
# Instrumentation for Energetic Neutral Atom Measurements at Mars, Venus, and the Earth

Klas Brinkfeldt

IRF Scientific Report 288
November 2005

ISSN 0284-1703
ISBN 91-7305-993-5

INSTITUTET FÖR RYMDFYSIK
Swedish Institute of Space Physics

Kiruna, Sweden

# Instrumentation for Energetic Neutral Atom Measurements at Mars, Venus, and the Earth

by

Klas Brinkfeldt
Swedish Institute of Space Physics
P. O. Box 812, SE-981 28 Kiruna, Sweden

IRF Scientific Report 288
November 2005

Printed in Sweden
Swedish Institute of Space Physics
Kiruna 2005
ISSN 0284-1703
ISBN 91-7305-993-5

**Abstract**

This thesis deals with the development and calibrations of sensors to measure energetic neutral atoms (ENAs) at Mars, Venus, and the Earth. ENAs are formed in charge exchange processes between energetic, singly–charged ions and a cold neutral gas. Since ENAs can travel in long straight trajectories, unaffected by electric or magnetic fields, they can be used to remotely image plasma interactions with neutral atmospheres. ENA instrument techniques have matured over the last decade and ENA images of the Earth's ring current for example, have successfully been analyzed to extract ion distributions and characterize plasma flows and currents in the inner magnetosphere.

Three different ENA sensors have been developed to image ENAs at Mars, Venus, and the Earth. Two of them, the nearly identical Neutral Particle Imagers (NPIs) are on-board the Mars Express and Venus Express spacecraft as a part of the Analyzer of Space Plasmas and Energetic Atoms (ASPERA-3 and 4) instruments. The third is the Neutral Atom Detector Unit, NUADU, aboard the TC-2 spacecraft of the Double Star mission. The NPI design is based on a surface reflection technique to measure low energy ($\sim$ 0.3-60 keV) ENAs, while the NUADU instrument is based on a simple design with large geometrical factor and solid state detectors to measure high energy ENAs ($\sim$ 20-300 keV).

The calibration approach of both NPI sensors were to define the detailed response, including properties such as the angular response function and efficiency of one reference sensor direction then find the relative response of the other sensor directions. Because of the simple geometry of the NUADU instrument, the calibration strategy involved simulations to find the cut-off energy, geometrical factor and angular response. The NUADU sensor head was then calibrated to find the response to particles of different mass and energy. The NPI sensor for the Mars Express mission revealed a so-called priority effect in the sensor that lowers the angular resolution at high detector bias. During the calibration of the Venus Express NPI sensor tests were made which showed that the priority effect is a result of low amplitude (noise) pulses generated in the detector system. The conclusion is that the effect is caused by capacitive couplings between different anode sectors of the sensor. The thresholds on the preamplifiers were set higher on the Venus Express NPI, which removed the priority effect.

Two of the three ENA experiments, the Double Star NUADU instrument and the Mars Express NPI sensor, have successfully measured ENAs that are briefly described in the thesis. The first ENA measurements at Mars were performed with Mars Express. Initial results from the NPI include measurements of ENAs formed in the Martian magnetosheath and solar wind ENAs penetrating to the nightside of Mars. The first results from NUADU in Earth orbit show the expected ENA emissions from a storm time ring current. Also, together with the HENA instrument on the IMAGE spacecraft, NUADU have produced the first multi-point ENA image of the ring current.

**Keywords:** Energetic neutral atoms, instruments and techniques, mass spectrometry, microchannel plates, solid state detectors, solar wind interaction, planets, magnetosphere, exosphere, ring current

## Sammanfattning

Den här avhandlingen behandlar utvecklingen och kalibreringen av sensorer för att mäta energirika neutrala atomer (ENA) vid Mars, Venus och Jorden. ENA bildas i laddningsutbytesreaktioner mellan energirika, envärt laddade joner och en kall neutral gas. Eftersom ENA kan färdas i långa raka banor, opåverkade av elektriska och magnetiska fält, kan dom användas för att avbilda plasmats interaktioner med neutrala atmosfärer. Instrumenttekniken för att mäta ENA har mognat under det senaste decenniet och ENA-bilder av till exempel Jordens ringström har kunnat analyserats för att utröna jondistributioner, flöden och strömmar i den inre magnetosfären.

Tre olika ENA sensorer har utvecklats for att ta ENA bilder vid Mars, Venus och Jorden. Två av dem, de nästan identiska Neutral Particle Imagers (NPI), ingår i instrumenten Analyzer of Space Plasmas and Enargetic Atoms (ASPERA-3 och 4) på rymdsonderna Mars Express och Venus Express. Den tredje är Neutral Atom Detector Unit (NUADU) ombord på satelliten TC-2, som ingår i Double Star missionen. NPI är baserad på en ytreflektionsteknik för att kunna mäta ENA med låga energier ($\sim$ 0.3-60 keV), medan NUADU baseras på en enkel design med hög geometrisk faktor och halvledardetektorer för att mäta ENA med höga energier ($\sim$ 20-300 keV)

Kalibreringen av de båda NPI sensorerna utfördes genom att mäta sensorsvaret, innefattande bland annat vinkelsvarsfunktion och effektivitet, från en referensriktning och sedan göra en relativ mätning mellan alla olika riktningar. Eftersom NUADU instrumentet har en enkel geometri, var kalibreringsstrategin att ta fram värden för avlänkningsplattornas energitröskel, geometrisk faktor och vinkelsvar. NUADU kalibrerades sedan för att finna sensorsvaren för partiklar med olika massa och energi. NPI på Mars Express uppvisade en så kallad prioritetseffekt, som sänker vinkelupplösningen vid hög detektorspänning. Under kalibreringen av NPIn för Venus Express utfördes tester som visade att prioritetseffekten är ett resultat av pulser med låg amplitud (brusnivå) som genererades i detektorsystemet. Slutsatsen är att effekten är ett resultat kapacitiva kopplingar mellan olika anodsektioner i sensorn. Tröskelvärdena på för-förstärkarna i Venus Express NPI sattes högre vilket gjorde att prioritetseffekten försvann.

Två av de tre ENA experimenten, NUADU instrumentet på Double Star och NPI på Mars Express har genomfört ENA mätningar, vilket är kortfattat beskrivet i avhandlingen. De första ENA mätningarna vid Mars genomfördes med Mars Express. Tidiga resultat från NPI inkluderar mätningar av ENA som bildats dels i magnetoskiktet vid Mars och i solvinden, som strömmar igenom till nattsidan av Mars. De första resultaten från NUADU visar de väntade ENA emissionerna från ringströmmen under en magnetosfärsstorm. Tillsammans med HENA instrumentet ombord på satelliten IMAGE har NUADU tagit de första multipunktbilden av ENA från ringströmmen.



**Nyckelord:** Energirika neutrala atomer, instrument and tekniker, massspektrometri, mikrokanalplattor, halvledardetektorer, solvindens påverkan, planeter, magnetosfär, exosfär, ringström

# Contents

*A man that looks on glass,*
*On it may stay his eye;*
*Or if he pleaseth, through it pass,*
*And then the heaven espy.*
*– George Herbert*

# Chapter 1

# Introduction

*Before beginning a Hunt, it is wise to ask someone what*
*you are looking for before you begin looking for it.*
– Winnie the Pooh in "Pooh's Little Instruction Book", inspired by A. A. Milne

Our solar system has in recent times been subject to massive investigation efforts. The number of robotic missions have dramatically increased over the last few decades. Where mankind cannot or dare not go yet she sends machines. Since the first Sputnik in 1957, all planets except Pluto have been the target of one or several robotic missions with close flybys, dedicated orbiters or even landers. Images and data describing worlds very different from our own have been sent back, frequently raising more questions than they answered, further sparking us to imagine new, improved missions. Such missions have provided invaluable information about our immediate neighborhood in the Universe. Early on, it became apparent that a supersonic flow of plasma, called the solar wind, flows from the Sun throughout the solar system. The planets and moons of the solar system are obstacles in the solar wind like rocks in a stream of water and depending on the planetary properties the interaction with the solar wind differs. Fig. 1.1 illustrates the solar wind flow around planets with different properties. The study of this flow and its interaction with the different obstacles are what we today call space plasma physics. Knowledge in this field has accumulated and we are now sorting out the details of the solar wind interaction with the Earth. Our closest neighbors in the inner solar system are not at that stage yet simply because there have been many more missions carrying relevant instrument payloads in Earth orbit. Ground-based studies have also contributed a great deal to understanding the Earth's interaction pattern.

While, the microscopic processes involved in space plasma physics are, in general, similar to laboratory plasma. What makes space plasma physics so unique is the investigations of large scale phenomena and the combination of different factors determining the observed processes. On a global scale, two main factors define the type of interaction between the solar wind and a celestial body, the presence of a large scale magnetic field and the presence of an atmosphere/ionosphere. The Moon, the terrestial planets Mercury, Venus, Earth and Mars, display all possible combinations of these two factors as summarized in Table 1.1. Traditionally, measurements of electrons and ions

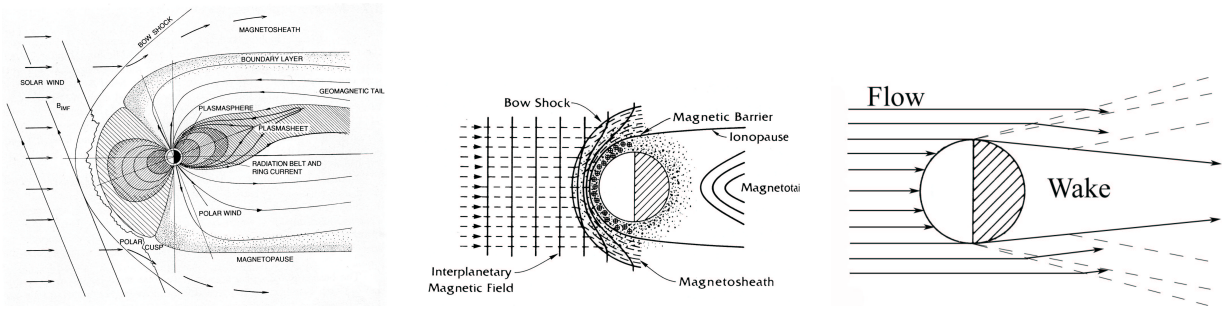


Figure 1.1: Illustration of the solar wind flow around (left) a planet with a global magnetic field (for example the Earth), (middle) a planet without a global magnetic field, but with an atmosphere (Mars and Venus), and (right) an obstacle without magnetic field and atmosphere (the Moon). Adapted from *Parks* [1991] and *Kivelson and Russell* [1995].

Table 1.1: Conditions at the terrestial planets and the Moon.

| Object | Global magnetic field | Atmosphere | Type of obstacle |
|---|---|---|---|
| Mercury | yes | no | Magnetosphere/surface |
| Venus/Mars | no | yes | Ionosphere |
| Earth | yes | yes | Magnetosphere |
| Moon | no | no | Surface |

have been the means to map and characterize various particle populations in situ. These local measurements have the inherent drawback that temporal and spacial variations cannot be resolved unambiguously. Moreover, in building up the global picture of particle distribution one is forced to rely on statistical observations only. Normally, imaging is referred to the detection of the direction (and wavelength) of photons originating from some source region. In the last decade global imaging techniques have grown to become an important complement to the local measurements. One such global imaging technique is called energetic neutral atom (or ENA) imaging. This thesis deals with the measurements of ENAs at Mars, Venus and the Earth. The focus is on ENA instrument development and specifically the calibration of three ENA sensors for different missions to the Earth and its neighbors. Also, some initial results from the ENA sensors at Mars and the Earth are presented. This, first chapter gives an introduction to the concept of ENAs, the different techniques to measure them, and some examples of existing ENA instruments. The following Mars, Venus, and Earth chapters begin with a general introduction to ENA measurements (or lack there of) at the planet in question, followed by a description of the specific mission and the ENA sensor. In the case of Mars and Venus, the sensors that have been developed are the Neutral Particle Imagers (NPI) of the Analyzer of Space Plasmas and Energetic Atoms ASPERA-3 and ASPERA-4 instruments on the Mars Express and Venus Express spacecraft respectively, and for the Earth it is the Neutral

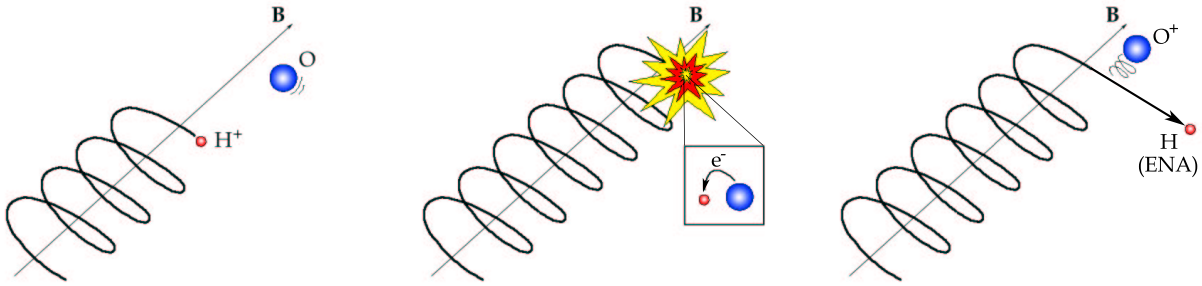


Figure 1.2: Energetic neutral atoms (ENA) can be formed in charge exchange interactions where an energetic positive ion obtains an electron from a neutral. The ion then becomes neutral and travels in a ballistic trajectory, unaffected by electric and magnetic fields.

Atom Detector Unit (NUADU) on-board the Double Star TC-2 satellite. Calibrations of the sensors are treated next. In the Mars and Earth chapters some initial results are also presented, while some expected results are shown in the Venus chapter. Chapter 5 is a summary including future plans.

## 1.1 Energetic neutral atoms (ENA)

Energetic neutral atoms (ENAs) are formed in various places throughout the solar system. They are produced in a process called charge exchange between singly-charged energetic ions and neutral atoms (or molecules). Charge exchange is when an electron is transferred from a neutral to an energetic, positively, singly charged ion without any significant transfer of momentum, which is true for particle energies above $\sim$ 10 eV (for oxygen). That is, the ion, which is transformed to an ENA does not notably change its velocity. Because they are neutral, ENAs propagate from the interaction region in ballistic orbits unaffected by electric or magnetic fields. The charge exchange process is illustrated in Fig. 1.2. In space, ENA measurements can thus be used to remotely image the interaction between ions (or molecular ions) and neutral gas in planetary environments. In much the same way as photography images reflected photons from an distant object, an ENA instrument can 'take pictures' of emitted ENAs from a distant source (provided their energies significantly exceeds the escape energy to avoid gravitational bending of the trajectories). A typical example of such a source is where the flowing plasma interacts with a planet's exosphere. Also, wherever there exists a cold, neutral background gas and a plasma, that region will emit ENAs. Such measurements are called ENA imaging and can give global information on ion distributions to complement the local, *in situ* measurements with ion spectrometers. The most common charge exchange reactions that produce ENAs in the solar system are:

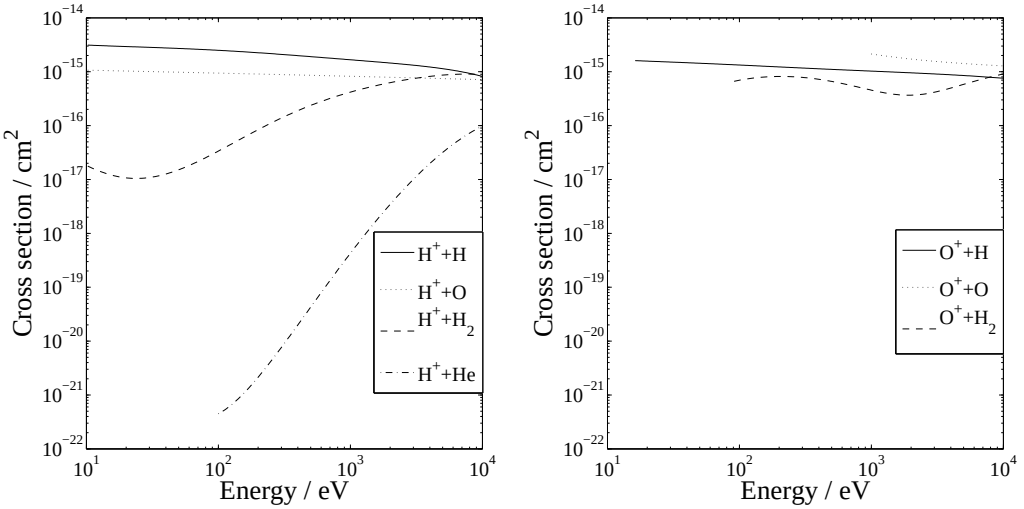


Figure 1.3: Cross sections of the most common charge exchange processes in the solar system.

$$
\begin{array}{lcllcl}
\mathrm{H}^+ & + & \mathrm{H} & \longrightarrow & \mathrm{H}_{ENA} & + & \mathrm{H}^+ \\
\mathrm{H}^+ & + & \mathrm{O} & \longrightarrow & \mathrm{H}_{ENA} & + & \mathrm{O}^+ \\
\mathrm{H}^+ & + & \mathrm{H}_2 & \longrightarrow & \mathrm{H}_{ENA} & + & \mathrm{H}_2^+ \\
\mathrm{O}^+ & + & \mathrm{H} & \longrightarrow & \mathrm{O}_{ENA} & + & \mathrm{H}^+ \\
\mathrm{O}^+ & + & \mathrm{O} & \longrightarrow & \mathrm{O}_{ENA} & + & \mathrm{O}^+ \\
\mathrm{O}^+ & + & \mathrm{H}_2 & \longrightarrow & \mathrm{O}_{ENA} & + & \mathrm{H}_2^+
\end{array}
$$

There are also helium charge exchange reactions, but they can often be neglected, especially for low energy ($< 1$ keV) ENA imaging since the cross section for such reactions is then several orders of magnitude lower (see Fig. 1.3).

Since ENAs can usually travel long distances in straight lines in space, the measured flux from one direction is an integration of all the ENAs along the line of sight from that direction (as illustrated in Fig. 1.4). From this we can estimate the ENA flux $j(E)$ of energy $E$ at the instrument position from this direction:

$$j(E) = \int_0^\infty \sum_i n_i(l)\sigma_i(E) j_{ion}(E,l) e^{-\sum_j \varsigma_j(E)\varphi_j(l)} dl, \tag{1.1}$$

where $\sigma_i$ is the charge exchange cross section, $i$ numbers different neutral species, $\varsigma_j$ is the ENA stripping cross section on neutral species $j$ and $j_{ion}(E,l)$ is the ion flux of energy $E$ at position $l$ along the line of sight. The column density of neutrals $\varphi$ to a point $l$ along a line of sight ($l = 0$ is the location of the ENA instrument) is:

$$\varphi_i(l) = \int_0^l dl' n_c(l'), \tag{1.2}$$

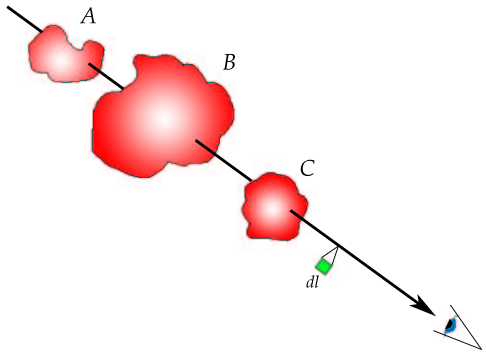


Figure 1.4: Line of sight geometry of ENA observations. ENAs produced in line elements $dl$ of the line of sight $l$ from infinity to the observer are added. For the line of sight depicted here the number of ENAs arriving at the observer is equal to the sum of the portion of ENAs produced in the ENA production areas A, B, and C that are in the line of sight.

where $n_c(l')$ is the number density at position $l'$ along the line of sight. The exponential term in equation 1.1 describes a loss of ENAs due to electron loss in a collision with a stationary atom or ion (stripping). In some circumstances the stripping cross sections are much smaller than the charge exchange cross sections and can therefore be neglected. The interaction is then referred to as ENA-thin. In such circumstances, the stripping term in equation 1.1 can be omitted and the simplified expression

$$j(E) = \int_0^\infty \sum_i n_i(l)\sigma_i(E)j_{ion}(E,l)dl, \tag{1.3}$$

can be used instead. When we consider only ENAs of the specific energy $E$ we have the differential intensity with units of number of particles per energy per $cm^2$ per steradian (sr) per second (or $eV^{-1}$ $cm^{-2}$ $sr^{-1}$ $s^{-1}$). Sometimes it is necessary to use the integrated number intensity instead, which is simply the differential intensity integrated over all energies

$$J = \int_{E_{min}}^\infty J(E)dE, \tag{1.4}$$

where $E_{min}$ is greater than the escape energy.

The ENA intensity at a point in space from a specific direction thus depends on the neutral particle density, the ion flux and the probability of charge exchange occurring between the two populations as in equation 1.1 above. Simulation models can produce calculated ENA intensity using parameterized models of ion and neutral gas distributions. The task is then to compare with the measured intensities in order to adjust parameters to fit in the model. In this way, physical information can be extracted from the images. To transform the measured ENA (the measurable

quantity) into the modeled differential ENA intensity (a physical quantity) the properties of the particular ENA instrument have to be known. A purely geometrical property of the instrument, the geometrical factor (or G-factor), is a measure of how large a portion of space the instrument is able to see through one of its apertures of a certain area. A thorough explanation of the theory describing the gathering power of particle telescopes can be found in *Sullivan* [1971]. Fig. 1.5 is a sketch of a two-element telescope consisting of an aperture and a detector. The angular confinements set by the aperture and the detector size are used to define the geometrical factor:

$$G = \int_{\Omega} \int_{S_2} \mathbf{ds} \cdot \mathbf{r} \; d\omega, \tag{1.5}$$

where, as in Fig. 1.5, $S_2$ is the area of the detector, $\mathbf{ds} = \hat{n} \cdot ds$ is an element of that area, $\mathbf{r}$ is the incoming particle vector and $d\omega$ is the element of solid angle of the total solid angle $\Omega$ that is confined by the aperture and detector.

Another property important to the instrument's ability to measure the ENA flux is its efficiency. For the simple example geometry in Fig. 1.5 one can expect all incoming particles incident on the aperture within the defined fraction of solid angle to impact the detector. If the detector is assumed to be able to detect all incoming particles, such a geometry has an efficiency of $\varepsilon = 1$. This may not be the case for other geometries and certainly not for all detectors. For almost any detector the efficiency is dependent on the energy of the incoming particles and can be considerably lower than unity. A common detector type used in ENA sensors is microchannel plate (MCP) detectors in which only $\sim 60\%$ of the total detector area is active (see Section 1.2, which describes different ENA sensor designs and detectors.). Calibrations of the instrument are thus required to find the ratio

$$\varepsilon(E) = \frac{C}{I}, \tag{1.6}$$

where $C$ is the measured ENA count per unit time (or count rate) and $I$ is the total number of ENAs of energy $E$ entering the detector per unit time.

Another important characteristic of a sensor is $D$, the noise of the detector or dark count when no incoming particles are present. All types of detectors have a noise associated with their operation. The MCP detector mentioned above, for example, is constructed of millions of tiny capillaries that function as electron multipliers. They have a small background dark current, typically 0.1 counts $s^{-1}$ per $cm^2$ of detector area associated with sporadic release of secondary electrons inside the channels caused by, for example, impurities in the MCP material or residual gas trapped inside the channels. Solid state detectors are another type of detector where the primary source of noise is thermal motion of electrons. The actual ENA flux associated with the count rate $C_E$ is then:

$$J(E) = \frac{C_E - D}{G \cdot \varepsilon_E}, \tag{1.7}$$

where $C_E$ is the count rate and $\varepsilon_E$ the efficiency of particles with energy $E$, $G$ is the geometrical factor and $D$ is the instrument dark count.

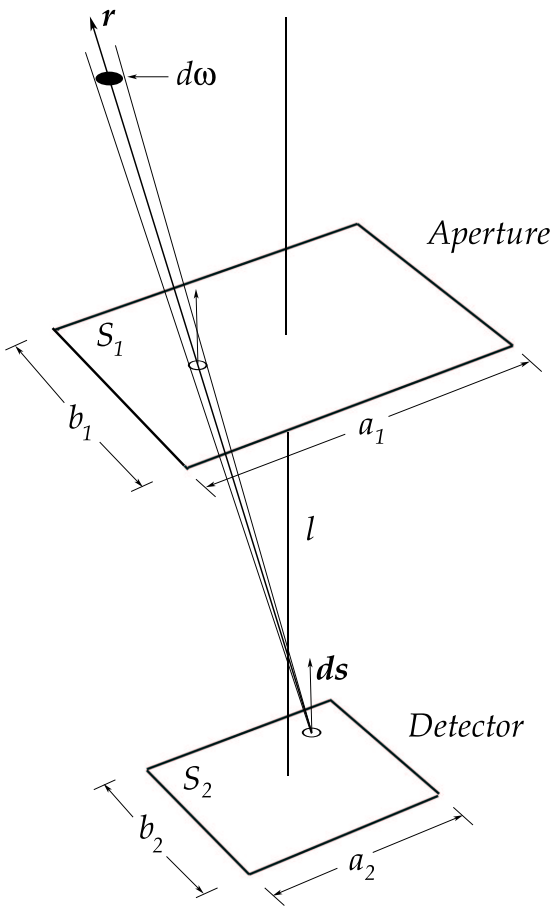


Figure 1.5: Sketch of a simple two element particle sensor consisting of an aperture and a detector plane. The particle trajectory has to transcend the aperture within a defined solid angle to hit the detector. This angle depends on the area of aperture and detector and the distance between them.

## 1.2 ENA instruments

*Dessler et al.* [1961] proposed a study of the ENAs emitted in the Earth's ring current (a doughnut-shaped current carried by charged particles that are trapped in the Earth's magnetosphere at $\sim 2-6$

$R_E$) and bombarding the upper atmosphere during magnetospheric storms. Much later, in 1987, the first unambiguous global ENA image of the Earth's ring current was produced [*Roelof*, 1987]. The image was not measured from the Earth as *Dessler et al.* [1961] had suggested but from space above the ring current. The instrument used was not a dedicated ENA instrument, but rather the Medium Energy Particles Instrument (MEPI) on the ISEE-1 spacecraft [*Roelof et al.*, 1985].

At Earth several space-borne instruments [*Barabash et al.*, 1998; *Mitchell et al.*, 2000; *Pollock et al.*, 2000; *Moore et al.*, 2000; *McKenna-Lawlor et al.*, 2004] have recently used ENA imaging to image the ring current ion distribution in the Earth's magnetosphere (see Section 4.1). The INCA (Ion and Neutral Camera) on the Cassini spacecraft has recently made measurements of ENAs from the interaction between Saturn and its moon Titan [*Mitchell et al.*, 2005]. ENAs at Mars have not been investigated prior to the ASPERA-3 instrument, though the failed Mars 96 spacecraft carried with it an earlier version of the instrument that would have measured ENAs using two sensors [*Barabash et al.*, 1995]. The ASPERA-4 instrument will be the first ENA instrument at Venus when it arrives at the planet in 2006.

Designing an ENA instrument is a trade-off between several competing properties. The low ENA intensities from some interesting areas in space (compared to charged particle flux, for example, the measured ENA component in the solar wind is $10^{-3} - 10^{-4}$ of the charged particle flux [*Collier et al.*, 2001]) would warrant having large apertures on the sensor to increase the number of measured ENAs, but at the same time a desire for better angular resolution would suggest smaller apertures. If, for example, an instrument should be able to resolve the major structures of the Earth's ring current from 7.2 $R_E$ above the Earth's north pole (the apogee altitude of the IMAGE spacecraft *Burch* [2000]) an angular resolution of $\sim 8°$ is required [*Mitchell et al.*, 2000], corresponding to $\sim 1$ $R_E$ at the equatorial plane from that altitude.

The first dedicated ENA instrument in space was a sounding rocket payload launched on April 25, 1968 (Fig. 1.6) [*Bernstein et al.*, 1969]. The instrument first employed a filter system based on electrostatic and magnetic fields to deflect charged particles, then a thin foil to convert the neutrals to ions followed by an curved electrostatic analyzer to determine the energy of the particles and finally a detector. Modern ENA instruments are based on similar building blocks and they will now be presented in more detail.

### 1.2.1 Deflection systems

The first of these building blocks is the deflection system. Since the detectors used in ENA instruments are also sensitive to charged particles, all ENA instruments must employ some sort of deflection system to remove the charged component of the incoming flux. The simplest and most common way to do this is to apply an electric field in the particle path in the instrument. The properties of such electrostatic deflection paths are important design parameters because not only do they determine the effective energy range in which charged particles can be removed, but very often the deflector works also as a collimator, setting parameters for angular resolution and the geometrical factor of the instrument. The simplest deflector systems, made up of two parallel plates of length $l$ separated with the distance $d$ and voltage $V$, has an upper energy cut-off, $E_{cut}$, for which

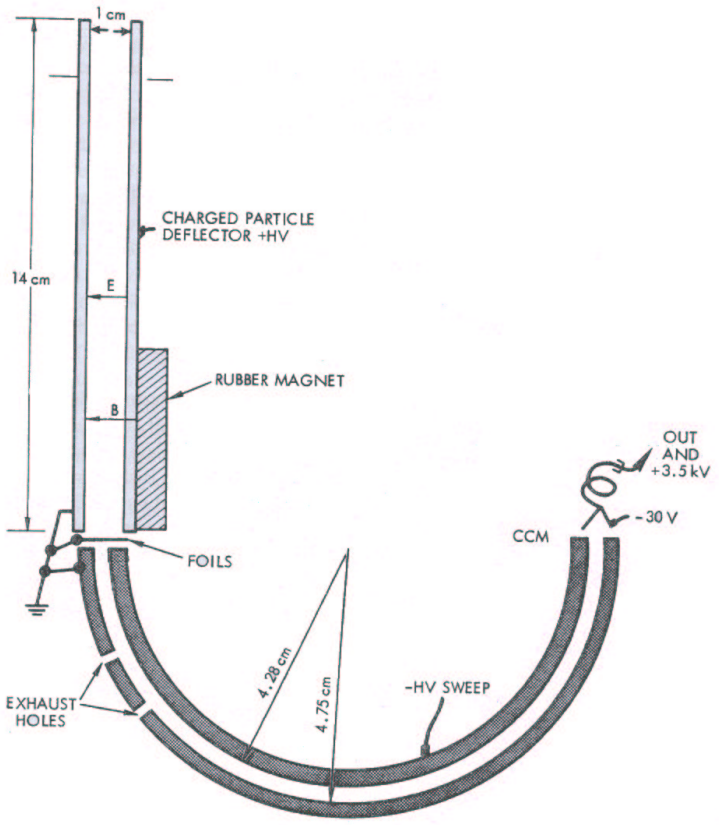


Figure 1.6: Diagram of the first ENA instrument ever used in space. Charged particles were removed using electrostatic and magnetic fields generated in the charged particle deflector and from the rubber magnet. The neutrals continue through unaffected and impact the foils. There they are converted to positive ions and can pass through the curved electrostatic analyzer if they have the correct energy. The energy is determined by the voltage across the particle path in the analyzer. The voltage on the inner analyser plate was swept to measure different energies (-HV sweep). Particles with the correct energy could pass through the analyzer and were detected using a continous channel electron multiplier (CCM). From *Bernstein et al.* [1969].

it no longer rejects charged particles of charge $q$, through the system [*Barabash*, 1995]

$$E_{cut} = qV\left(1 + \left(\frac{l}{4d}\right)^2\right) \tag{1.8}$$

To have a high energy cut-off it is good to have a long, narrow deflection path (large $l$, small $d$) and high voltage. Too high $V$ across a small $d$ may cause discharges between the two deflection plates. A rule of thumb is to have no higher voltage than 1 kV per mm of space in vacuum, corresponding

to a field strength of $10^6$ V/m. Increasing $l$ and decreasing $d$ will have a negative effect on the geometrical factor, but obviously improve angular resolution. The $l$ and $d$ parameters correspond to the $l$ and $b_1$ dimensions from Fig. 1.5. Increasing $l$ will decrease the domain of $\Omega$. While shortening $b_1$ may be compensated for by increasing $a_1$, it will cause a loss of angular resolution of the sensor. There is then a trade off between the efficiency of the deflection system (i.e. the energy range of the instrument) and other parameters such as the geometrical factor (which ultimately reflects on the sensitivity of the instrument) and the angular resolution of the measurements.

### 1.2.2 ENA ionization

Depending on the energy range of the instrument and whether it has energy or mass resolution, the next step may be to strip the incoming ENA of an electron, converting it to an ion. The energy of the newly formed ion can then be determined by conventional techniques used in ion instruments. In some designs the ion is accelerated to an energy measurable with the detector. This method may be necessary for low energy ENA instrumentation and certain types of detectors. One way to ionize an incoming ENA is to let it pass through an ultra-thin foil. Such foils are made up of a thin sputtered or condensed layer of material, usually 20 - 200 Å thick or 0.5 - 10 $\mu$g/cm$^2$ (corresponding to only a few atomic layers in most cases), attached to a high transmittance (90-95 %) grid for mechanical stability. The material used in the thin foils is often silicon or carbon because they provide lowest density per cm$^2$ and thus attenuates an incoming particle's energy the least. Particles exiting the foil may have one of the possible charge states, namely, positive, negative, or neutral. In the process of particle-matter interaction, energy straggling and angular scattering occur. The scattering angle is proportional to the particle mass and inversely proportional to the particle energy. A plot of the average energy loss against foil thickness for hydrogen and helium is shown in Fig. 1.7.

Foils cannot be used for very low energy ENA measurements ($E < 100...300$ eV) simply because the particles do not have enough energy to penetrate them. Instead a method of surface ionization can be used. Surface ionization is based on letting low energy particles reflect off a specially prepared surface, coated with a material with low work function (for example, caesium or tungsten), at a shallow angle ($< 15°$, i.e. thus only graze the surface). In the process the ENAs can be ionized into either positive or negative ions depending on the surface, ENA species, and energy. The ionization efficiency varies depending on species, target material, angle of incidence, and particle energy.

### 1.2.3 Time of flight (TOF)

During the penetration of a foil or the grazing of a conversion surface, electrons are emitted from the interaction. The electrons can be used to provide a START signal to time of flight (TOF) systems. The time of flight technique is based on measuring the time it takes for a particle to travel a well-defined distance between START and STOP events to measure the particle velocity. Combining the knowledge of the incoming particle's energy (from electrostatic analyzers or solid state detectors that are able to resolve energy) TOF techniques may be used to determine the mass of a particle. A simple TOF system (sometimes referred to as a TOF cell) is shown in Fig. 1.8. The START signal is received when the detector $D_1$ registers electrons emitted in the interaction

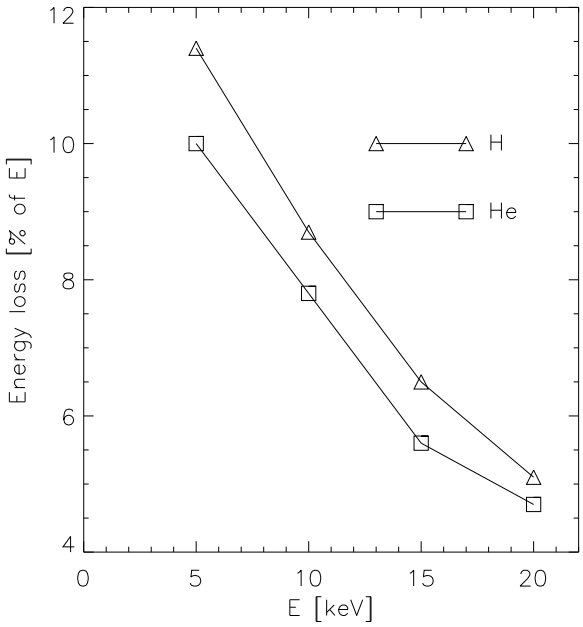


Figure 1.7: The energy loss of H and He ENAs with energy E through a foil of thickness 1.1 $\mu$g/cm$^2$. Adapted from *Gruntman* [1997].

with the ultra-thin foil. The time is then measured between the START signal and the STOP signal, which comes from the impact of the particle on detector $D_2$. The main advantage of TOF systems is their low noise. Because they are coincidence systems, they require two valid events (START/STOP) to occur within a certain time window for a count to be produced. To increase the accuracy of the measured TOF, an electrostatic mirror can be installed, which first accelerates the emitted electrons from the foil toward detector $D_2$ then reflects them and accelerates them toward $D_1$ (a typical example is the RAPID instrument [*Wilken et al.*, 1997] designed for the CLUSTER mission) The START timing then becomes independent of where the ENAs hit the foil.

### Shutter-based TOF

The problem with using foil or surface interactions in ENA instruments is that they end up with a poor energy resolution (50 % or worse for low energy, $<$ 10 keV instruments). This is because the original particle looses part of its energy in the interaction (Fig. 1.7). For the same reason, it is also impossible to measure ENAs with energies E $<$ 10 eV. The next generation ENA instruments may not require the conversion of ENAs into ions for energy analysis. They will instead rely on velocity filters based on two or more super fast shutters that are only open for a very short time to allow ENAs of a particular velocity to pass through. Fig. 1.9 show two examples of the velocity

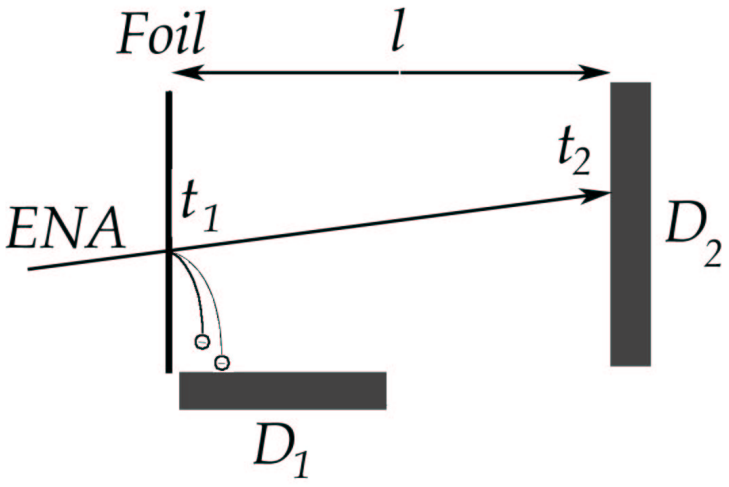


Figure 1.8: Principal of a time of flight (TOF) system. An ENA penetrates the foil and knocks off electrons. They are collected on detector $D_1$ while the original particle continues to detector $D_2$. The time is then measured between $t_1$ when the electrons reach $D_1$ and $t_2$ when the particle hits detector $D_2$. The velocity of the ENA is then estimated from $v = l/(t_2 - t_1)$.

filter principal. The first sketch presents a velocity filter which transmits particles with the fixed velocity $L/t$. If the detector has energy resolution, both mass and energy of an incoming ENA may be derived. In the second sketch, the signal from the detector provides information of the mass composition of the incoming beam of particles, assuming the beam energy is known. Such a system could replace a TOF system. Particle sensors usually require a mass (energy) resolution $\Delta m/m < 10$ % to differentiate between populations in space. For the system to the left in Fig. 1.9, the resolution $\Delta m/m$ depends on the shutter-open time $\Delta t$. 10 eV, hydrogen atoms travel at $v \approx 44$ km/s. If $L = 8$ cm the TOF, $t$, is 1827 ns. If an ideal shutter is assumed (square wave from CLOSED to OPEN to CLOSED) the required shutter-open time $\Delta t = (t/2)(\Delta m/m) = 58$ ns. Fig. 1.10 shows the TOF times and $\Delta t$ for different species and energies with a mass resolution of 5 % for TOF distances of $L = 8$ and $L = 4$ cm between the two shutters. The problem with such systems is that they have to remain closed under long periods then open for very short times (slow duty cycle, $\Delta t \ll t$). To remedy this problem and increase the system's open time one can use a coded sequence when individual shutters are opened and closed. Processing based on the known sequence can then allow "decoding" of the measured counts into an interpretable result. Theoretical estimations show that such time-coded measurements could have a duty cycle of up to 50 % [*Brock et al.*, 2000].

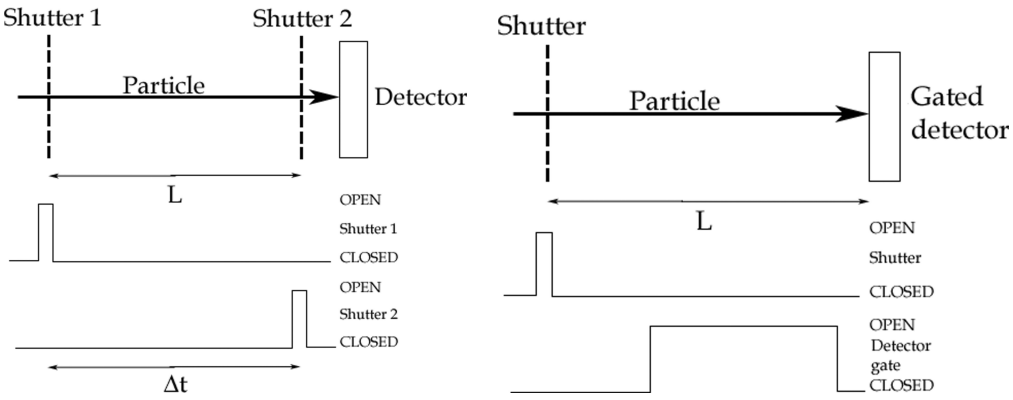


Figure 1.9: Two examples of using micro-shutters in the ENA measurement path. The sensor to the left operates as a pure velocity filter. Shutter 1 is open for a very short time, admitting particles to propagate across $L$ to Shutter 2. If the particle has the correct velocity, Shutter 2 is open when it reaches the shutter. If not, the particle will not reach the detector. The example to the right is basically a TOF cell where the START signal comes from the shutter-open time. It uses a detector allowing multiple STOP signals. The shutter opens to let through particles of different velocities and the output is a velocity spectrum of the particles.

### 1.2.4 Detectors

The same detectors used for charged particles are also used to detect ENAs. A common detector type used for space applications is the channel electron multiplier (CEM). It is typically made up of a curved glass tube coated on the inside with a material that easily emits secondary electrons when impacted. The glass tube itself is slightly conducting and an electric field can be formed by applying a potential between the two ends of the tube so that any electrons are accelerated toward one end of the tube. Electrons impact the inner tube wall and knock out more electrons. These in turn impact again further down the tube releasing even more electrons and so on. This evolves into an electron avalanche and one initial particle impact at the starting end of the CEM results in typically $10^6 - 10^8$ electrons exiting at the other end. The electron cloud impacts a conducting anode resulting in a measurable current pulse. The CEM itself is curved to avoid ions, formed from trapped gasses in the channel or impurities on the channel wall, to be accelerated in the opposite direction and cause multiple electron avalanches (a process called ion feedback).

The size of the resulting electron cloud or gain in a CEM is mostly determined by the diameter-to-radial-length ratio of the glass tube. Scaling of the tube down to very small sizes is thus possible with most of the gain retained. This has enabled the CEM to evolve into the micro channel plate (MCP). An MCP can be described as an array of miniature CEMs arranged to form a thin (typically $\sim 1$ mm) glass plate (Fig. 1.11, to the left). The microchannels perforating the plate each function individually as a CEM. Typical microchannel diameter is 6-12 $\mu$m and the plate size can vary in shape and size. For direction-sensitive instruments, round MCP plates with diameters between 30-

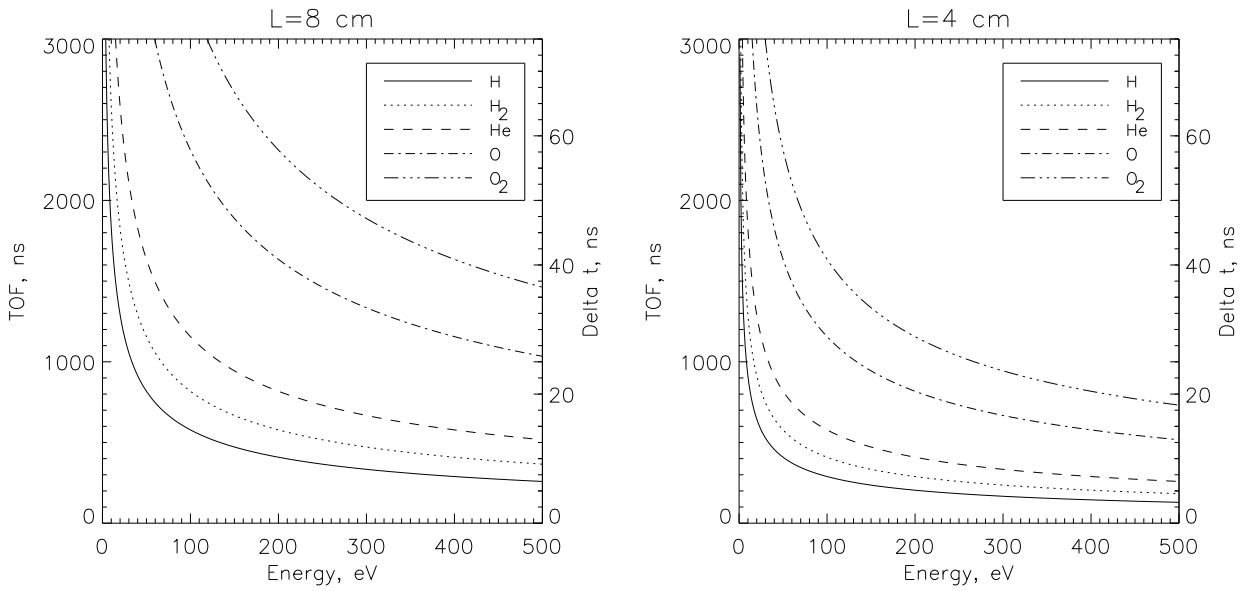


Figure 1.10: TOF times in ns for different species at low energies with drift distances between the two shutters of $L = 8$ cm (left), and $L = 4$ cm (right). On the right y-axes are the shutter-open times ($\Delta t$) in ns if a mass resolution of $\Delta m/m = 5$ % is assumed.

100 mm are often used. MCP plates are often operated stacked together in what is called chevron (two plates) or Z (three plates) stack to avoid ion feedback. To increase gain there should be a small gap between the plates. The cloud of electrons exiting the first plate then spreads radially to cover more microchannels on the second plate. The result is more electrons impacting an underlying anode in a slightly increased area. The typical footprint diameter of MCP plates in a chevron configuration is $\approx 1$ mm. Typical gain when using a gap of 0.1 mm between the plates is $10^6 - 10^7$, depending on the microchannel diameter.

Another type of detector used in particle space instrumentation is the solid state detector (SSD). When a particle impacts a semiconducting material, electrons are freed and can be extracted by biasing the material (Fig. 1.11, to the right.). The resulting current pulse is proportional to the energy deposited by the impacting particle. If the particle stops completely in the material, that is, all its energy is deposited, the size of the current pulse can be used to find the particle energy. When SSDs are coupled with TOF techniques to provide velocity information (for example as detector $D_2$ in Fig. 1.8) such systems can be used to find both energy and mass of a particle. The main advantage of using SSDs is that one can combine particle detection and energy measurement. The noise in SSDs comes from electrons that are released by thermal excitation. To reduce thermally generated noise, an SSD is usually formed by joining an n-type with a p-type semiconductor material. This sets up a depletion region which is slightly biased, forming a barrier for the thermal electrons. This rectifying junction drastically reduces the noise. When a particle impacts the detector electron-hole

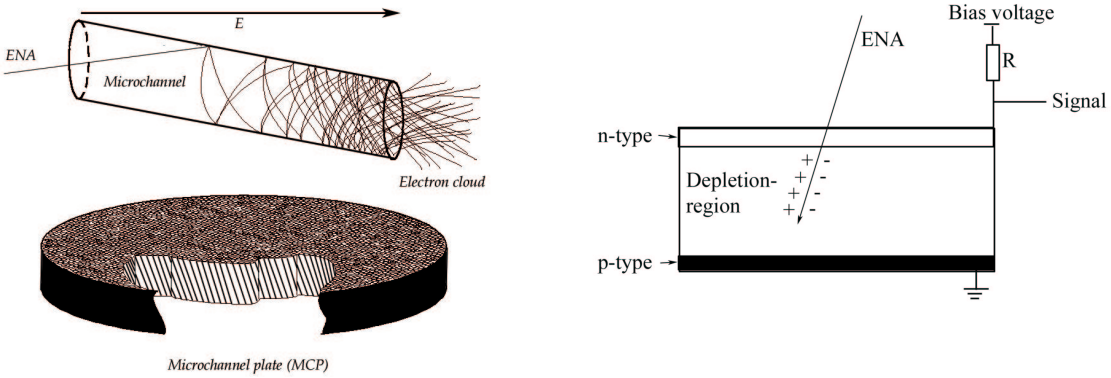


Figure 1.11: Microchannel plates (left) are made up of millions of small microchannels each tilted at an angle and each functioning as an individual CEM. (Right) Solid state detectors (SSDs) are made of a semiconducting material, in which electron-hole pairs are generated whenever particles impact the material.

pairs are generated along the particle's track in the material. Holes and electrons are separated and accelerated to each side of the depletion region. The downside of using SSDs is that there is always an inactive layer formed to seal the active region in when forming this junction. This layer is called the dead layer of the detector and has to be penetrated first in order for a hit to be registered. This means that incoming particles must have enough energy to get to the active region. Energy loss depends on the species and energy of the incoming particle and the material of the detector. For protons in silicon, $dE/dx$ increase from about 10 to 120 keV/$\mu$m for proton energies between 1-80 keV, then decrease again for higher energies [*Andersen and Ziegler*]. For $O^+$ ions in silicon, the expression $dE/dx = 27.177E_{O+}^{0.5159}$ (keV and $\mu$m units) in the energy range between 1 keV - 1 MeV has been derived as a best fit to empirical results [*Johansen*, 1990]. The expression corresponds to $dE/dx = 110$ keV/$\mu$m at $E_{O+} = 20$ keV, $dE/dx = 290$ keV/$\mu$m at $E_{O+} = 100$ keV, and $dE/dx = 670$ keV/$\mu$m at $E_{O+} = 500$ keV. Energy losses in the dead layers for oxygen are thus much higher than those for hydrogen. Silicon is the material usually used in SSDs. In silicon an energy deposition of 3.61 eV is required to generate one electron-hole pair. Another material used in SSDs is germanium. Dead layers in silicon detectors can be made as thin as a few nm.

### 1.2.5 UV rejection

For use in space, a thicker layer is often required on the active area of an SSD to reduce unwanted signal from ultra violet (UV) photons. This raises the lowest detectable particle energy further. A deposited aluminum layer of 150-200 nm effectively stops UV photons from entering the sensitive volume of the SSD.

MCP detectors are also sensitive to photons in the UV range. Measured MCP plate efficiencies for extreme UV wavelengths in the range between 30-60 nm reach $\sim$ 10 %, while at the hydrogen

Lyman-$\alpha$ wavelength of 126.1 nm, which dominates the UV output from the Sun, efficiencies are typically 1-2 % [*Fraser*, 1982]. Measurements at higher wavelengths with single channel multipliers display a logarithmic decrease in detection efficiency from 2 % at 120 nm to $10^{-9}$ at 260 nm [*Paresce*, 1975].

Techniques for separating UV photons and ENAs (UV rejection) in ENA sensors depend on the energy range of the sensor. *Funsten et al.* [1998] summarize UV rejection techniques including UV blocking foils for high energy ENAs ($>$ 20 keV), ultra thin foils for medium energy ENAs (1-50 keV), and transmission gratings for low energy ENAs (10-1000 eV). Deflection system plates are often either serrated or blackened using for example copper-sulfide to create roughened surfaces which reduce internal reflections of both charged particles and UV photons. The use of foils to convert ENAs to charged particles for high and medium energies ($>$ 1 keV) also provides protection for UV photons. In the case of high energies ($>$ 20 keV), thick ($10 - 15$ $\mu$g/cm$^2$) UV blocking foils are used. These attenuate a large fraction of the UV photons, while allowing high energy ENAs to pass [*Mitchell et al.*, 1998, 2000]. In the case of ultra-thin foils, a larger portion of the UV radiation can penetrate, but UV and ENAs converted to charged particles can be separated after the foil using electric and/or magnetic fields. As discussed above, a particle loses part of its energy when passing through a foil. It also changes its direction, which translates to a worse angular resolution, especially at lower energies. An alternative method to remove UV from the measurements is the use of transmission gratings. They make use of the diffraction characteristic of light. Transmission gratings are made up of thin (100-200 nm) parallel bars with a separation of $<$ 100 nm. The slits between the bars act as a diffraction filter that efficiently (by a factor of $10^4 - 10^5$) suppresses UV, while allowing ENAs to pass. Because of the slit structure UV suppression depends on polarization. UV suppression is lower in the dimension along the slit. The grating itself and its support structure block part of the ENA flux. Measurements on an existing gold transmission grating yielded a transmittance of 44 % [*Funsten et al.*, 1998]. The systems with shutters in Fig. 1.9 will be immune to UV contamination and have a transmittance of ENAs of $<$ 50 %.

### 1.2.6 Examples of ENA instruments

The High Energy Neutral Atom (HENA) imager [*Mitchell et al.*, 2000] on the IMAGE spacecraft [*Burch*, 2000] measures ENAs in the $\sim$ 20-500 keV range. A schematic illustration of the instrument is shown in Fig. 1.12. ENAs enter a charge particle deflection system and penetrate a three-layer Si-polyimide-C START foil (6.5 $\mu$g/cm$^2$ Si, 7.0 $\mu$g/cm$^2$ polyimide, and 1.0 $\mu$g/cm$^2$ C) with a transmittance of $1.5 \times 10^{-3}$ for Lyman-$\alpha$ photons. The START signal is measured with the 1-D imaging START MCP. The ENAs then continue to either a pixelated SSD or a second foil, under which there is a 2D imaging MCP detector. Electrons emitted from the front of the SSD and the second foil at the ENA impacts are collected on the coincidence/SSD-STOP MCP providing a triple coincidence scheme. Mass and energy determination then comes from conventional TOF and SSD pulse height analysis. Alternative mass measurements are is possible from the MCP system since the number of electrons emitted from the foils depends on the mass of the particle penetrating it. Determining between hydrogen and oxygen is possible by comparing the pulse heights from the MCP system.

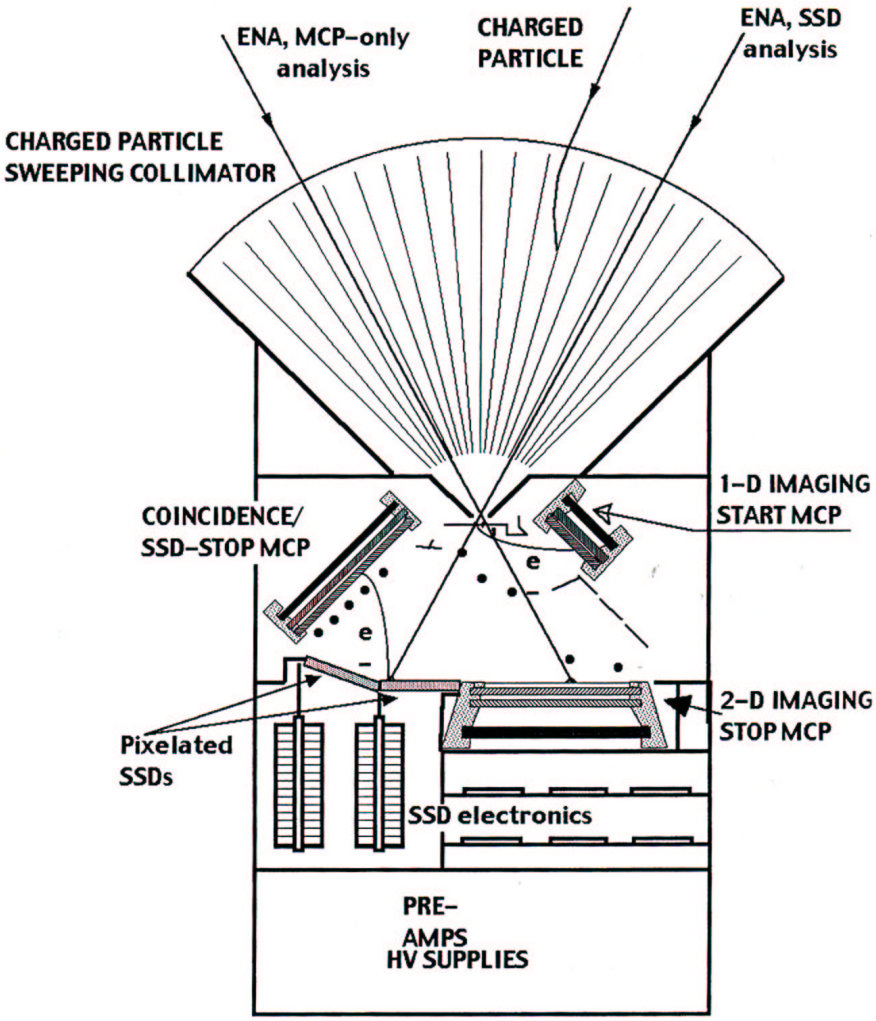


Figure 1.12: Principal of the HENA instrument on the IMAGE spacecraft. From *Mitchell et al.* [2000].

The first dedicated ENA instrument in orbit was the Prelude in Planetary Particle Imaging (PIPPI) instrument [*Barabash et al.*, 1998] on the Astrid-1 spacecraft [*Norberg et al.*, 1995]. The cylindrical sensor consisted of two parts (illustrated in Fig. 1.13), the PIPPI-SSD that measured high energy (13-140 keV) ENAs and the PIPPI-MCP that measured low-medium energy ($\sim 0.1-70$ keV) ENAs. The PIPPI-SSD sensor head was made up of a two-layer deflection system (cut-off energy 140 keV) and 16 SSDs (8/layer) mounted in the center of the instrument. Each SSD covered a sector of $5^\circ \times 30^\circ$ field of view. Two of the sectors in the sun direction differed from the other

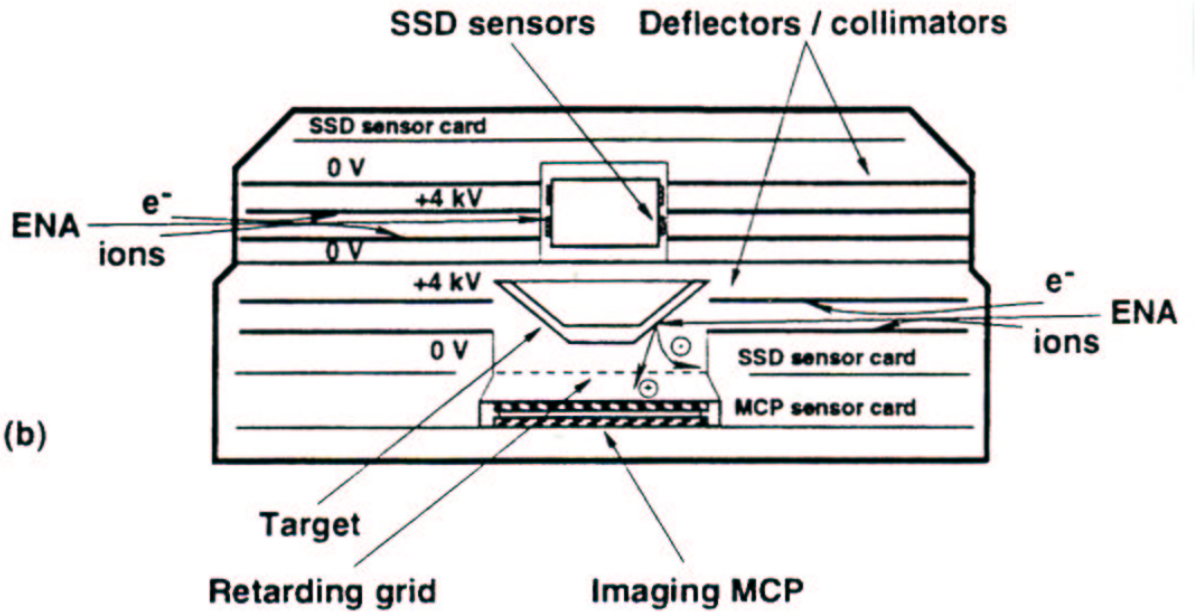


Figure 1.13: Schematic of the Prelude in Planetary Particle Imaging (PIPPI) sensor. From *Barabash* [1995].

14 in that one of them was completely blocked to monitor the electronic noise in one SSD, and the other was shielded by an aluminum foil so that only particles with energy higher than 140 keV could reach the SSD to monitor the energetic particles that could reach the detectors through the deflection system. The PIPPI-MCP sensor consisted of a one-layer deflection system divided into 32 sectors ($9° \times 18°$ field of view each) and with a cut-off energy of 70 keV. ENAs were then either converted to ions or reflected as neutrals onto a target block (angle of incidence $\sim 20°$) towards an MCP with 32 anodes. To reduce UV contamination, the target block was coated with DAG-213, a resin-based graphite dispersion that suppresses UV reflections (see Section 3.4 for calibrations with such coatings against Lyman-$\alpha$ photons). One sector pointing towards the sun was blocked. During one half spacecraft spin the PIPPI sensors covered almost $4\pi$. The design of the ENA sensors described in this thesis is to a large extent based on the PIPPI instrument. The ASPERA-3 and ASPERA-4 NPIs are based on PIPPI-MCP and the NUADU instrument is based on PIPPI-SSD.

The Medium Energy Neutral Atom (MENA) imager [*Pollock et al.*, 2000] on IMAGE measures ENAs in the range 1-70 keV (hydrogen) and 3-70 keV (oxygen). Fig. 1.14 shows an illustration of the MENA sensor. Behind a charged particle deflection system are UV transmission gratings to reduce the UV intensity on the START foil directly underneath them. Electrons generated at the START foil are accelerated towards a START segment on a position-sensitive MCP detector. The ENA

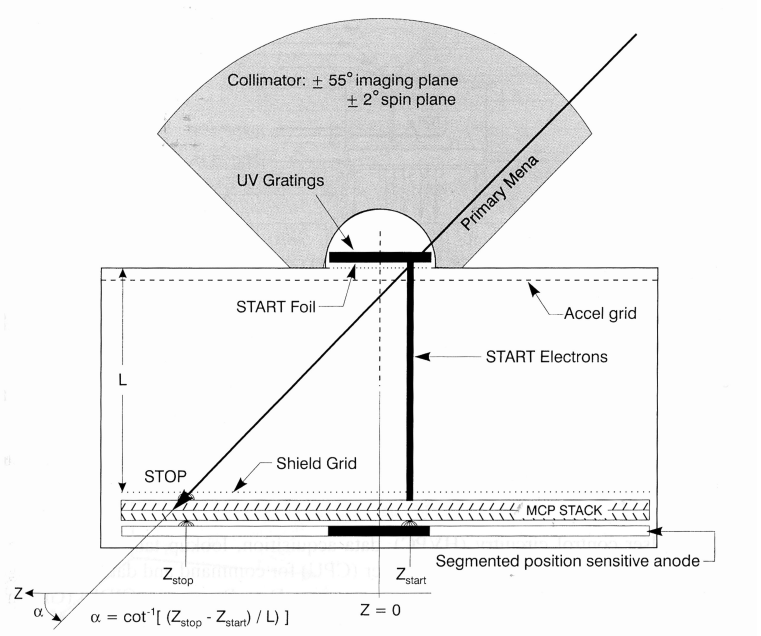


Figure 1.14: Principal of the MENA instrument on the IMAGE spacecraft. From *Pollock et al.* [2000].

continues towards the STOP segment on the position-sensitive detector. Energy is then deduced from TOF measurements between START and STOP pulses, and mass determination between H and O comes from MCP pulse height analysis. Angular resolution of MENA is 5°-12° for O and 5°-8° for H.

The Low Energy Neutral Atom (LENA) imager [*Moore et al.*, 2000] on IMAGE was designed to measure ENAs of energies $\sim$ 10-750 eV. The sensor is based on an atom-to-negative conversion technique. The concept of LENA is shown in Fig. 1.15, where the particle paths through the different sensor sections are visible. ENAs are passed through a charged particle deflection/collimator system with a cut-off energy of $\sim$ 100 keV for singly-charged particles. ENAs then enter the conversion surface system through a pinhole of $\sim$ 1 cm$^2$. A near-conical Tungsten conversion surface at a 15° grazing angle of incidence converts the ENAs to negative ions. The surface itself is negatively-biased to accelerate the newly-created negative ions away from the surface toward an ion optics system. The ion optics system in LENA is made up of an extraction lens to extract and map the ions according to their energy onto the entrance of an electrostatic analyzer. Photoelectrons and other electrons are removed with a broom magnet at the entrance to the analyzer. At the exit from the analyzer the ions enter a TOF cell composed of a carbon foil ($\sim$ 2 $\mu$g/cm$^2$), an electrostatic mirror, and MCP detectors. The angular resolution (FWHM) of the LENA sensor is 8° $\times$ 8°.

Since 1968, the development of ENA instruments has matured and they are today receiving

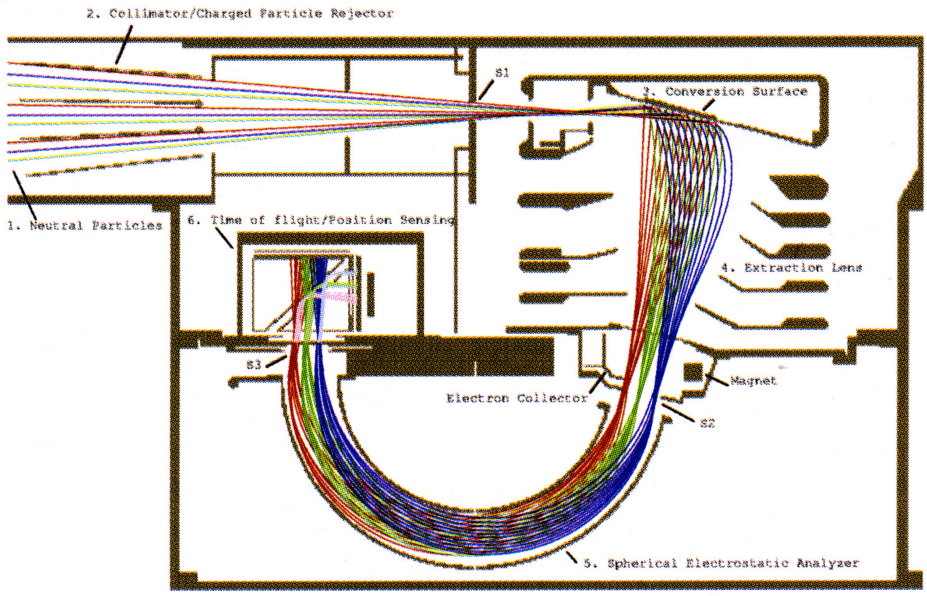


Figure 1.15: Principal of the LENA instrument on the IMAGE spacecraft. From *Moore et al.* [2000].

increasing attention as a useful tool to diagnose large-scale plasma interactions remotely. This chapter has reviewed the main building blocks of ENA detection and examples of existing ENA sensors that measure ENAs in the high, medium, and low energy ranges. In the following three chapters the attention is turned to the development of three ENA sensors for measurements at Mars, Venus and the Earth.

# Chapter 2

# Mars

*A child of five would understand this. Send someone to fetch a child of five.*
– Groucho Marx

*If it looks like a duck, and quacks like a duck, we have at least to consider the possibility that we have a small aquatic bird of the family anatidae on our hands.*
– Douglas Adams

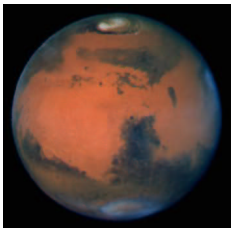

**Mariner 4 was the first spacecraft to visit Mars in 1965. Many others have since followed. Currently there are three spacecraft operating in Mars orbit (Mars Global Surveyor, Mars Odyssey, and Mars Express). The planet is about half the size of the Earth with a radius of $R_m = 3393$ km. Its orbit around the sun is elliptical enough to cause a major influence on the Martian climate with a temperature variation of about 30° C at the subsolar point between aphelion and perihelion, also causing large variations in the surface temperatures all over the planet. The Martian atmosphere is very thin and mainly composed of carbon dioxide (95.3 %), nitrogen (2.7 %), argon (1.6 %) and traces of oxygen (0.15 %) and water (0.03 %). The average pressure on the surface of Mars is less than 1 % of Earth's surface pressure. There are permanent ice caps at both poles composed of water ice and solid carbon dioxide ("dry ice"). Measurements have recently shown that there may also be water ice hidden below the surface at lower latitudes and the NASA Mars Exploration Rovers have indicated that large water deposits may have been present on the Martian surface in the past. A weak crustal magnetic field exists in various regions of the southern hemisphere of Mars. No large scale magnetic field is present, which may have important implications for the Martian atmosphere evolution.** [1]

[1] Reference: Bill Arnett, www.nineplanets.org

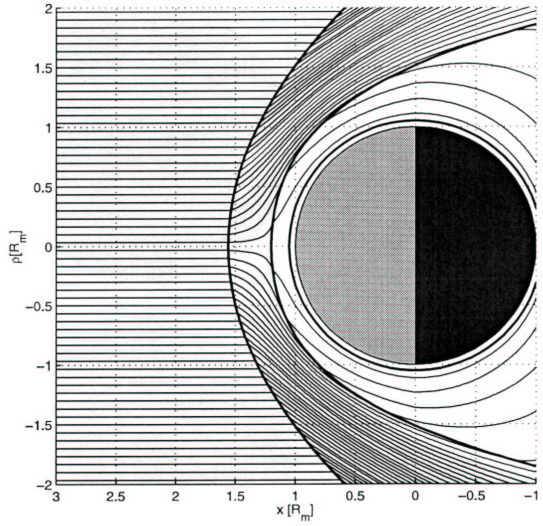


Figure 2.1: Proton streamlines around Mars from the empirical model [*Kallio*, 1996]. Bow shock, IMB and obstacle boundary are drawn in the figure. Figure from *Holmström et al.* [2002].

## 2.1 ENAs at Mars

Before the arrival of Mars Express at the red planet in December 2003, there had not been any spacecraft carrying ENA instrumentation in Martian orbit. Consequently, what was known about ENA emissions at Mars all came from simulations and models. Any ENA simulation is based on a model describing ion distribution, a model of the background neutral gas distribution (mainly hydrogen and oxygen exospheres) and the charge exchange/stripping cross sections. At Mars, the atomic and molecular hydrogen exosphere and oxygen models used come from *Krasnopolsky and Gladstone* [1996] and *Zhang et al.* [1993]. In 1996, *Kallio* [1996] developed an empirical model of the proton velocity flow around Mars that includes this region (Fig. 2.1). It is based on ion observations made by the first ASPERA instrument on the Phobos 2 spacecraft in 1989. It is on this empirical flow model that most ENA studies prior to Mars Express orbit insertion at Mars have been based. Different studies have looked at hydrogen ENAs originating from solar wind protons and ENAs of planetary origin. *Kallio et al.* [1997] describe the generation of ENAs from the charge exchange process between solar wind protons and the Martian neutral upper atmosphere for solar minimum and maximum conditions. *Holmström et al.* [2002] investigated the sensitivity of simulated ENA images to varying model parameters. They also looked at backscattered ENAs from the dayside of Mars, sometimes called the ENA albedo. ENAs of planetary origin have been discussed in *Barabash et al.* [2002] and *Lichtenegger et al.* [2002]. *Gunell et al.* [2005b] study the effect that different ion distribution models have on ENA images. They compare the empirical model by *Kallio* [1996], MHD and hybrid models. ENA-generation in the solar wind interaction with the Martian moon Phobos is considered by *Mura et al.* [2002]. What follows here is a summary of previous studies to

give an account of the different ENA sources around Mars and their characteristics.

There are five main identified/proposed ENA sources near Mars. They are:

1. ENAs from the undisturbed solar wind interaction with the extended exosphere (detected).
2. ENAs from the shocked solar wind region between the bow shock and induced magnetosphere boundary, IMB (also known as the ENA jet) (detected).
3. Backscattered ENAs from the Martian upper atmosphere (ENA albedo) (detected).
4. ENAs from picked up ions that are accelerated and later charge exchange (not detected).
5. ENAs from the solar wind interaction with the Phobos and Diemos tori (not detected).

The first ENA source is the solar wind itself before it reaches the Martian bow shock. The solar wind contains a small neutral component even at large distances from planets. These ENAs are generated in charge exchange processes between the solar wind protons and the background interplanetary neutral gas with typical density $\sim 0.1$ cm$^{-3}$. *Collier et al.* [2001] reported measurements of solar wind ENAs from Earth orbit and concludes the energy to be same as solar wind energies and intensities around $7.0 \times 10^3$ cm$^{-2}$ sr$^{-1}$ s$^{-1}$ ($10^{-3} - 10^{-4}$ of the total solar wind). The Martian atmosphere, though thin, extends far from the planetary surface. Measurements of the Lyman-$\alpha$ line on the Mariner 6 and 7 missions found that the exosphere of neutral hydrogen extends further than 22,500 km above the Martian surface [*D. E. Anderson and Hord*, 1971]. At these altitudes the density is low ($1.6 \times 10^2$ cm$^{-3}$), but still orders of magnitude higher than the background interplanetary neutral gas. As the neutral density increases even more closer to the planet the in comparison with the ENA intensity from the solar wind direction is increased from $7.0 \times 10^3$ cm$^{-2}$ sr$^{-1}$ s$^{-1}$ or lower to $10^6$ - $10^7$ cm$^{-2}$ sr$^{-1}$ s$^{-1}$. The energies of such ENAs are close to the solar wind energy ($\sim 0.7 - 1.0$ keV). There is also a certain spreading from the solar wind direction. The reason for that is the inherent temperature of the solar wind ions when they charge exchange with the neutral exosphere and become ENAs. The solar wind ENAs can propagate unaffected through the main plasma boundaries at Mars and finally precipitate onto the Martian upper atmosphere and can contribute to the heating of the upper exosphere [*Kallio and Barabash*, 2001]. Section 2.5.2 presents measurements of solar wind ENAs propagating through the Martian atmosphere in the terminator region and spreading into the eclipse of Mars.

Inside the bow shock, but outside the IMB, a second population of ENAs is born in the solar wind interaction (Fig. 2.2). This volume is populated with shocked solar wind protons of lower bulk energy, but higher temperature. The reactions that create this ENA population are predominantely:

$$\begin{aligned} H^+_{sw} &+ H_{cold} \longrightarrow H_{ENA} + H^+_{cold} \\ H^+_{sw} &+ O_{cold} \longrightarrow H_{ENA} + O^+_{cold} \\ H^+_{sw} &+ H_{2cold} \longrightarrow H_{ENA} + H^+_{2cold} \end{aligned}$$

where the subscripts denote 'sw' and 'cold' for solar wind or planetary origin, respectively. The reaction involving He atoms is not included because that reaction has a much lower cross section ($\sim 10^{-22} - 10^{-19}$ cm$^2$) for the energies in question (see Fig. 1.3) and therefore does not contribute

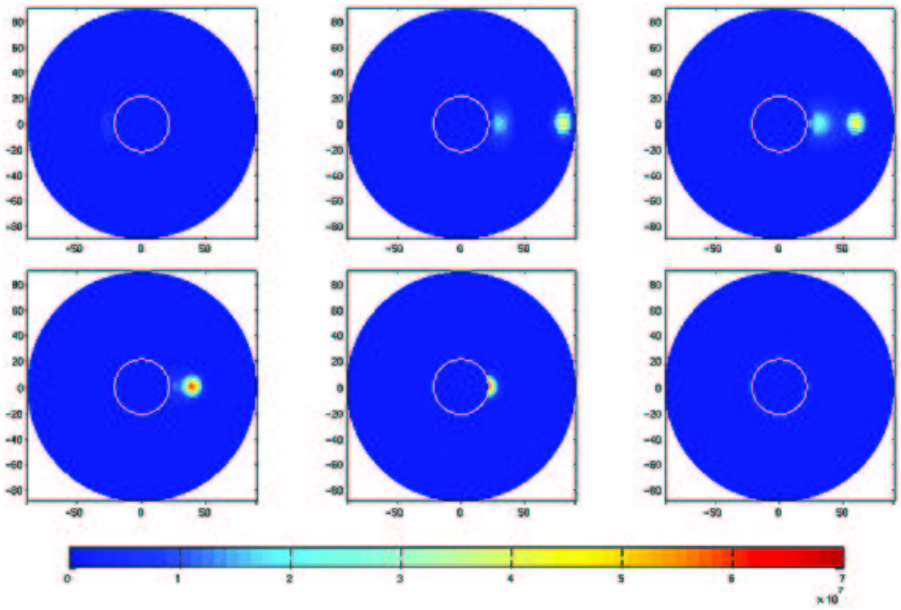

Figure 2.2: Simulated ENA images of charge exchanged solar wind protons from a distance of $3R_m$ from the center of Mars. The plots are polar representations of an 180° field of view. The axes show the angle to the look direction. The white circle is the impenetrable planetary obstacle (1.05 $R_m$) and the angle between the view position and the Mars-sun line (the solar zenith angle, SZA) is, from left to right, top to bottom, 80°, 100°, 120°, 140°, 160°, and 180°. The color scale is the flux in $\mathrm{cm}^{-2}\ \mathrm{sr}^{-1}\ \mathrm{s}^{-1}$. Figure is from *Holmström et al.* [2002].

very much to the ENA generation. This ENA population has generally lower energies than the ENAs from the solar wind. The thermalisation of the plasma flow as it passes the bow shock translates to an energy spread in the generated ENAs and the predicted energies ranging from tens of eV to over 1 keV. Measurements of ENAs from the ENA jet are presented in Section 2.5.1.

As mentioned, some of the hydrogen ENAs generated in (1) above will precipitate onto the Martian upper atmosphere. Monte-Carlo simulations of the precipitation process show that a majority ($\sim$ 60 %) of the precipitated flux are backscattered [*Kallio and Barabash*, 2000]. The remaining flux deposits energy in the upper atmosphere of Mars. Simulations of ENA imaging give highest intensities from backscattered ENA from vantage points 30° away from the Mars-sun line [*Holmström et al.*, 2002].

The fourth ENA population arises from ions of planetary origin. Apart from the charge exchange process described earlier, ionization due to solar UV photons and thermalized electrons (electron impact ionization) of neutral particles in the Martian upper atmosphere can take place. In all cases the product is an initially cold planetary ion. In the magnetic and electric fields such ions (mostly $O^+$), moving on cyclical trajectories, will rapidly gain energy higher than the escape energy of 2.1 eV for oxygen (an electric field strength of 1 mV/m would accelerate a singly charged oxygen ion

to the escape energy over a distance of 2.1 km). Such ions can then form planetary ENAs from a second charge exchange process in one of the following reactions:

$$
\begin{array}{lcllcl}
H^+_{pl} & + & H_{pl} & \longrightarrow & H_{ENA} & + & H^+_{pl} \\
H^+_{pl} & + & O_{pl} & \longrightarrow & H_{ENA} & + & O^+_{pl} \\
H^+_{2pl} & + & H_{2pl} & \longrightarrow & H_{ENA} & + & H^+_{2pl} \\
O^+_{pl} & + & H_{pl} & \longrightarrow & O_{ENA} & + & H^+_{pl} \\
O^+_{pl} & + & O_{pl} & \longrightarrow & O_{ENA} & + & O^+_{pl} \\
O^+_{pl} & + & H_{2pl} & \longrightarrow & O_{ENA} & + & H^+_{2pl}
\end{array}
$$

It is anticipated that about 50 % of the oxygen ions go through charge exchange to form planetary oxygen ENAs [*Barabash et al.*, 2002]. A portion of these ENAs can subsequently escape the planet, while others precipitate back onto the Martian upper atmosphere. Simulations of both oxygen and hydrogen show that there are strong asymmetries of the flow of such ENAs along the direction of the electric field. Energy spectra from the hydrogen simulations suggest that instrumentation with sufficient energy resolution should be able to separate planetary hydrogen ENAs from solar wind ENAs [*Lichtenegger et al.*, 2002]. Oxygen ENAs mostly have energies of 600 eV or below [*Barabash et al.*, 2002].

The final ENA source near Mars are ENAs found in the solar wind interactions with the Phobos and Deimos moons. Depending on the origin of those satellites they can contain amounts of oxygen in the form of $H_2O$ that in turn can evaporate to space, forming a neutral gas torus around Mars at the orbit of each of the moons. ENAs would then be generated in the solar wind interactions with this torus. Phobos 2 spacecraft data showed possible out-gassing rates from Deimos of $10^{24}$ $s^{-1}$ [*Sauer et al.*, 1995] as well. Further studies have shown that, if such an evaporation rate is applicable also for Phobos, the neutral density in the immediate vicinity of the moon could be as high as $\sim 3 \times 10^4$ $cm^{-3}$ [*Mura et al.*, 2002]. Such densities of ENA production from the Phobos torus could be high and should be measurable from a number of vantage points even with a background of shocked solar wind ENAs. As for the ENA emissions from Mars, the energies range up to solar wind energies.

Fig. 2.3 summarizes the different sources of ENAs around Mars (Phobos and Deimos tori not included). All these emissions are added to form the ENAs from the Martian system. As their respective directionality and energy spectra differ it should be possible to separate and identify the different sources with proper instrumentation, i.e., with proper angular and energy/mass resolution. The modelled ENA production from all sources is also sensitive to changes in the parameters of the models. Out of 14 varied parameters it has been shown that the total ENA production is most sensitive to the exobase temperature and therefore also the hydrogen density profile [*Holmström et al.*, 2002]. The flow geometry of the ENAs around Mars is most sensitive to the position of the modeled magnetopause. Solar wind temperature and proton flux were also found to be important parameters.

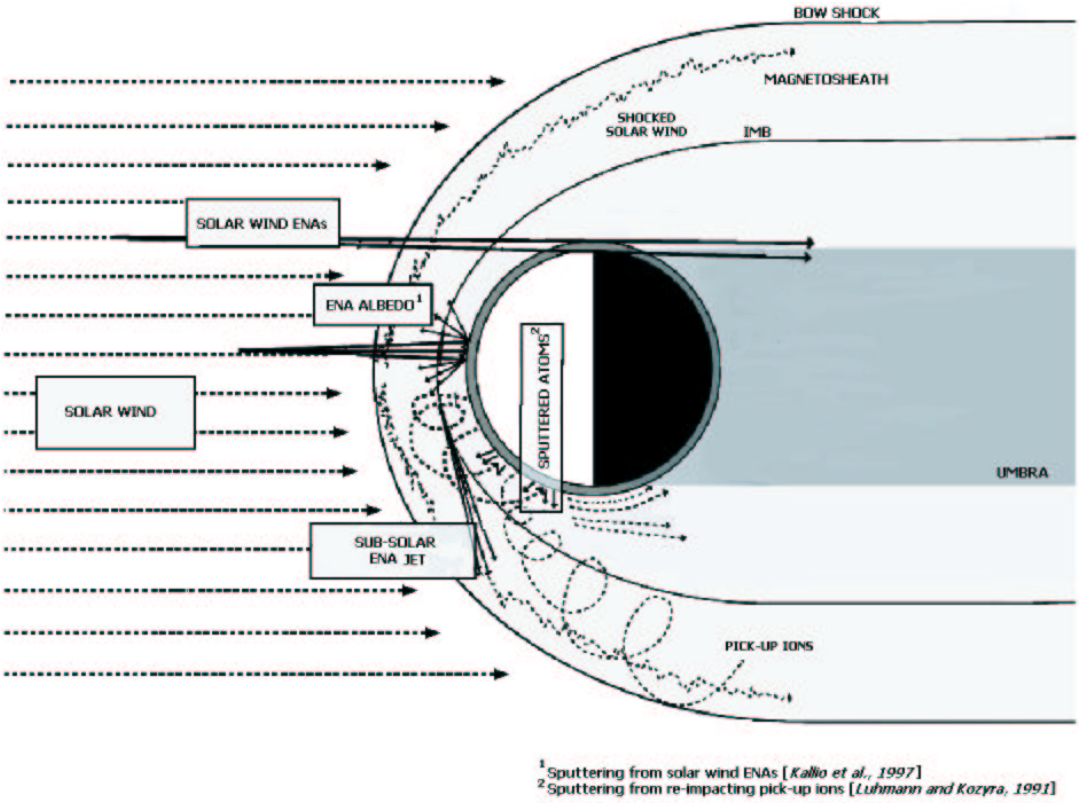


Figure 2.3: Illustration of the ENA production regions at Mars from models. Solar wind ENAs are produced by charge exchange between the solar wind ions and the extended exosphere in front of the bow shock. The ENA albedo is produced by the solar wind ENAs and pick-up ions precipitating the upper atmosphere [*Futaana et al.*, 2005a]. The subsolar ENA jet is produced where the subsolar deflection point of the solar wind flow lines occurs in high neutral gas density close to the planet [*Futaana et al.*, 2005b; *Gunell et al.*, 2005a]. Figure from *Brinkfeldt et al.* [2005].

## 2.2 Mars Express and ASPERA-3

Mars Express is the first European mission to another planet and was launched on June 2, 2003, on a Soyuz/Fregat launcher from Baikonur, Kazakhstan. The orbiter wet mass was 1223 kg, and on-board was also the unsuccessful Beagle 2 lander with a mass of 60 kg. On December 19, 2003, Beagle 2 was separated from the orbiter, but contact with it was never established. The orbiter was successfully inserted into Mars orbit six days later on December 25, 2003, and is still operational at the time of writing. Mars Express is in an elliptical, polar orbit around Mars. The inclination is 86°. The pericenter of the orbit is currently at 298 km altitude and the apocenter at 10,107 km with an orbital period is 6.7 hours. During the first 440 days of the mission the orbit was slightly more elliptical and had a period of 7.5 hours. As Mars travels around the Sun a part of the Mars Express orbit moves in and out of eclipse during eclipse-seasons. The orbit plane is not fixed in inertial space, which means that there can be more than two Mars Express eclipse-seasons per Martian year. The scientific payload on Mars Express consists of seven instruments to complete the scientific objectives to study the subsurface, surface, and atmosphere of Mars and its interaction with the interplanetary medium.

One of the instruments is the Analyzer of Space Plasmas and Energetic Atoms (ASPERA-3). The Swedish Institute of Space Physics in Kiruna, Sweden is responsible for the instrument. The ASPERA-3 team consists of scientists from 14 different research groups in 11 different countries. The scientific objectives of ASPERA-3 are to map the global distributions of plasma and neutral gas in the vicinity of Mars and to study the effects the solar wind has on the ionosphere and atmosphere including investigations of plasma-induced atmospheric escape. To meet these objectives the instrument has to be able to measure electrons, ions and ENAs. ASPERA-3 consists of five sensors (Fig. 2.4): the electron spectrometer (ELS), the ion mass analyzer (IMA), the neutral particle imager (NPI), and two identical neutral particle detectors (NPD1 and NPD2). The ELS is a top-hat type electrostatic analyzer in the energy range 1 eV - 20 keV with a 360° field of view divided into 16 sectors. IMA is a 360° top-hat electrostatic analyzer followed by a magnetic velocity analyzer. To provide polar angle coverage, the top-hat analyzer is equipped with an electrostatic deflector sweeping polar angles between ±45° angular range. IMA measures ions from 1 eV-36 keV and resolves $H^+$, $He^{++}$, $He^+$, $O^+$, and molecular ions. NPD and NPI both measure ENAs, but build on different principles. The NPDs have energy and mass resolution, but poor angular resolution, while the NPI does not provide mass or energy resolution, but has high angular resolution. An analogy to photographic cameras can be made, in which the NPDs are cameras that take very blurred pictures, but in color, while the NPI can take sharper pictures, but only in black and white. The NPD principle is based on a surface reflection technique and measurements of TOF between hits on START and STOP surfaces. Mass identification is provided by TOF measurements. Since only two species, hydrogen and oxygen, are expected, the difference in their TOF while they travel 8 cm is sufficient to resolve these ENAs over the energy range of interest. There are two identical NPD units on ASPERA-3 facing different directions in space. The NPI sensor is presented in detail in the next section.

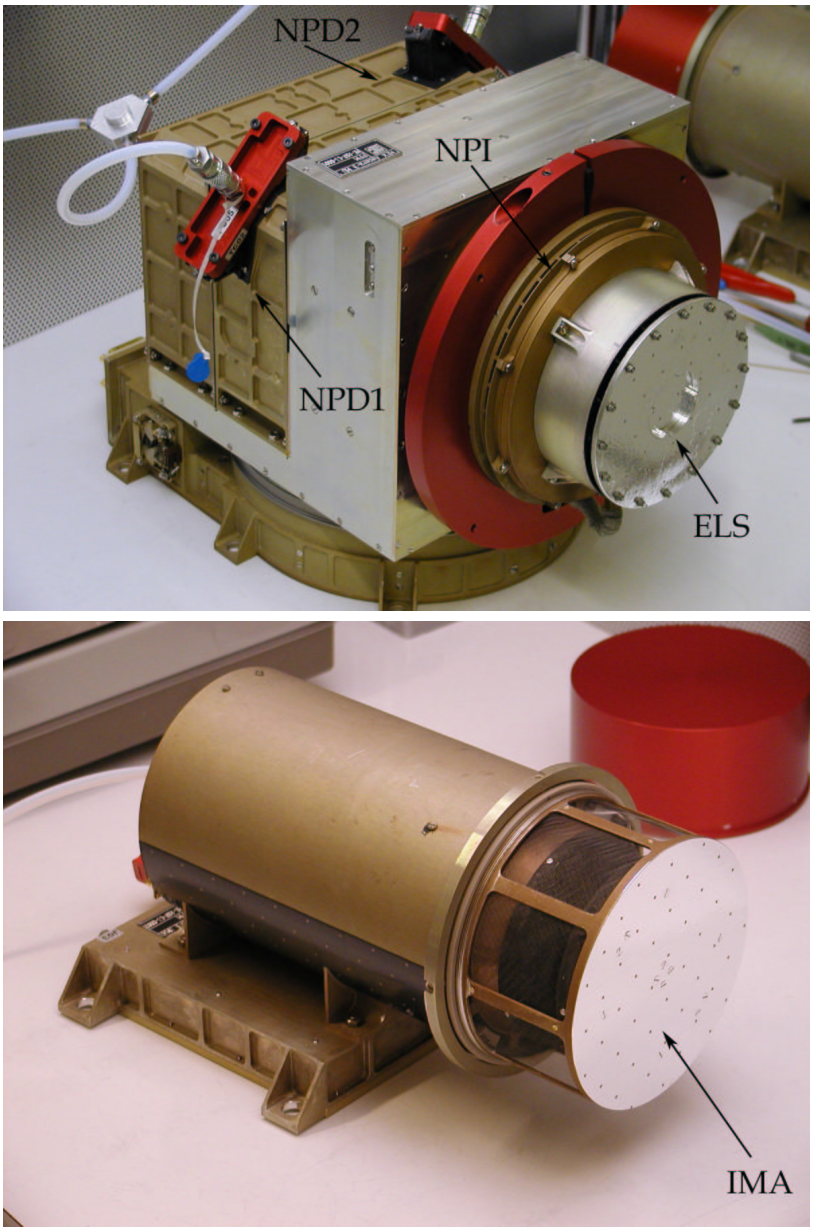


Figure 2.4: The ASPERA-3 instrument consists of five different sensors: The Electron Spectrometer (ELS), Neutral Particle Imager (NPI), and Neutral Particle Detector (NPD1 & NPD2) are mounted on the ASPERA-3 Main Unit (top). The Ion Mass Analyzer (IMA) (bottom) is separated from the Main Unit.

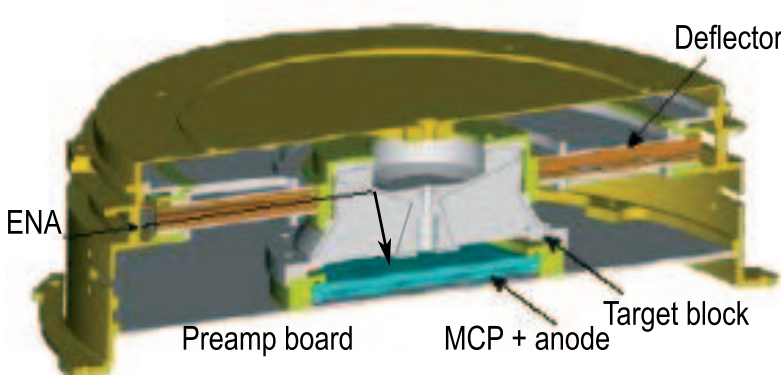


Figure 2.5: Cut-away illustration of the NPI. ENAs pass through the deflection system and are reflected from the target block towards the MCP plates.

## 2.3 NPI general design

The Neutral Particle Imager (NPI) is a $9° \times 337.5°$ ENA imager with the field of view sectioned into 32 sectors, each with a $11.25° \times 4.6°$ field of view (FWHM). The NPI design is based on the PIPPI-MCP ENA imager on-board the Astrid spacecraft (see Section 1.2.6). NPI is placed on a scanning platform that rotates the sensor 180 degrees in 32 s. This scanning provides full coverage of space for the NPI except for the solid angle blocked by the spacecraft body. Charged particles of energies up to 60 keV are rejected in an electrostatic deflection system. The neutrals hit a central target block and are reflected (or converted to ions, then reflected) towards a micro channel plate (MCP). The target block itself is coated with DAG-213, which is a resin based graphite dispersion similar to aqua-DAG. It is chosen to minimize reflections of UV photons from the target block, while, as efficiently as possible, convert ENAs to secondaries. Two sectors, numbers 15 and 16, are mechanically blocked and used to monitor the MCP dark count. The apertures of those sectors were simply not cut open. A cut-away view of NPI is shown in Fig. 2.5. Fig. 2.6 shows photographs taken during the integration of the ASPERA-4 NPI.

The MCP assembly is in chevron configuration and operated in ion mode (negative high voltage on the front plate). The gain of the MCP stack is $\sim 10^6$. At the MCP output, a 32-sectioned anode connected to front end electronics collects the electron shower from the MCPs on one of its sections. The charge pulse is fed to a charge-sensitive preamplifier, which also generates a TTL level signal. NPI does not have its own signal processing and interfaces with the ASPERA-3 central data processing unit (DPU) via an Actel 1020 FPGA. After each hit the NPI FPGA generates a READY signal and puts the sector address on the five address lines After DPU read-out of the address lines it resets the FPGA via a RESET line. 32 16-bits counters are located on the DPU side. The counter read-out occurs every 62.5 ms for further processing. Therefore, once per sampling time the DPU reads out a 32 element array containing the ENA count rates from 32 different directions. Hits received during the READY pulse ($\approx$200 ns) are ignored (sensor dead time).

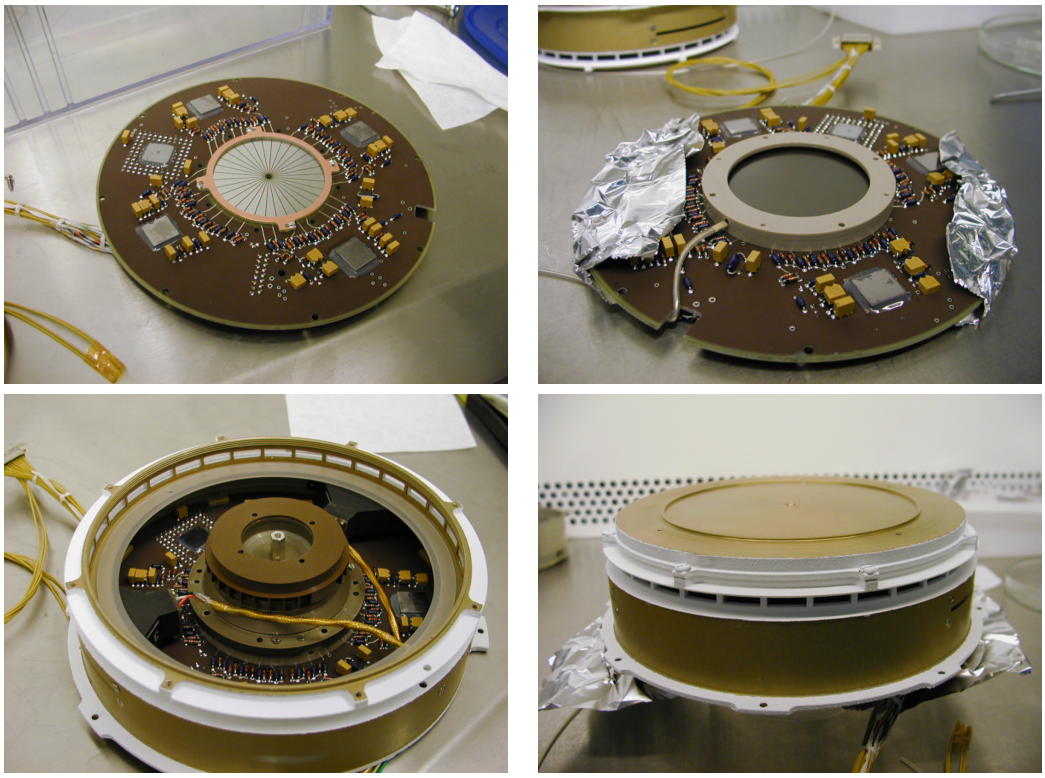

Figure 2.6: Integration pictures of the ASPERA-4 NPI. Top left shows the NPI electronics board with the anode sectors. In the upper right image the MCP stack has been integrated. The bottom left shows the target block in position and the board is now mounted in the NPI housing. The integrated NPI is shown in the lower right image.

NPI uses four Monolithic Octal Amplifier Discriminator (MOCAD) preamplifiers. Each MOCAD contains 8 channels with both analog and digital outputs and adjustable thresholds (one threshold per MOCAD or 8 channels). Only the digital outputs are used in the NPI. These are connected to the FPGA. The FPGA loops a program in which it checks if a hit was in sector 31, 30, 29, ... 0. This means that there is a programmed priority in case of two simultaneous hits since it first checks sector 31 and last sector 0. Simultaneous hits on the sectioned anode are thus always counted in the higher sector. During calibration of the NPI it was found that neighboring sectors are affected whenever there is a count. Because of the programmed priority this results in a sector drift effect in the sensor. The effect is further explained in Section 2.4. Fig. 2.7 shows a block diagram of the NPI. A summary of the NPI characteristics are found in Table 2.1.

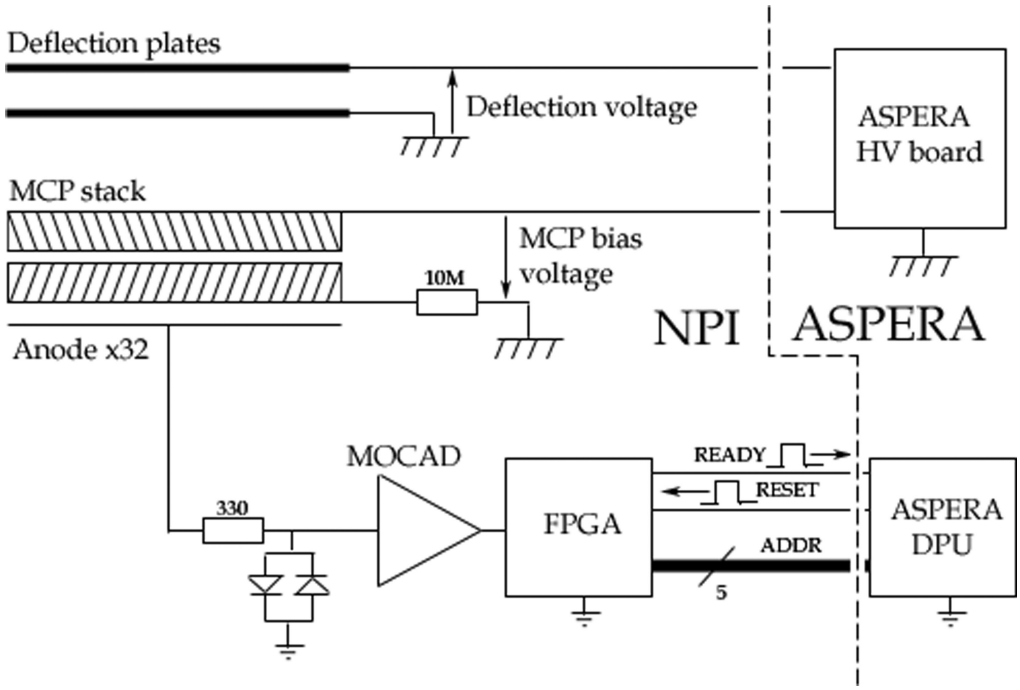


Figure 2.7: Block diagram of the NPI. High voltage for deflection system and MCP stack is provided by a central HV board in the ASPERA Main Unit. The signal from the 32 anodes (corresponding to the 32 sectors) is amplified and digitalized in four different MOCAD preamplifier packages (8 sector anodes per package). The FPGA then transforms each digital hit into a 5-bit address corresponding to the anode that received the hit. The address (ADDR) is then sent to the ASPERA data processing unit after a READY signal enables it to be read. When the address is read the DPU sends a RESET signal to the NPI FPGA.

## 2.4 ASPERA-3/NPI calibrations

The calibration facility at the Swedish Institute of Space Physics in Kiruna, Sweden, houses two ion sources with energies of 0.4-25 keV and 0.02-50 keV that provide large diameter (10 cm) parallel beams of a selected energy and mass and with variable intensity. The systems are also equipped with turntables having four degrees of freedom. The system used for the NPI particle calibration is the Model 2751 50 keV Ion Source from Peabody Scientific. It is capable of producing a parallel and evenly distributed ion beam with an energy of up to 50 keV/q. The system can be run in three different modes to be able to achieve the three energy ranges 0 - 1 keV/q, 1 - 15 keV/q and 15 - 50 keV/q. The system is shown schematically in Fig. 2.8.

Ions are produced in the duoplasmatron in discharge between an anode and a filament coated with $Ba_2CO_4$ to increase electron emission. To increase the ionization efficiency, a strong magnetic field is applied in the axial direction of the duoplasmatron. The generated electrons spiral along

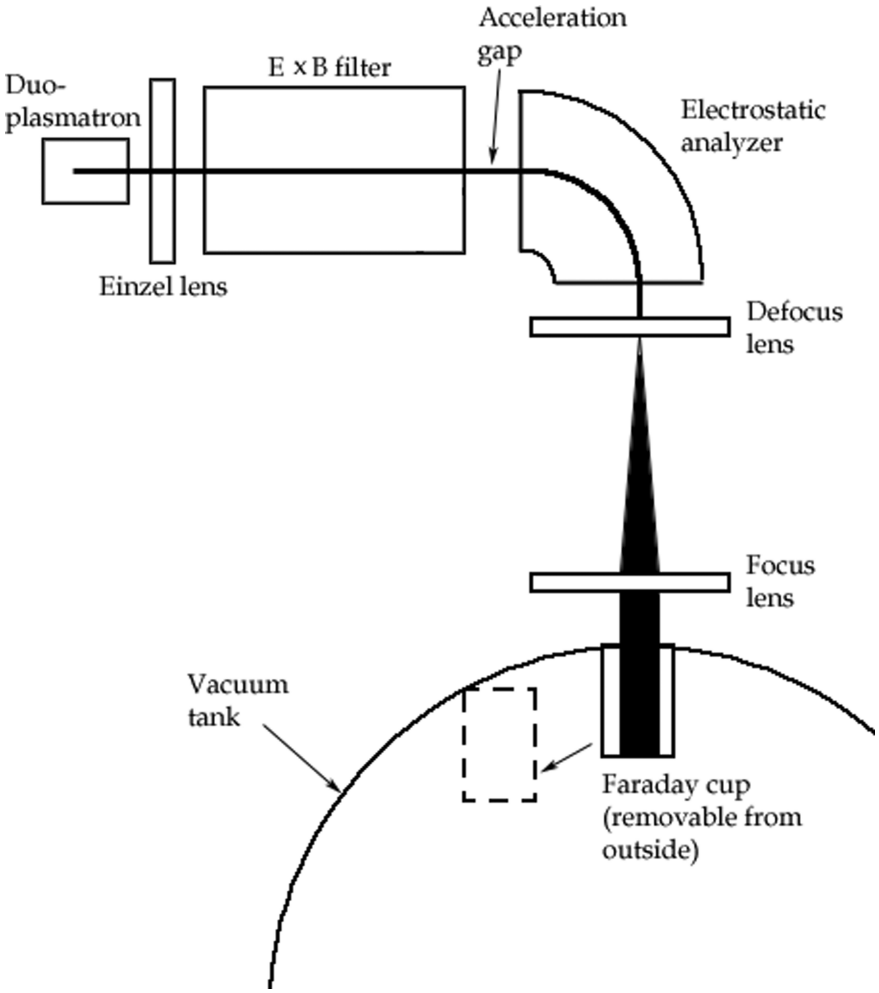


Figure 2.8: Illustration (not to scale) of the ion source at the Swedish Institute of Space Physics in Kiruna, Sweden.

Table 2.1: NPI characteristics.

| **Parameter** | **NPI** |
|---|---|
| Particles to be measured | ENA |
| Energy, keV per charge | ~0.1-60 |
| Energy resolution, $\Delta E/E$ | - |
| Mass resolution | - |
| Intrinsic field of view | $9 \times 344°$ |
| Angular resolution, FWHM | $4.6 \times 11.5°$ |
| G-factor/pixel, $cm^2$ sr | $2.7 \cdot 10^{-3}$ |
| Efficiency, % | $\sim 0.1$ (at 1 keV) |
| Time resolution (full 3D), s | 32 (one scan) |
| Sampling time (min), ms | 62.5 |
| Mass, kg | 0.7 |
| Power, W | 0.8 |

the magnetic field lines towards the anode and produce longer ionization tracks. The ion beam is then extracted through an extraction gap by an extraction electrode and then accelerated through a three-element Einzel focusing lens, which also collimates the diverging ion beam into a parallel beam. The focal length can be optimized by adjusting the lens voltage. The ions then enter an E×B Wien filter. This consists of a perpendicular magnetic and an electric field. The electric field can be varied to balance the magnetic force so that the desired ion mass can pass through the system. Exiting the E×B filter, the ions are accelerated in an acceleration gap to achieve the final beam energy. The beam is then guided through a 90° electrostatic analyzer, with a central radius of 12.7 cm. This is made to prevent the strong neutral beam that exits the duoplasmatron from reaching the vacuum tank. The electrostatic analyzer in the system has an energy resolution of 1 %. To permit widening of the ion beam that emerges from the electrostatic analyzer, a defocus lens first diverges the beam and then a focus lens collects the diverging beam into a parallel beam used for calibration. Both lenses are three-element Einzel lenses of different sizes. The retractable Faraday cup provides measurements of the beam intensity and because of this also indirectly the beam location. It is mounted inside the vacuum tank.

The NPI response to particles was measured using the system described. The target block reflection and MCP response in the NPI is similar for ions and neutrals. Therefore the NPI was fully calibrated using ions with the deflection system switched off. Then the calibration was verified using neutrals generated in a drift tube in the ion source. These neutrals result from charge exchange between the beam ions and the residual gas in the system. There is also a small (25 % of total amount of neutrals) contribution from neutrals generated in the duoplasmatron that pass through the system. For the energies in question the ion beam always contains 1 %-5 % of neutrals [*Barabash*, 1995] depending on beam energy and pressure in the tank. The sensor itself was placed on the turntable (4-degrees of freedom) inside the system and subjected to a parallel beam of ions

Table 2.2: Calibrations and functional tests performed on the ASPERA-3 NPI.

| Test | Species | Energy |
|---|---|---|
| Effect of priority scheme on angular response | $H^+$, $H_2O^+$ | 4.8, 9.6 keV |
| Dark current calibrations | – | – |
| Angular response function calibrations | $H_2^+$ | 4.8 keV |
| Relative response calibrations | $H_2^+$ | 4.8, 9.6 keV |
| Efficiency calibrations | $H_2O^+$ | 0.29, 0.48, 0.96, 4.8 keV |

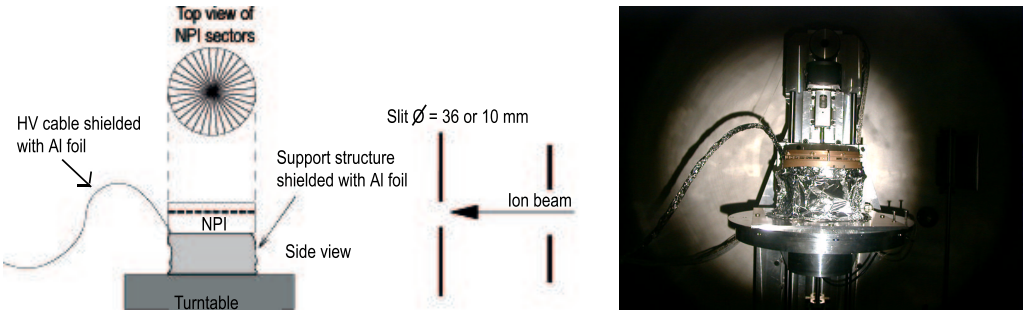


Figure 2.9: Illustration of the calibration configuration. The calibration beam enters from the right. The NPI was placed on a shielded support structure attached to a turntable with four degrees of freedom inside the calibration tank.

of different mass at different energies. The calibrations and functional tests performed as well as the species and energies used in the calibration beams are listed in Table 2.2. The calibration set-up inside the tank is shown in Fig. 2.9.

### 2.4.1 Priority effect

During calibration of the NPI a sector drift effect toward higher numbered sectors at high MCP bias was found. When the beam was incident on one sector the resulting counts shifted toward the next sector in the clockwise direction (i.e. toward higher sector numbers) when the MCP bias increased (see Fig. 2.10). The NPI electronics have a programmed priority for dealing with counts that occur within a short time period ($\sim$ 200 ns) on two different sectors. In the event that this happens, the higher numbered neighboring sector is awarded the count. With this in mind the drift could be explained as a large area (spanning across sector boundaries) charge cloud forming between the MCP and anode for every count. The charge cloud would be split between two sectors resulting in two (or even more) simultaneous pulses. Because of the priority scheme this would then be manifested as a sector drift to a higher sector. Alternatively, there might be stray capacitive couplings between neighboring sectors proportional to MCP bias. The signal on one sector could be coupled to neighboring sector anodes and the drift effect would again result from the sector priority

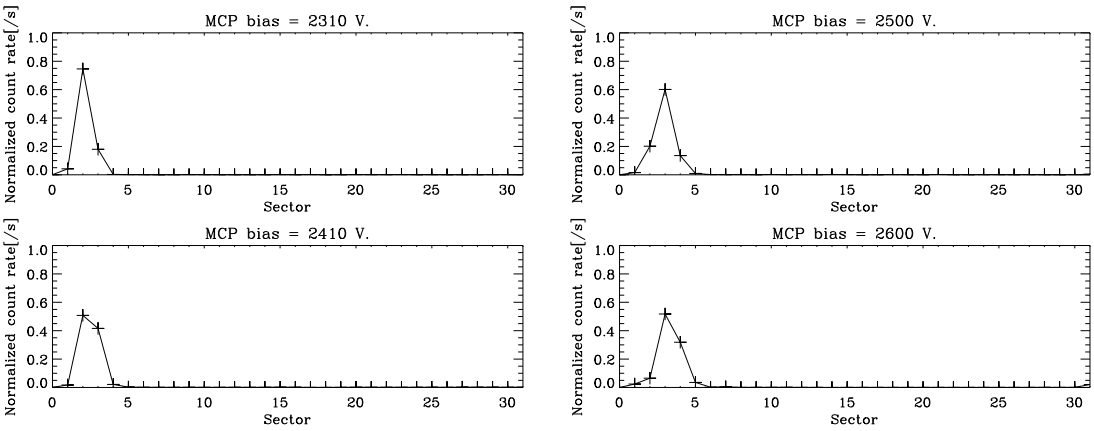


Figure 2.10: Measurements with the calibration beam directed into the same NPI sector (number 2) for different MCP bias. There is a clear shift of the response into higher numbered sectors with MCP bias.

scheme.

To investigate the effect further, the deflector and lid of the NPI was removed and the sensor was mounted perpendicular to the ion beam (as in Fig. 2.11). The count rates were then measured

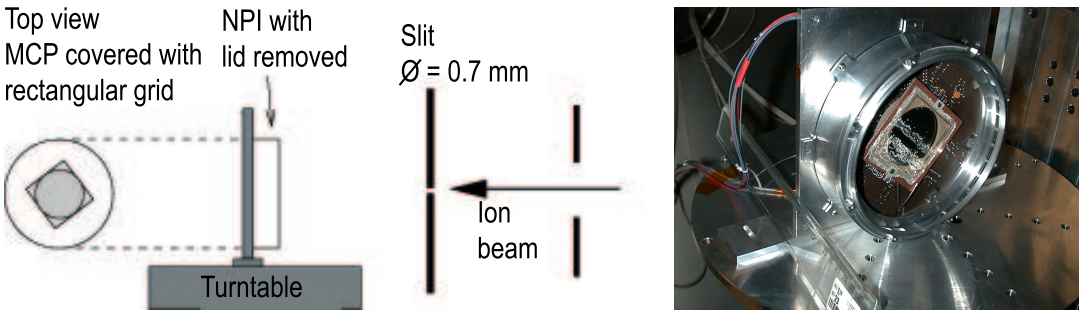


Figure 2.11: The priority effect was further investigated using the set-up shown. Lid, deflector plates and target block were removed and the NPI with the bare MCP covered with a rectangular grid was mounted on the turntable perpendicular to the 0.7 mm diameter pencil beam.

at three different positions, A, B and C (Fig. 2.12), along the central line of sector 15, where A was near the center (where the anode sectors are narrow and therefore closer together), B was half way between edge and center, and C was near the edge of the MCP (where the anode sectors are wide). The MCP bias for all measurements was 2600 V. A charge cloud with an area large enough to cause the sector drift would cause the measurement at point C to have a smaller associated drift than that at point A where the cloud would cover more sectors. The result in Fig. 2.13a, where the sector average based on normalized count rate is plotted for the three points, suggests that this

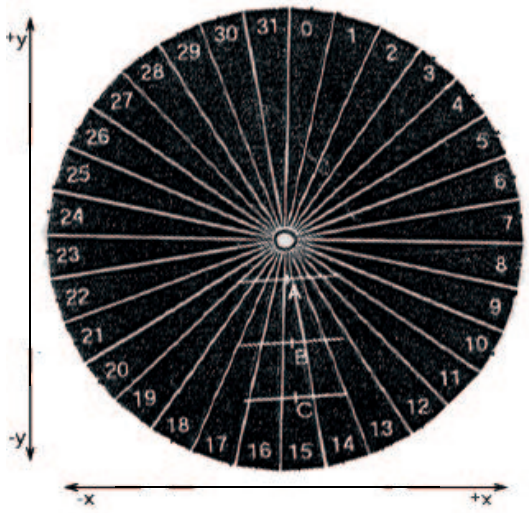


Figure 2.12: The anode layout on the preamplifier board. The lines at the three measurement points A, B and C correspond to 13 mm on the real anode.

could be the case. Close to the center of the MCP the count rate median was between sectors 16 and 17 while close to the edge it was between sectors 17 and 18. An ideal detector would produce counts in sector 15 only.

A rough estimate of the size of such an electron cloud can be made from scans over sector boundaries at low (2210 V) and high (2600 V) MCP bias. The estimate is based on a method to investigate the radial electron cloud distribution between MCP output and a split strip anode [*Edgar et al.*, 1989]. Because of the symmetry of the anodes of two neighboring sectors in the NPI, measuring the fraction of count rates for one sector to its neighbor at different points across a sector boundary at low MCP bias will produce the S-shaped curves in Fig. 2.13b. This method was used to estimate the size of the low bias MCP electron cloud. Scans were then made at high MCP bias to find the size increase, $\Delta r$ produced by the sector priority effect. The sectors used are 6, 7, and 8 for a vertical scan and 15, 16, and 17 for a horizontal scan. The charge distributions in the x and y direction (x and y directions are defined in Fig. 2.12) at low MCP bias are then found from the derivative of the S-curves. Fig. 2.13c is a plot of the charge distribution for the low MCP bias electron cloud from scans in the x and y directions. From this plot it is suggested that though the electron cloud is not perfectly symmetric in the vertical and horizontal directions (the lines should coincide [*Edgar et al.*, 1989]) the estimated diameter is $\sim 2$ mm in both directions, which is consistent with a typical size of 1 mm.

After estimation of the cloud size at low MCP bias, vertical and horizontal scans over the sector boundaries at high MCP bias was performed. This gave the difference, $\Delta r$, between the two electron cloud radii (the difference in position when counts are first detected in the higher sector for high and low MCP bias). From this the cloud size at high MCP bias could be estimated. Fig. 2.13d

show the normalized count rate in sector 8 during a vertical scan across sectors 6,7, and 8 for both high and low MCP bias. $\Delta r$ is the difference in cloud radius for high and low MCP bias. As shown in Fig. 2.13d $\Delta r \approx 5.5$ mm and added to the measured electron cloud diameter for low MCP bias $r \approx 1$ mm the estimated electron cloud radius for high MCP bias is $r + \Delta r = 6.5$ mm, which is unresonably large.

The approximation of a 13 mm cloud diameter is not consistent with Fig. 2.13a. The figure shows in which sector the average of the counts appears for the different positions A, B, and C. The highest sector in which counts appeared for position A was sector 20; for B and C it was sector 19. The white horizontal lines in Fig. 2.12 correspond to 13 mm and are centered over the positions A, B and C. It is clear that a cloud size of diameter 13 mm would not reach sector 19 as the data indicates at positions B and C, while at A it does. For an electron cloud centered at position C to include sector 19, its diameter would have to be in the order of 30 mm. However, if the cloud has a 13 mm diameter and is equally distributed in the x and y directions at position A it would cover the central part of the MCP and all anode sectors would have counts. With the priority, a large number of these should be registered in sector 31, but the response is not above noise level in that sector.

As mentioned above, two mechanisms would contribute to the priority effect, namely, large electron cloud size and capacitive cross talk. The main contribution seems to come from capacitive coupling. This conclusion is indeed confirmed by the Venus Express ASPERA-4 NPI calibrations, where increasing the MOCAD thresholds cured the problem. Unfortunately, because of the tight time schedule for Mars Express, this was not done on the ASPERA-3 NPI. To reduce the effect of the priority, the operational MCP bias was lowered from the optimal MCP bias based on saturation measurements. Nominal operational MCP bias on the ASPERA-3 NPI is 2310 V.

### 2.4.2 Dark counts

The NPI dark count was measured during 60 seconds without the ion beam. The average count rate ($s^{-1}$) for each of the sectors during 60 seconds for different MCP bias settings are shown in Fig. 2.14. The sector priority effect is visible as a decrease of the count rate in low sector numbers and an increase in high sector numbers for higher MCP bias. The average dark count rate for the nominal 2310 V MCP bias is 0.959 $s^{-1}$. The priority effect is negligible at the nominal MCP bias.

### 2.4.3 Angular response

To determine the angular response of one reference NPI sector (number 14) the sensor was rotated to different positions in azimuth and elevation. The rotation axis was centered in a parallel beam that was sufficiently wide to cover the whole sector aperture at all angles. Fig. 2.15 shows the measured angular response for one sector of the NPI at different MCP biases. Each point on the angular function is an average over 11 seconds. The measurement was made for the species and energy listed in Table 2.2 with the basic shape of the angular function remaining constant. The angular calibration is used to calculate the pure geometrical factor (G-factor) excluding efficiency

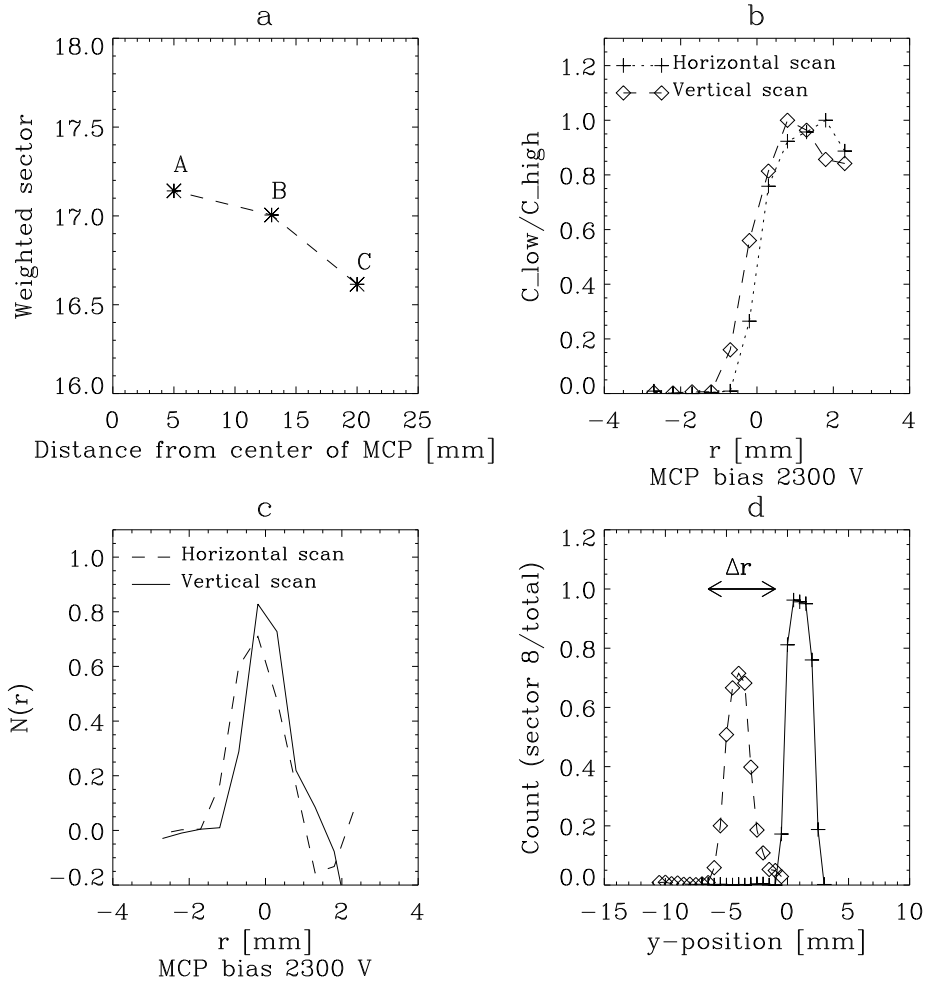


Figure 2.13: (a) shows the sector average from normalized count rates for three points on the MCP. The plot suggests that the sector drift is increased when close to the center of the MCP plate, a result which could be explained by more sector anodes covered by a large area charge cloud from the MCP output. The S-curves in (b) show the fraction of total count rate present in sectors 7 and 8 (+) and 16 and 17 ($\diamond$) as the ion beam is moved vertically (+y direction) over sectors 6, 7, and 8 and horizontal (-x direction) over sectors 15,16, and 17. (c) shows the derivatives of the S-curves and thus the charge distribution in the vertical (full line) and horizontal (dotted line) directions for low (2210 V) MCP bias. Plot (d) shows the instrument response at MCP bias 2210 V (+) and 2600 V ($\diamond$). The difference $\delta y$ between the front edges of the scan (scan direction was +y) is the difference in radius between the two clouds.

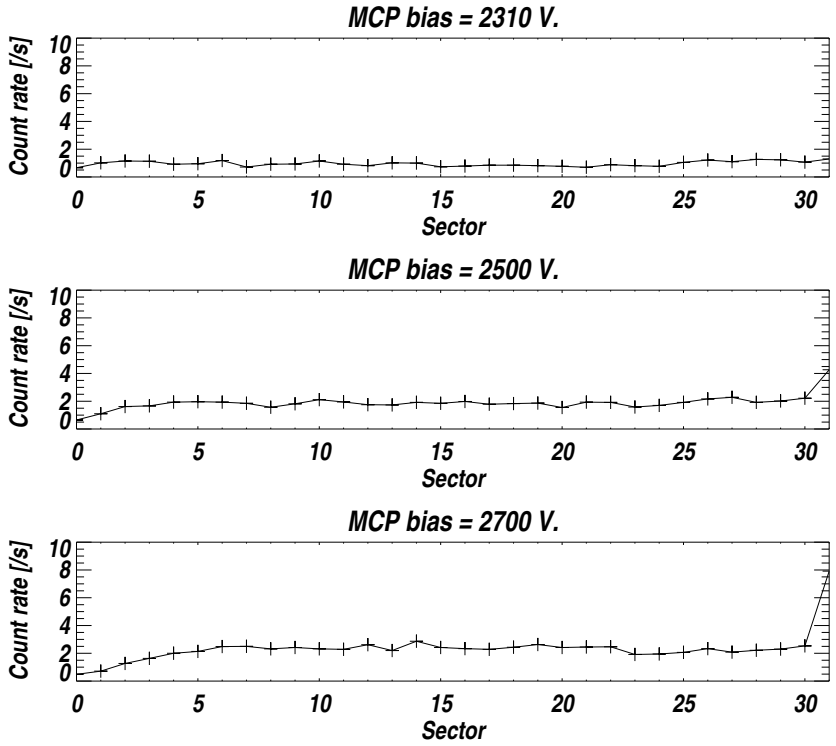


Figure 2.14: Dark count at different MCP biases.

from

$$G = A_{eff}(\theta_0, \varphi_0) \int_{\varphi} \int_{\theta} \frac{C_{meas}(\theta, \varphi)}{C_{meas}(\theta_0, \varphi_0)} \cos\theta d\theta d\varphi, \tag{2.1}$$

where $A_{eff}$ is the effective areal size, $C$ is the measured count rate, $\theta$ is the elevation angle and $\varphi$ is the azimuth angle. $\theta_0 = 0°$ and $\varphi_0 = 0°$ correspond to the sector central axis co-aligned with the beam. The calibration data from sector 14 was used for the geometrical factor calculation. The center sector response was $C(\theta_0, varphi_0) \approx 68$ counts $s^{-1}$. The effective target area of one sector in the NPI is $A_{eff}(\theta_0, \varphi_0) = 0.128\ cm^2$ (visible target block area). The angular scan gave the instrument elevation and azimuth response

$$\int_{\varphi} \int_{\theta} \frac{C(\theta,\varphi)}{C_{meas}(\theta_0,\varphi_0)} \cos\theta d\theta d\varphi = 2.15 \times 10^{-2}$$

and insertion into equation 2.1 results in a geometrical factor of:

$$G_{sector} \approx 0.128 \times 2.15 \times 10^{-2} = 2.7 \cdot 10^{-3} \text{ cm}^2 \text{ sr}$$

Simulation results of the NPI sector geometry based on a Monte-Carlo method gave

$$G_{sim} = 1.70 \times 10^{-3} \text{ cm}^2 \text{ sr},$$

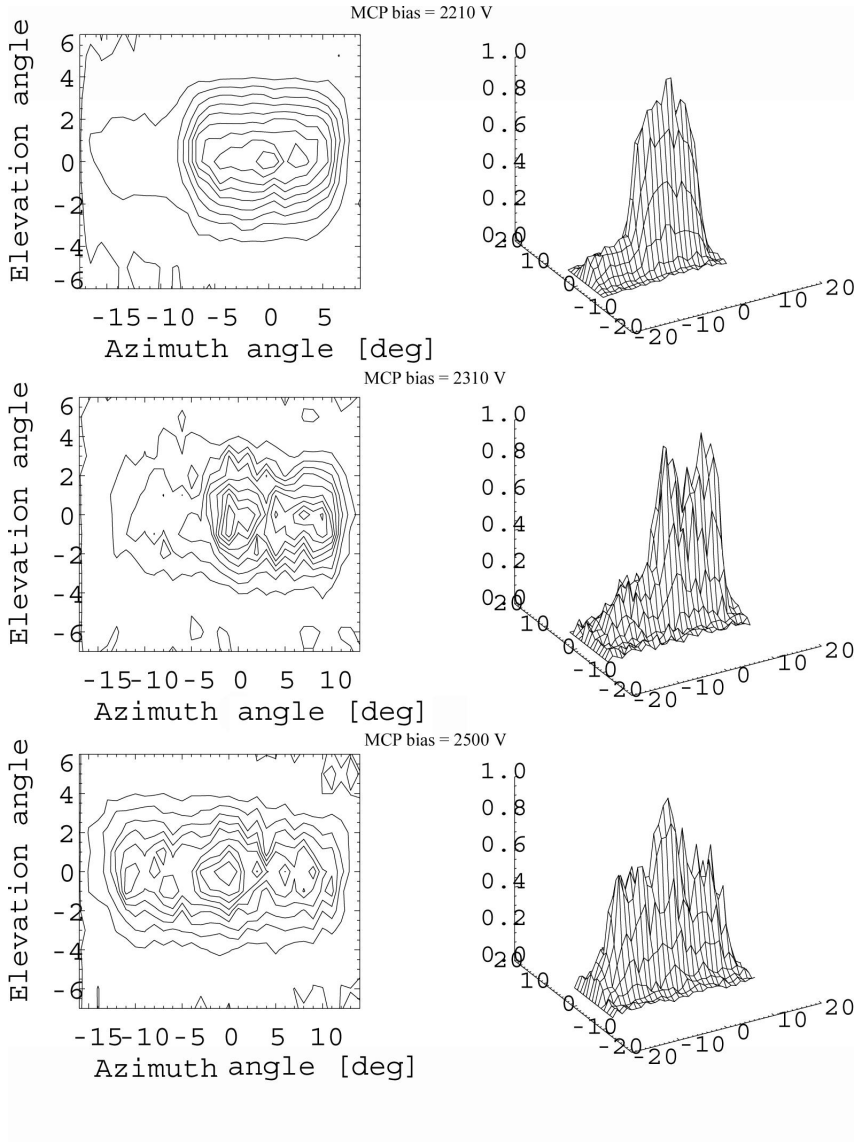


Figure 2.15: Angular scan of sector 14 at MCP bias 2210 V (top), 2310 V (middle), and 2500 V (bottom). The sector priority effect is visible as a decrease in angular resolution with MCP bias. In the bottom panel the response also covers two complete sectors because particles going into sector 13 are registered in sector 14 instead.

Table 2.3: Response of all sectors relative to the response of sector 8.

| Sector | 0 | 1 | 2 | 3 | 4 | 5 | 6 | 7 | 8 | 9 | 10 |
|---|---|---|---|---|---|---|---|---|---|---|---|
| Relative sensitivity | 1.11 | 1.07 | 1.08 | 1.07 | 1.00 | 0.99 | 1.10 | 1.04 | 1.00 | 1.31 | 1.30 |
| Sector | 11 | 12 | 13 | 14 | 15 | 16 | 17 | 18 | 19 | 20 | 21 |
| Relative sensitivity | 1.16 | 1.05 | 0.85 | 0.88 | 0.00 | 0.00 | 0.65 | 0.69 | 0.58 | 0.64 | 0.64 |
| Sector | 22 | 23 | 24 | 25 | 26 | 27 | 28 | 29 | 30 | 31 | |
| Relative sensitivity | 0.84 | 0.97 | 0.99 | 0.98 | 1.15 | 1.28 | 1.30 | 1.44 | 1.09 | 0.86 | |

which is 37 % lower than the measured value. One reason for this may be that the simulations were made befoe the NPI design was finalized and there are therefore slight differences in geometry between the simulated NPI model and the manufactured NPI (T. Sergienko, private communication).

### 2.4.4 Relative response and efficiency

To determine the relative response of other sectors an azimuth scan through the center of all apertures was conducted with large diameter parallel beams of the species and energies listed in Table 2.2. Beam monitoring in the system is provided by the Faraday cup which cannot be performed continuously during calibration measurements. Before the start of the scan the beam stability was verified. The scan was then interrupted at regular intervals (every 72°) to verify beam stability. Fig. 2.16 shows an azimuth scan at the nominal operational bias ($V_{MCP} = 2310$ V) using the species and energy listed in Table 2.2. In each point the average count rate over 8 seconds was measured. For each sector the four central data points were averaged and normalized to that of sector 8 to estimate the relative response of the NPI. The result is listed in Table 2.3. In all further considerations it is assumed that the angular response function is identical for all sectors and only the relative efficiency varies.

The efficiency of the NPI was measured at different MCP biases using stable $H_2O^+$ beams of energies 0.29, 0.48, 0.96, and 4.8 keV. Sector 14 was used. The efficiency $\varepsilon$ is calculated from

$$\varepsilon = \frac{C \cdot A_{beam}}{I \cdot A_{tb}}, \tag{2.2}$$

where $C$ is the measured count rate, $I$ is the beam current, $A_{beam}$ is the beam cross sectional area, and $A_{tb}$ is the effective target block area of one sector. $A_{tb}$ is 0.128 $cm^2$ and $A_{beam}$ is limited to $5.05^2 \times \pi = 80.1$ mm$^2$ using a 10.1 mm slit (see Fig. 2.9). The beam current is

$$I = \frac{I_{faraday}}{e}$$

where $I_{faraday}$ is the Faraday cup reading and $e$ is the elementary charge. The calibration beam could not be monitored continuously as the response was recorded. Instead, the beam intensity

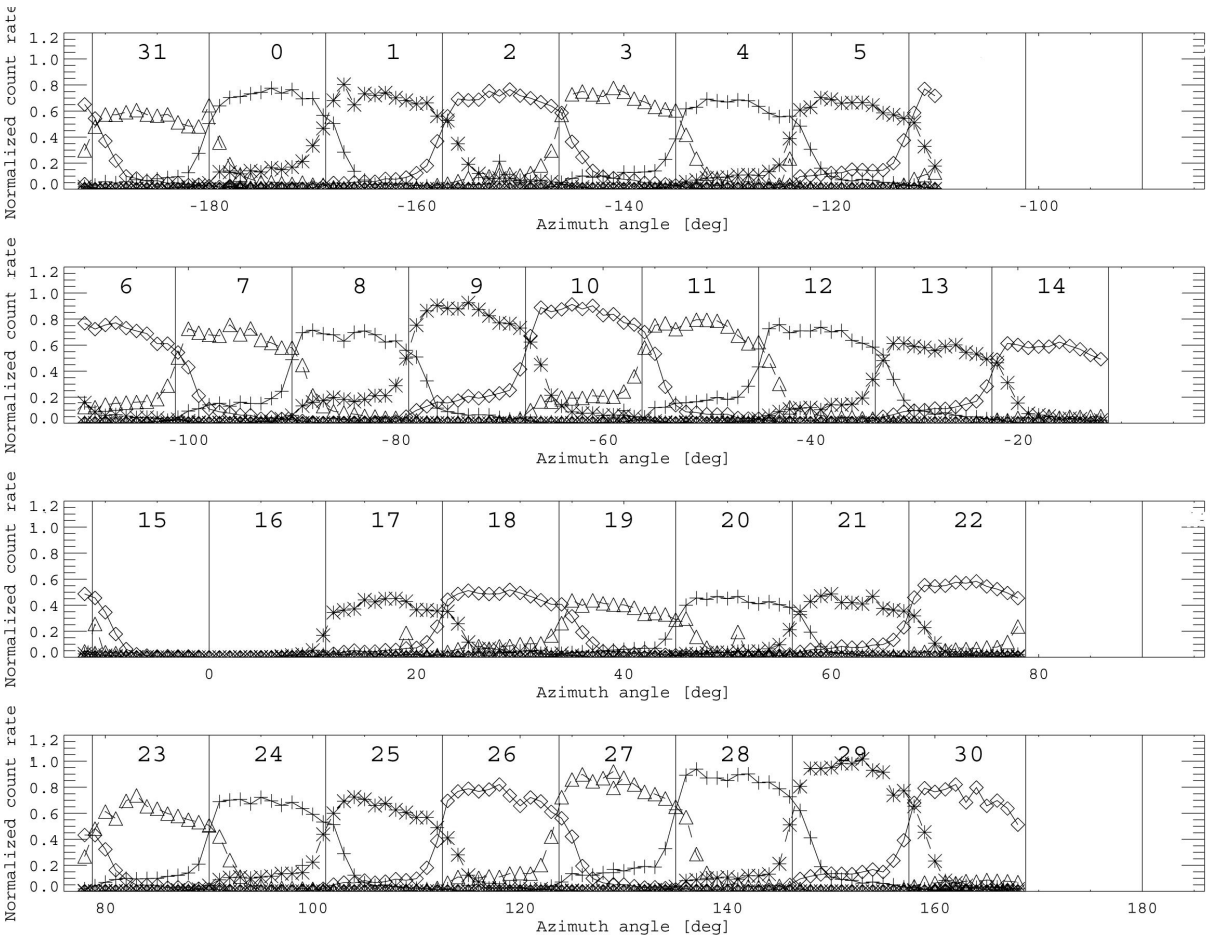


Figure 2.16: Normalized response of the MEX NPI sectors when the calibration beam was in the center aperture plane and the NPI was rotated 360°. Sectors 17 - 22 have a slightly lower relative response than the others.

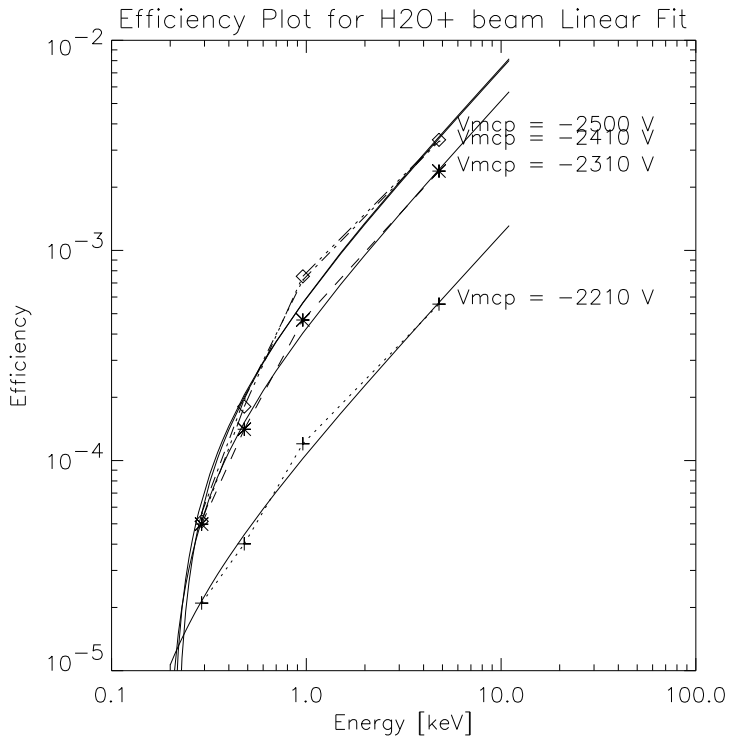


Figure 2.17: The efficiency of the NPI to $H_2O^+$ ions as a function of energy at different MCP bias.

was recorded every 10 s during one minute before the measurement. During this time the average dark count in the NPI sector 14 was also measured. The Faraday cup was then retracted from the beam and the average count rate during one minute was measured. Then the Faraday cup was placed in the beam and the intensity was again recorded every 10 s during one minute. The average beam intensity before and after the instrument response measurement was then used as $I$. The average count rate $C$ during one minute was reduced by the average dark count during one minute. Fig. 2.17 shows a plot of the measured efficiency at different MCP biases with fitted linear approximations of the form

$$\varepsilon = kE + m, \tag{2.3}$$

where $E$ is the ion beam energy in keV. The linear coefficients for the fits are shown in Table 2.4.

The G-factor is used together with efficiency and dark count to convert the count rate of the NPI into ENA flux. The NPI sector count rate, $C_{sector}$, is converted to flux $J$ in

$$J = \frac{C_{sector} - D_{sector}}{G_{sector} \cdot \varepsilon_{sector}} \tag{2.4}$$

where $D_{sector}$ is the sector dark count rate, $G_{sector}$ is the pure geometrical factor of one NPI sector, and $\varepsilon_{sector}$ is the NPI sector efficiency.

Table 2.4: Linear coefficients for efficiency

| $V_{MCP}$ [V] | $k$ | $m$ |
|---|---|---|
| -2210 | $1.205 \cdot 10^{-4}$ | $-1.346 \cdot 10^{-5}$ |
| -2310 | $5.261 \cdot 10^{-4}$ | $-1.008 \cdot 10^{-4}$ |
| -2410 | $7.423 \cdot 10^{-4}$ | $-1.509 \cdot 10^{-4}$ |
| -2500 | $7.567 \cdot 10^{-4}$ | $-1.625 \cdot 10^{-4}$ |

## 2.5 ASPERA-3/NPI initial results

Three main results from NPI observations during the first year in orbit around Mars are presented here. The scanner was not operational during the measurements reported. Section 2.5.1 reports observations of ENAs from charge exchange of the shocked solar wind with the exosphere in the magnetosheath, the region between the bow shock and the induced magnetosphere boundary (IMB). Section 2.5.2 shows measurements of ENAs that are produced in the interaction of the solar wind with the extended exosphere then penetrate the Martian system and are observed in the Martian eclipse. The final example, in Section 2.5.3, deals with possible observations of interplanetary ENAs.

### 2.5.1 ENAs from the magnetosheath

NPI observations are here compared to simulations of ENAs based on a empirical model of the plasma flow around Mars [*Kallio*, 1996]. This model has been used to study the role of charge exchange in Mars-solar wind interaction [*Kallio et al.*, 1997], and was used by *Holmström et al.* [2002] to simulate ENA images. The computational technique used to calculate the ENA flux was described in detail by *Holmström et al.* [2002]. For solar wind parameter estimates measurements from the Ion Mass Analyzer (IMA) and the Electron Spectrometer (ELS) have been used. First, the observations are described. They are then compared with numerical simulations of ENA and UV photon flux and the results are finally discussed.

The NPI observations reported here were made during Mars Express orbit 363 on May 3, 2004, when the spacecraft passed through the magnetosheath and into the solar wind. Fig. 2.18 shows Mars Express orbit 363 in cylindrical coordinates, in which the x-axis points towards the sun and the vertical axis is the distance to the Mars-sun line. The bow shock and IMB positions are shown as dashed lines. The modeled bow shock and IMB shapes shown in Fig. 2.18 are the same as those used for ENA calculations in the simulations discussed below. Fig. 2.19 shows the position of Mars Express and the field of view of sectors 21-25 at 20:12:44 UT on May 3, 2004, when the spacecraft was in the magnetosheath. The grey-scale map shows a simulation of the ENA production rate in the center of the sector plane in the NPI. The simulation is discussed further below. In the plot $\xi$-axis is the projection of the Mars-Sun line in the NPI plane, and the $\zeta$-axis is perpendicular to both the $\xi$-axis and the Mars-sun line. Fig. 2.20 shows the observed count rates of NPI sectors 21-25 as the spacecraft moves through the Martian magnetosheath. The peak in sectors 22-24 between 20:11 UT and 20:17 UT is identified as ENAs from the main production region in the magnetosheath (it

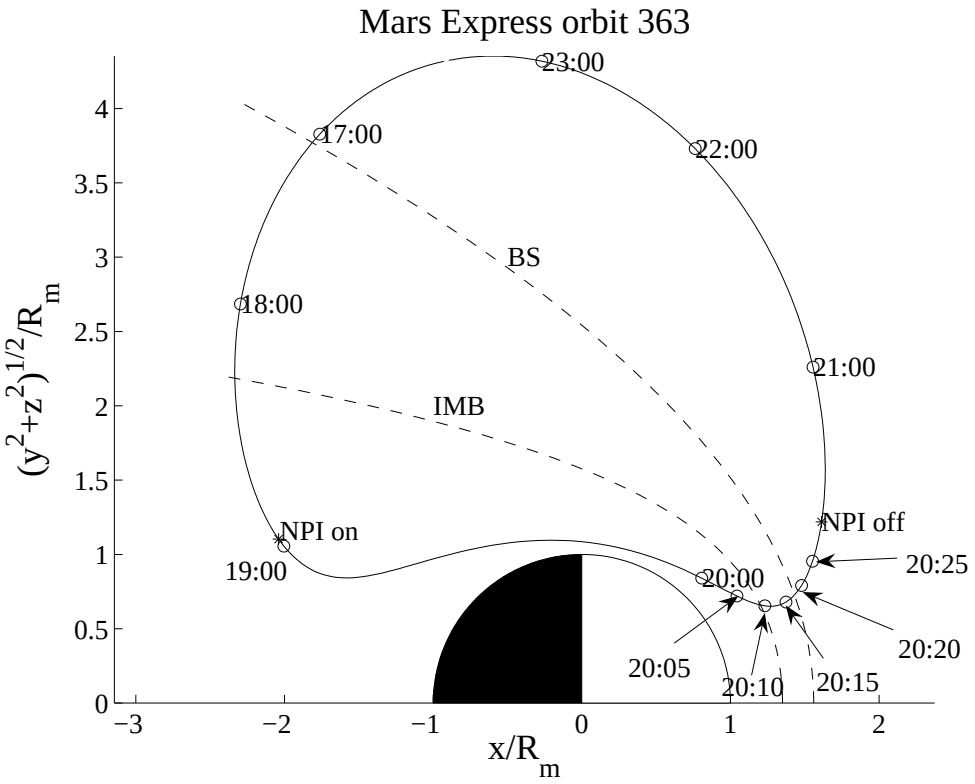


Figure 2.18: Mars Express orbit 363 in cylindrical coordinates, with the bow shock (BS) and the induced magnetosphere boundary (IMB) shown. The bow shock and IMB shapes shown here are the same as those used for ENA calculations with the empirical model discussed in the text. The origin of the coordinate system is in the center of Mars. The $x$-axis is directed toward the sun, the $z$-axis is directed northward, perpendicular to the ecliptic plane, and the $y$-axis closes the right-handed system. $(y^2 + z^2)^{1/2}$ is the distance to the Mars-sun line. From *Gunell et al.* [2005a].

also appear in sectors 21 and 25, but is less pronounced there). The geometry is shown in Fig. 2.19, which shows the spacecraft position at 20:12:44 and the field of view of the relevant sectors. Sectors 24 and 25 also have another peak at about 19:50 UT followed by a slow decay until the count rate rise again in the main peak at 20:11 UT when the spacecraft has entered the magnetosheath. The other three sectors in Fig. 2.20 also show a small elevation of the count rate during this period. From 19:50 to 20:10 the spacecraft has not yet entered the magnetosheath and is still inside the IMB. The field of view of the sectors in question lie between Mars and the IMB and the source of this signal could be backscattered ENAs or contamination of UV photons from the reflected on the Martian surface or scattered in the atmosphere.

Simulations of ENA and UV were compared to the observed signal. The ENA simulations were

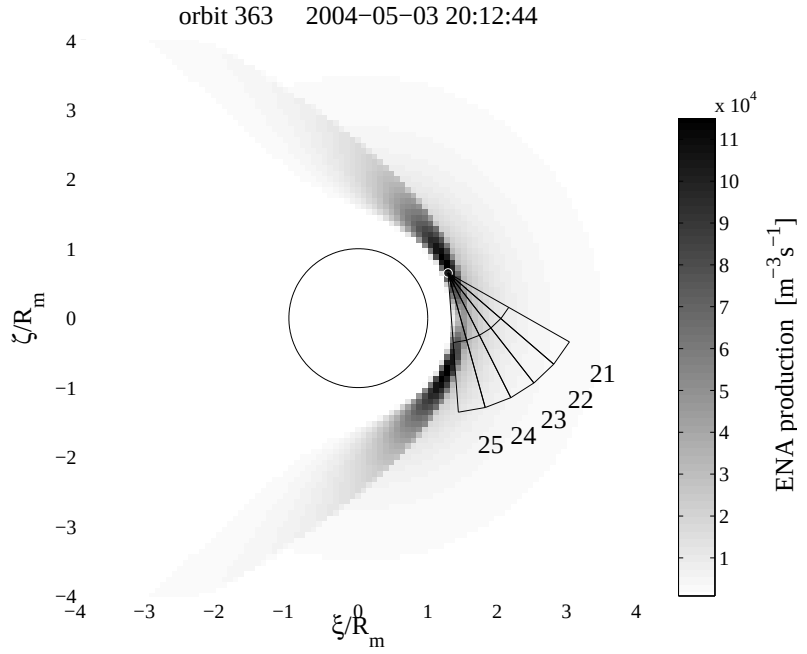


Figure 2.19: Spacecraft position and field of view of sectors 21-25 at 20:12:44 UT on May 3, 2004. The grey-scale map shows a simulation of the ENA production rate in a plane that intersects the center of all NPI sectors. The $\xi$-axis is the projection of the Mars-sun line in the NPI plane, and the $\zeta$-axis is perpendicular to both the $\xi$-axis and the Mars-sun line. From *Gunell et al.* [2005a].

based on the empirical model for the plasma flow around Mars developed by *Kallio* [1996] (see Fig. 2.1). The parameter values used in the analysis are shown in Table 2.5, which also shows the parameters used by *Holmström et al.* [2002], by way of comparison. The simulated ENA count rates shown in Fig. 2.21 have been computed by a weighted average of 434 line of sight integrals for each sector. The weights are given by the response function of the NPI for ENAs incident from different directions in Fig. 2.15. The exosphere model included three species: atomic hydrogen, molecular hydrogen, and oxygen. For oxygen two different temperature populations were modeled. The model geometric and exospheric parameters were varied from the ones used by *Holmström et al.* [2002] to fit the observed data. The solar wind parameters were estimated from IMA and ELS data and were fixed. For example, an IMB position (defined as the planetocentric distance to the subsolar IMB) of 1.35 $R_m$ agrees much better with the rising edge of the main peak in the count rate for sector 23, increased neutral densities boost the ENA generation, and a modified IMB penetration depth increases the proton stream lines in the magnetosheath, also generating more ENAs in the observed area. The modeling result is shown as the dashed line in Fig. 2.21. The main peak of the ENA flux starts shortly after the spacecraft has entered the magnetosheath at 20:10 UT and ends

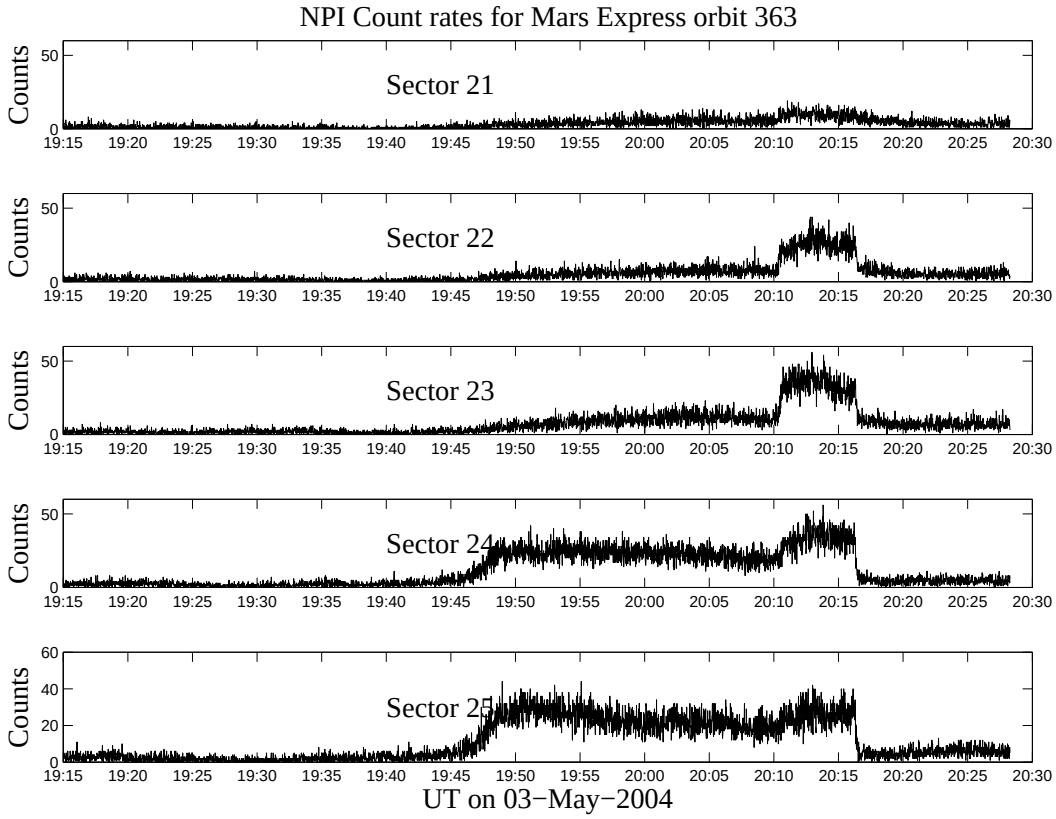


Figure 2.20: Orbit 363 data from the ASPERA-3 NPI sensor. From *Gunell et al.* [2005a].

Table 2.5: Model parameters used by *Holmström et al.* [2002] compared to the parameters used here. The model obstacle is located at 170 km altitude.

| Parameter | Holmström | This work |
|---|---|---|
| **Solar wind** | | |
| Plasma density | $2.5 \cdot 10^6 \mathrm{m}^{-3}$ | $2.0 \cdot 10^6 \mathrm{m}^{-3}$ |
| Temperature | 10 eV | 5 eV |
| Solar wind speed | 400 km/s | 470 km/s |
| **Geometry** | | |
| Bow shock position | $1.55 R_m$ | $1.55 R_m$ |
| IMB position | $1.2 R_m$ | $1.35 R_m$ |
| IMB penetration | 1/6 | 0.05 |
| **Neutral exobase** | | |
| H density | $9.9 \times 10^{11}$ m$^{-3}$ | $2.97 \times 10^{12}$ m$^{-3}$ |
| H temperature | 192 K | 192 K |
| $H_2$ density | $3.8 \cdot 10^{12}$ m$^{-3}$ | $1.14 \times 10^{13}$ m$^{-3}$ |
| $H_2$ temperature | 192 K | 192 K |
| $O_{hot}$ density | $5.5 \cdot 10^9$ m$^{-3}$ | $1.65 \cdot 10^{10}$ m$^{-3}$ |
| $O_{hot}$ temperature | $4.4 \cdot 10^3$ K | $4.4 \cdot 10^3$ K |
| $O_{thermal}$ density | $1.4 \cdot 10^{14}$ m$^{-3}$ | $4.2 \cdot 10^{14}$ m$^{-3}$ |
| $O_{thermal}$ temperature | 173 K | 173 K |

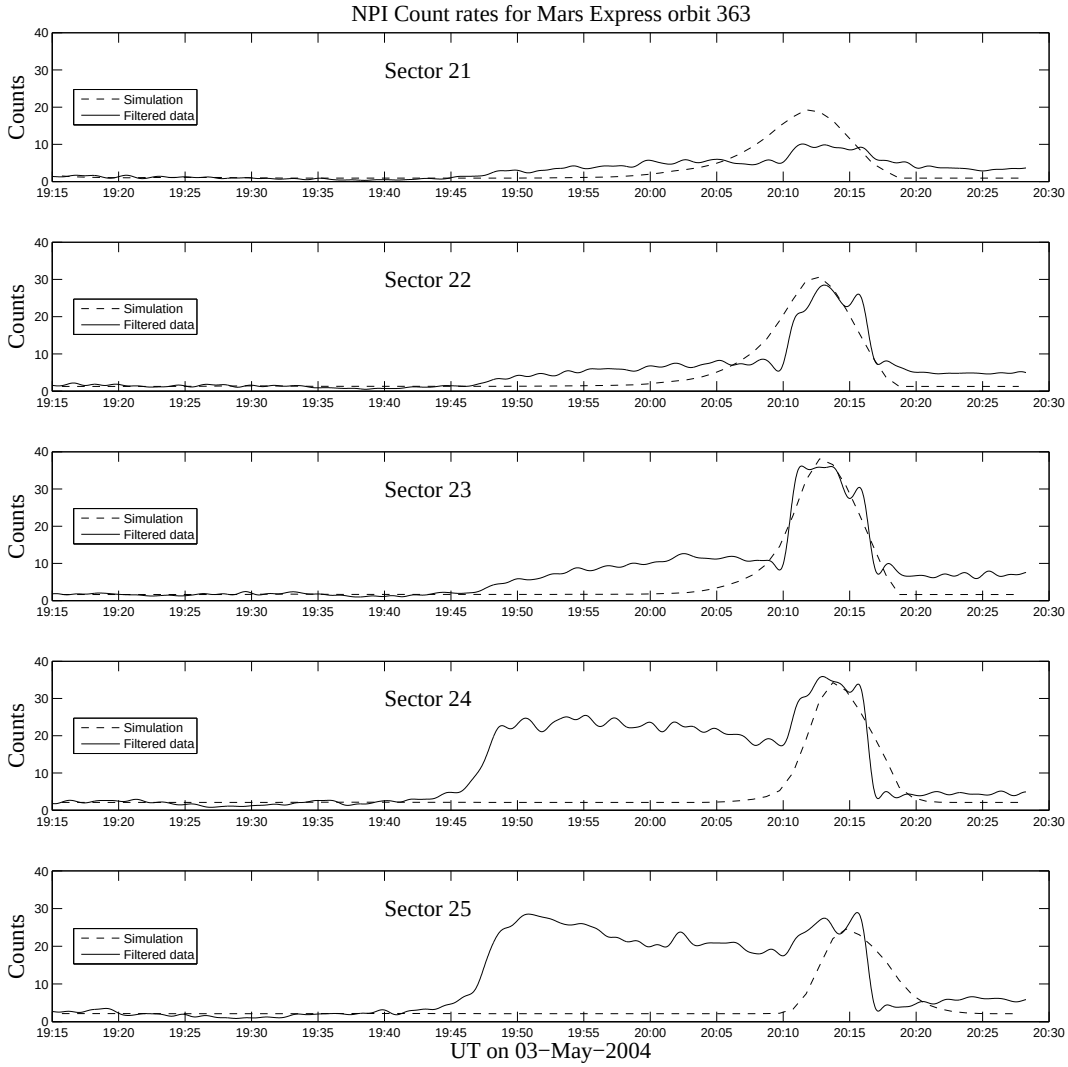


Figure 2.21: Simulations (dashed curves) and filtered data (solid curves) from MEX orbit 363 and the ASPERA-3 NPI sensor. The highest count rates in sector 23 and 24 correspond to fluxes of $1.3 \times 10^{11}$ m$^{-2}$ sr$^{-1}$ s$^{-1}$ and $1.2 \times 10^{11}$ m$^{-2}$ sr$^{-1}$ s$^{-1}$ respectively. The dark counts shown in Table 2.6 have been added to the simulation results. From *Gunell et al.* [2005a].

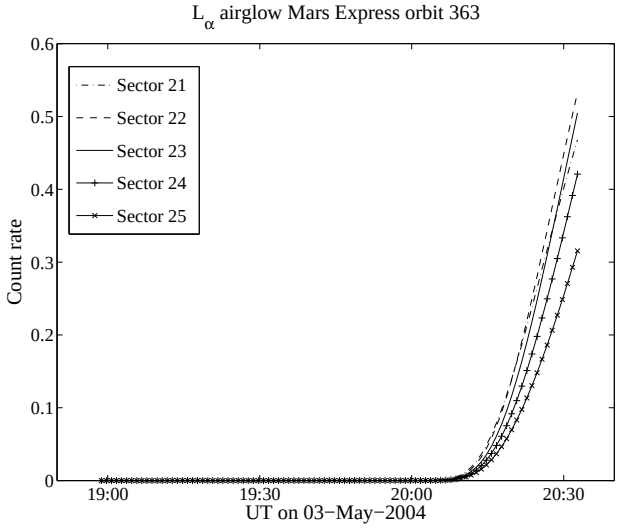


Figure 2.22: A simulation of the count rate caused by Lyman alpha airglow from the Martian hydrogen corona. From *Gunell et al.* [2005a].

a minute before the spacecraft crosses the bow shock and enters the solar wind at 20:18 UT. The solid line of Fig. 2.21 is the raw data, which has been digitally filtered to remove high frequency count rate changes. The filter is a low-pass finite impulse response filter of length 201, with real and symmetric coefficients. The signal is run first forward and then backward through the filter, thus obtaining exactly zero phase distortion. Signals with a period less than one minute are efficiently attenuated.

To investigate the influence of UV photon contamination on the observation count rates a simple model of the Lyman-$\alpha$ airglow was used. The model is a simplified version, assuming only single scattering of the incident sunlight, based on *Bush and Chakrabarti* [1995] . The value for the solar Lyman-$\alpha$ used in the model is obtained from the Solar2000 model [*Tobiska et al.*, 2000]. The Mars Express NPI was not calibrated against UV photons and the NPI photon detection efficiency and relative directional sensitivities to Lyman-$\alpha$ photons were obtained in calibrations of the NPI reference model, which is the same as the Venus Express flight model. A description of the Venus Express NPI photon calibrations and results can be found in Section 3.7. The calibration is not on the same physical sensor, which introduces an uncertainty of the absolute count rate due to photons is introduced, but the simulation result can still serve as a relative measure of the contribution from ultraviolet light. The shape of the curves shown in Fig. 2.22 can thus be compared to the shape of the curves showing observed count rate in Fig. 2.20. The simulated count rates generated from Lyman-$\alpha$ photons are below 1 count per second throughout the observation period. This is 10-100 times less than what is observed and the shape of the curve differs significantly from the observed data. Even if the UV photon detection efficiency is orders of magnitude higher than the calibrated

Table 2.6: ENA flux observed by the ASPERA-3 NPI and the dark count and sensitivity that was used to calculate the flux.

| Sector | Flux ($cm^{-2}sr^{-1}s^{-1}$) | Dark count | Sensitivity ($cm^{-2}sr^{-1}$) |
|---|---|---|---|
| 21 | $3.4 \times 10^6$ | 0.9 | $5.2 \times 10^{-6}$ |
| 22 | $1.0 \times 10^7$ | 1.3 | $6.8 \times 10^{-6}$ |
| 23 | $1.3 \times 10^7$ | 1.6 | $7.9 \times 10^{-6}$ |
| 24 | $1.2 \times 10^7$ | 2.1 | $8.0 \times 10^{-6}$ |
| 25 | $9.9 \times 10^6$ | 2.1 | $7.9 \times 10^{-6}$ |

values used, the observed count rate cannot be caused by this UV source.

Considering the filtered data of Fig. 2.21 The maximum flux can be calculated for each sector during the main peak between 20:11 UT and 20:17 UT. The flux is computed using equation 2.4. The result is shown in Table 2.6. Since the NPI cannot resolve the energy of the particles measured the efficiency corresponding to 1 keV was used. To get the efficiency for each sector the relative response of each sector was determined from the calibration azimuth scan (Fig. 2.16). The dark count is estimated as the mean of the count rate between the times 19:15 and 19:45. The sensitivity for each sector is calculated as $G\varepsilon$. The maximum ENA flux value in sector 23 is $1.3 \times 10^7$ $cm^{-2}sr^{-1}s^{-1}$ which is in agreement with the highest emission from the shocked solar wind predicted by *Holmström et al.* [2002], as shown in Fig. 2.2. The uncertainties that can produce an error in the calculation of the flux comes from the calibration of the efficiency. The calibrated efficiencies are for $H_2O^+$ and not hydrogen ENAs. During the calibration of the Venus Express NPI it was found that the efficiency is comparable for protons and $H_2O^+$ ions (see Section 3.3) The angular response on one sector varies depending on the angle of incidence of the particle (Fig. 2.15). In the calculation the angle of incidence of all particles is assumed to be more or less in the center of the sector and the peak response of the sector was used. The energy of the measured ENAs is not known. Since efficiency is a function of energy, the observed count rate increase from $\sim 10$ $s^{-1}$ to $\sim 35$ $s^{-1}$ in the main peak could be an effect of an energy increase of the particles as well as of an increased intensity. The error of using the efficiency for 1 keV particles in the calculations is $7.4 \times 10^{-4}$/eV (the slope of the fitted 2310 V line in Fig. 2.17). For a constant intensity the required energy increase to raise the count rate in the NPI by 15 $s^{-1}$ is around 20 keV provided the efficiency is linear over such energy ranges. That is an unresonably large increase in energy.

A peak in the count rates of sectors with a field of view between the Martian bow shock and the IMB has been observed. Models of ENA and UV photon generation concludes that the source of the observed peak in the flux is ENAs created in charge exchange collisions between solar wind protons and atoms in the atmosphere of Mars. The geometric and exospheric model parameters have been modified to better fit the data, while the solar wind parameters were estimated from measurements of the IMA and ELS sensors and kept constant.

### 2.5.2 Solar wind ENAs on the night-side of Mars

Another source of ENAs near Mars discussed in Section 2.1 is the charge exchange between the solar wind ions with the extended Mars exosphere. NPI observations show how significant flux of ENAs produced upstream of the bow shock can penetrate the Martian system and be measured on the night side of the planet. Similar to the previous section the observations are first described, then compared to simulations of ENA and UV photons. To further study the influence of UV photons the NPI observations were also compared to simultaneous measurements of photoelectrons by the electron spectrometer ELS.

In the considered orbits the NPI aperture plane coincides with the ecliptic plane and the scanner was not operating. For this attitude the solar photon flux impinges directly on the NPI field of view resulting in extremely high count rates ($10^5$ s$^{-1}$), rendering any neutral solar wind measurements impossible (the sensor is effectively "blinded"). However, as the spacecraft entered the Martian eclipse between April and May 2004 during an eclipse season, the observations showed a lingering response from the sun direction. The observations presented here were made during the transition of the spacecraft into Mars eclipse. A typical view of the orbit geometry with the field of view of NPI sectors 20-22 is shown in Fig. 2.23. The plot is a cylindrical representation of a Mars centered right-hand coordinate system, as in Fig. 2.18. The measured count rates for sectors 17-28 during the entry into eclipse on orbit 343, April 27, 2004 are shown in Fig. 2.24a. The entry into the Mars penumbra, when the disc of the sun intersects the Martian limb, occurred at 11:18:27 UT and the spacecraft entered the Mars umbra, when the sun is completely below the Mars limb, at 11:19:03 UT. As seen in the plot a signal remains in the NPI during several minutes after the entry into eclipse. The dashed lines in the plot are the limbs of Mars. Another representation of the data at 11:22 UT that helps to understand the geometry better is in Fig. 2.25. The observation starts with a sharp drop in the count rate. This is common for all eclipse transitions and can be explained by the direct solar photon flux disappearing when the sun sets below the limb of Mars. When the count rate has dropped to around $10^2$ s$^{-1}$/sector there is an abrupt change in the slope and the count rate exhibits a logarithmic decrease that lasts for typically 5-8 minutes. The count rate then reaches the background level of the NPI in eclipse at a few counts per second. Fig. 2.26 shows some typical NPI count rates during other orbits as the spacecraft enters eclipse between April 23, 2004 and May 14, 2004. The count rate is plotted against the parameter $h$, which is defined in Fig. 2.27. The signals are smoothed using a running mean:

$$S_i = \begin{cases} \frac{1}{w}\sum_{j=0}^{w-1} C_{i+j-w/2}, & i = (w+1)/2, \ldots, N-w; \\ C_i, & otherwise; \end{cases}$$

where $S_i$ is the new, smooth, data point, $w$ is the width of the smoothing box, $C_i$ is the original data point, and N is the total number of data points. A width of $w = 59$ s was used here. The signal demonstrates a clear variability. Some orbits show a response lasting longer and there can be a flat region in the count rate after the initial decrease (for example orbits 343 and 362 in Fig. 2.26). Other orbits exhibit a more direct decrease in count rate (for example orbits 344 and 363).

Since we attribute the observed signal to the angular scattering of the neutral solar wind due to thermal spreading of the proton velocity and, possibly, interaction with the atmosphere in the

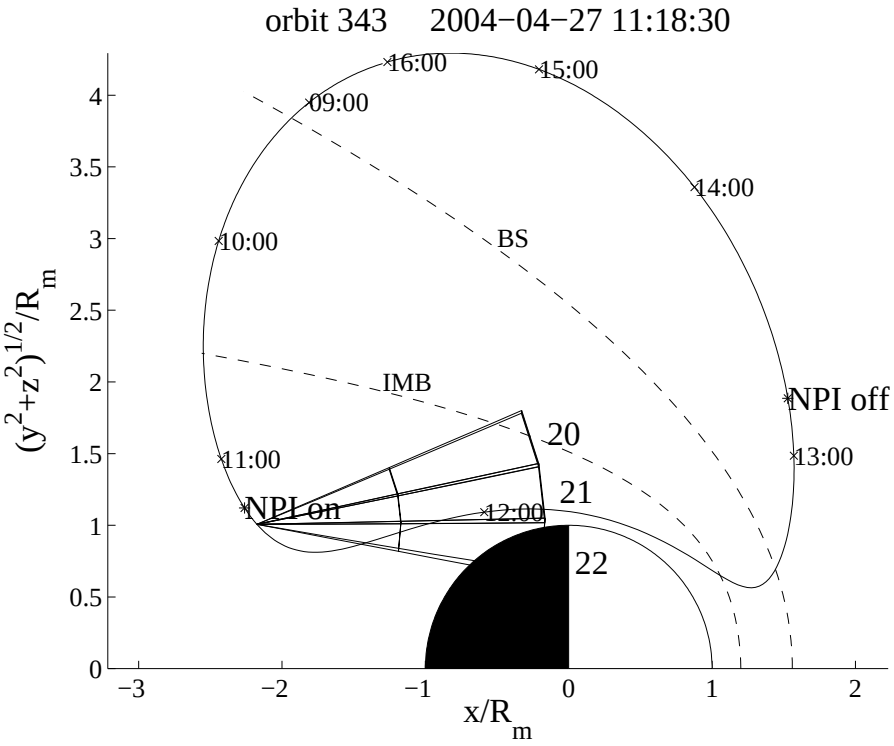


Figure 2.23: A view of the orbit geometry with the field of view of NPI sectors 20-22 at 11:18:30 UT during orbit 343 on April 27, 2004. The plot is in cylindrical coordinates. UT hours are included in the plot. Distances are in Mars' radii ($R_m = 3397$ km). The area between the bow shock (BS) and the induced magnetosphere boundary (IMB) is referred to as the magnetosheath. From *Brinkfeldt et al.* [2005].

terminator region as simulated by *Kallio et al.* [2005]. Therefore we ran simulations based on the empirical model with different solar wind ion temperatures (20, 30, and 50 eV). The parameters used in the simulations are identical to the first column of Table 2.5 also used by *Holmström et al.* [2002]. Fig. 2.24b and 2.24c show simulated count rates with different solar wind temperatures and densities. Since the Martian atmosphere can scatter Lyman-$\alpha$ photons into the eclipse, the simplified UV model described in Section 2.5.1 was also used here to study how much of the observed count rate could be attributed to contamination from Lyman-$\alpha$ photons. The simple UV model only takes into account the Lyman-$\alpha$ airglow and not direct photons from the sun. Fig. 2.28 is a plot of the ENA and UV simulations overlaid on the count rate from sectors 20, 21 and 22. The photon related count rate is negligible in all other sectors during this time interval. Sectors 20 and 21 follow the ENA simulation reasonably well, while sector 22 has a count rate that is too high. This could partly be due to ENA scattering in the exosphere [*Kallio et al.*, 2005], Not only is the expected UV photon

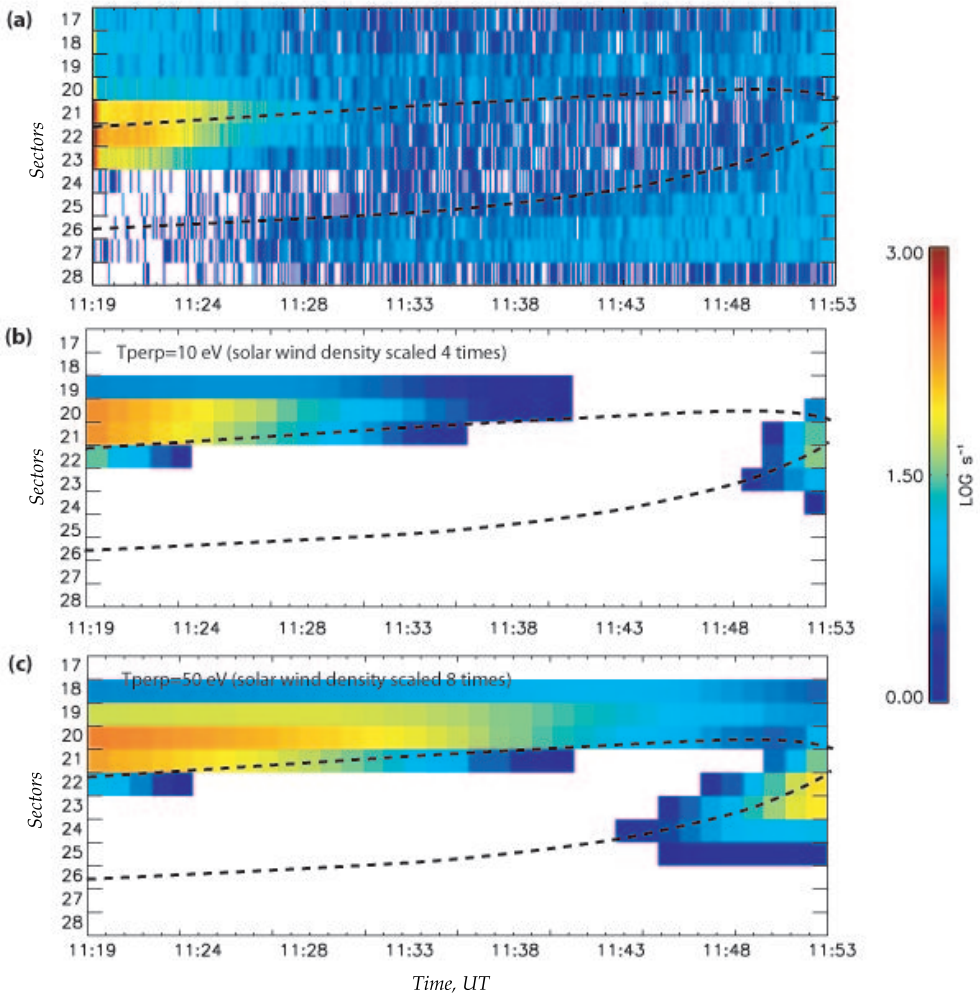


Figure 2.24: (a) NPI measurements obtained in eclipse on 27 April 2004 (orbit 343). A distinct signal was observed in sectors 20-23 lasting deep into the umbra. The y-axis is sector number (direction) and x-axis is time in UT. The color scale indicates count rate ($s^{-1}$). The dashed lines are the plotted Martian limbs as viewed from the NPI. (b) Simulations using a semiempirical solar wind flow model with a temperature of 10 eV. (c) Simulations using a semiempirical solar wind flow model with a temperature of 50 eV. The ENAs are produced via charge exchange of the upstream solar wind with the extended Martian exosphere and can propagate into the umbra due to the temperature spread. From *Brinkfeldt et al.* [2005].

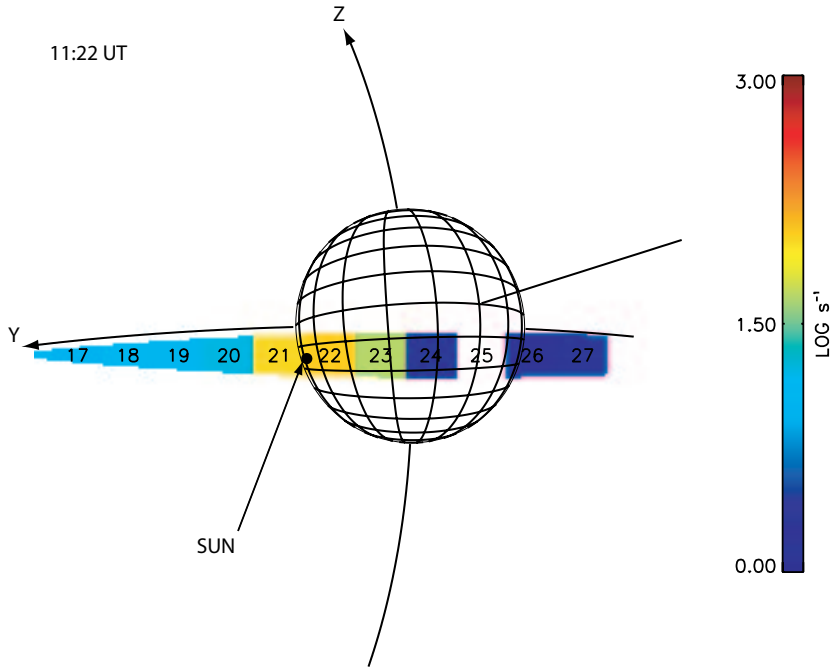


Figure 2.25: A fish-eye view of the observed ENA emissions at around 11:22 UT. The image resembles what a human eye would see. Ecliptic north is along the z-axis and the x-axis points towards the sun. The dot represents the location of the sun and is hidden behind the planet. The color scale indicates count rate ($s^{-1}$). From *Brinkfeldt et al.* [2005].

count rate (right hand y-axis in Fig. 2.28) orders of magnitude too low to explain the signal, the curve shape is different. The slope of the UV count rate is consistently higher than the slope of the data count rate for all three sectors. Note that the direct solar photons are not modeled, which is why we do not see a high UV count rate when we are outside of the eclipse in the beginning of the figure. According to the ENA simulations with different solar wind temperature a signal that is lower in intensity as the NPI enters eclipse, but lasts longer into the eclipse is expected for higher solar wind temperatures.

To further investigate wether or not the signal is related to UV we have compared the NPI observations with photoelectron measurements from the ASPERA-3 electron spectrometer ELS. Since the flux of photoelectrons emitted by the spacecraft is proportional to the incident UV photon flux, the ELS measurements can serve as an indicator of the photon flux variations. We have examined

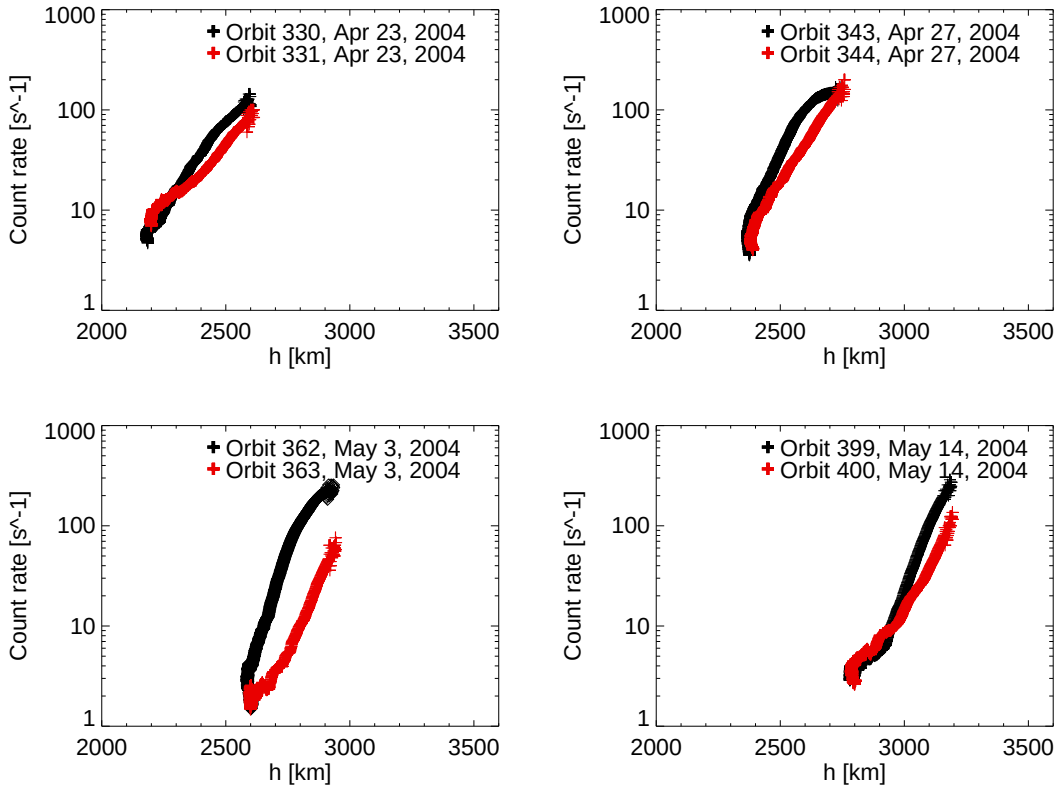


Figure 2.26: Count rate data from NPI sector 22 during selected orbits between April 27 and May 14, 2004 as a function of the target parameter $h$ for the sector 22 viewing direction (see Fig. 2.27). From *Brinkfeldt et al.* [2005].

the correlation between the NPI signal and ELS photoelectron measurements. The ELS sector 15 viewing across the spacecraft was chosen to observe photoelectrons emitted from the spacecraft. The ELS electron energy spectrum from sector 15 was integrated from 5 eV (the internal protection grid potential) to 10 eV (estimated spacecraft negative potential) to determine the integral electron flux that is produced locally on the spacecraft. The photoelectron flux is compared to the NPI measured flux in Fig. 2.29 for orbit 343 on April 27, 2004 The lower panel of Fig. 2.29 shows the dependence of the NPI normalized flux on the ELS normalized flux after the initial drop in NPI count rate (i.e. after 11:18:12 UT). Some correlation exists for low flux when the count rate in the NPI decreases close to noise level, but none for higher NPI fluxes.

In conclusion the NPI observed ENAs presumably from upstream of the bow shock that penetrate the Martian system as the spacecraft moves into eclipse. Simulations with ENA and UV models and a lack of correlation with photoelectrons emitted from the spacecraft suggest that the observed signal is not due to UV, but is ENA. The variability shown i Fig. 2.26 is interesting too and cannot

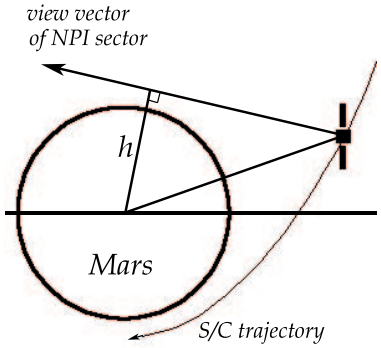


Figure 2.27: A target parameter $h$ is defined as the shortest distance to the NPI center sector view vector from the center of the planet. From *Brinkfeldt et al.* [2005].

be expected if the signal had been related to only the solar photons. As seen, there is a clear variability between consecutive orbits, which is on a time period of 7-8 hours. One can rule out that this variation is due only to changes in the orbit geometry (because the orbit geometry and spacecraft attitude change only marginally between consecutive orbits). Therefore it must be an effect of changing physical conditions around the planet. One possibility is changes in the upper atmosphere conditions, affecting scattering of the solar wind ENAs at the terminator. However, Monte Carlo simulations of such scattering by *Kallio et al.* [2005] predict low ENA fluxes scattered into eclipse. Another possibility is a change in the solar wind ion temperature. More theoretical studies are required to come to a final conclusion.

### 2.5.3 Observations in the deep eclipse of Mars

*Holmström et al.* [2005] have analyzed NPI observations in the deep umbra behind Mars. Since the observed count rates there are close to the NPI dark count, statistics over all observations during the 2004 and 2005 eclipse seasons are presented. Several statistically significant signals are observed in both 2004 and 2005 (Fig. 2.30). In the 2004 eclipse season, the NPI plane was mostly in the ecliptic plane. During the 2005 eclipse season the attitude of the spacecraft changed so that directions away from the ecliptic became visible. The strong emissions at negative ecliptic latitudes in Fig. 2.30b correlate well with the galactic plane. To determine what parts of the signals comes from ENAs and what parts comes from UV, the data were compared to a skymap of UV emissions measured by the SWAN instrument [*Bertaux et al.*, 1995] on the SOHO spacecraft. Some but not all signals can be explained with UV light from sources in the galactic plane. Fig. 2.31 shows a SWAN skymap of the UV emissions that has been smoothed according to the NPI angular resolution and is compared to the NPI observations during the 2005 eclipse season. Further investigations where made by looking at the time evolution of the observations. Fig. 2.32 show how the signals in the ecliptic plane evolve with time. Signals that change longitude at the same rate as the sun seem to be ENAs originating

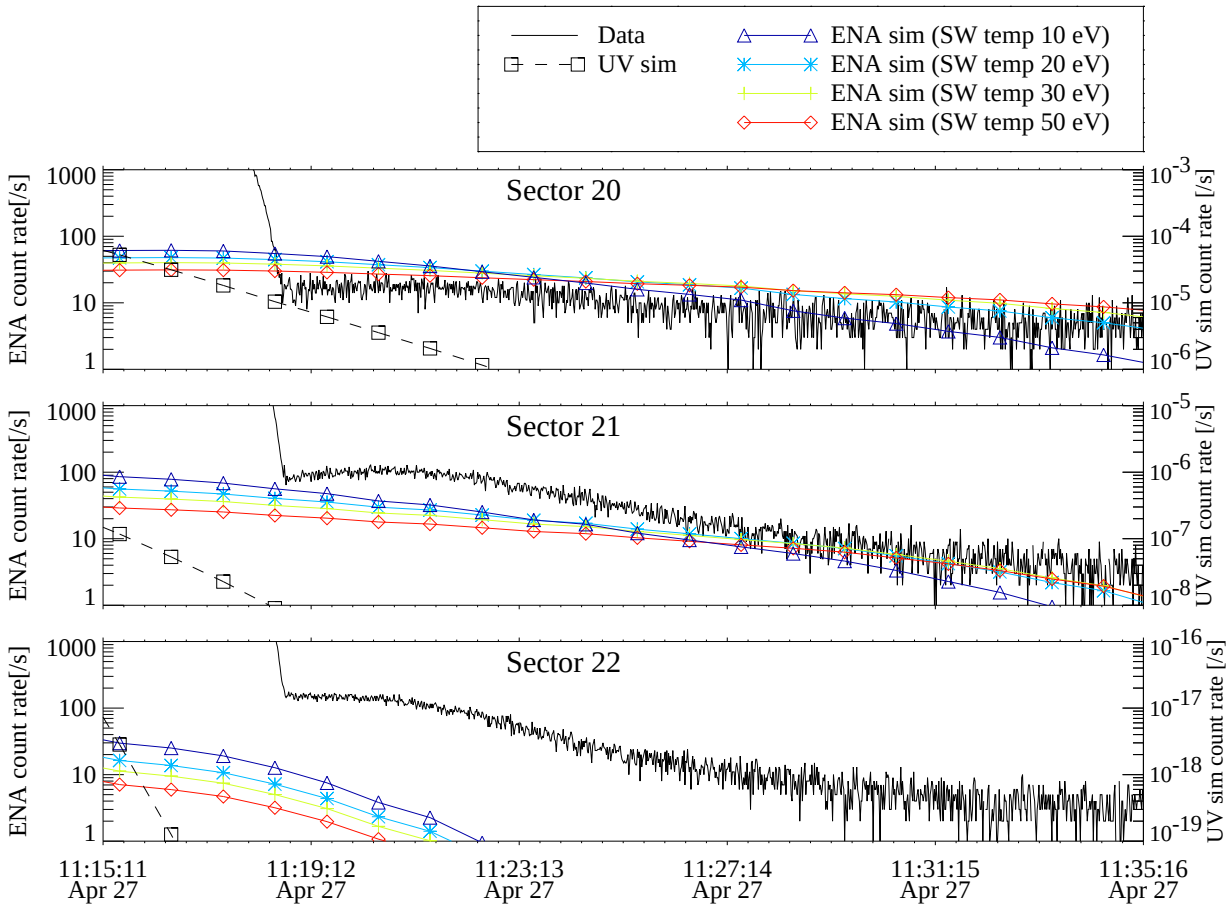


Figure 2.28: NPI count rates from sectors 20, 21, and 22 (solid line) during the transition into eclipse on orbit 343 (April 27, 2004). ENA simulations with a virtual NPI sensor are overplotted. ENA simulations count rate and the observed data count rate in each plot are on the left y-axis. The simulations do not include scattering of ENAs in Mars' exosphere. The dashed line with squares is a UV simulation with a virtual NPI sensor. The simulated UV count rate in each plot is on the right y-axis. The extremely low count rate of UV suggests that the observations are ENAs. From *Brinkfeldt et al.* [2005].

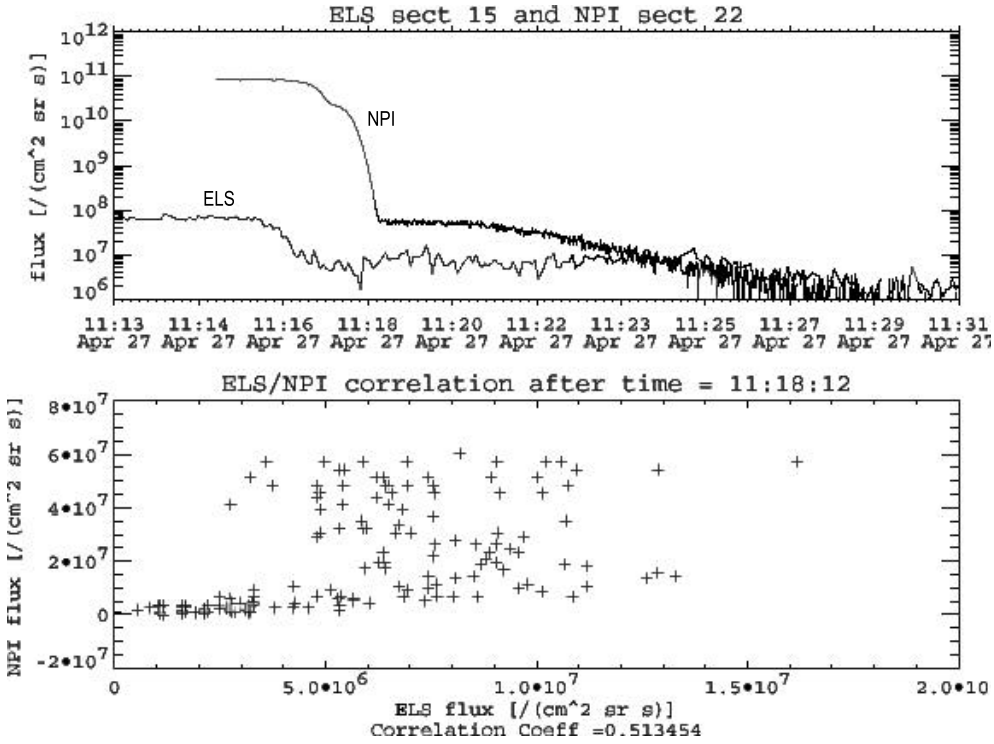


Figure 2.29: The top panel is a comparison of the particle fluxes measured by NPI and ELS, when entering eclipse. The ELS flux is integrated between 5 eV and 10 eV, and is a measure of photoelectron production on the spacecraft surfaces. It can thus give an indication of the UV background. The lower panel shows the dependence of the normalized NPI flux on the normalized ELS flux. No correlation is observed. From *Brinkfeldt et al.* [2005].

from Mars that reach deep into the umbra. Signals that have a constant longitude with time have probably stellar UV sources. But there are signals that have other characteristics and therefore cannot directly be connected to Martian ENAs or UV from stars. There is a source in the ecliptic around longitude 200° in 2004, that seem to have moved 25° to a higher longitude in 2005. If this is the same signal it is inconsistent with a stellar UV source. The next step in the investigation is to try to identify such signals in the NPD sensor on Mars Express or the LENA sensor [*Moore et al.*, 2000] on the IMAGE spacecraft [*Burch*, 2000] in Earth orbit. This work is ongoing.

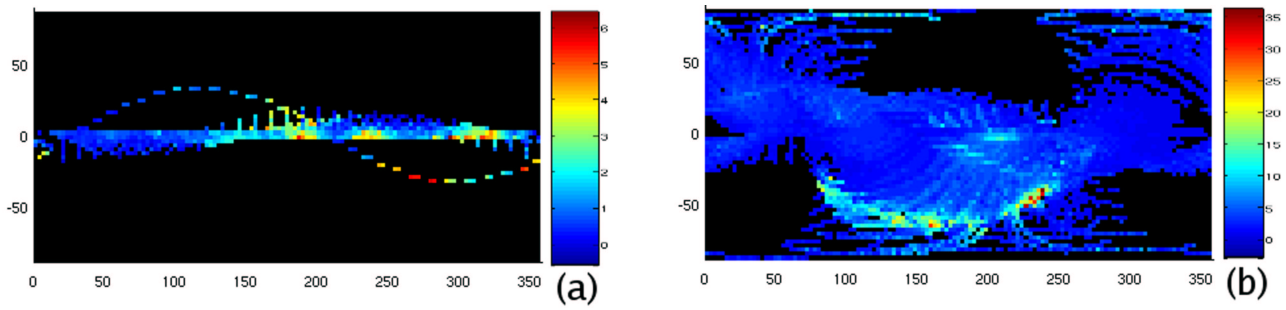


Figure 2.30: Skymaps of the average NPI count rate for NPI eclipse observations in (a) 2004 and (b) 2005 eclipse seasons. The plots are in ecliptic coordinate systems with longitude on the x-axes and latitude on the y-axes. The color scales are NPI count rates and the scales run from 0-6 $s^{-1}$ in (a) and from 0-35 $s^{-1}$ in (b). Black denotes no measurements. From *Holmström et al.* [2005].

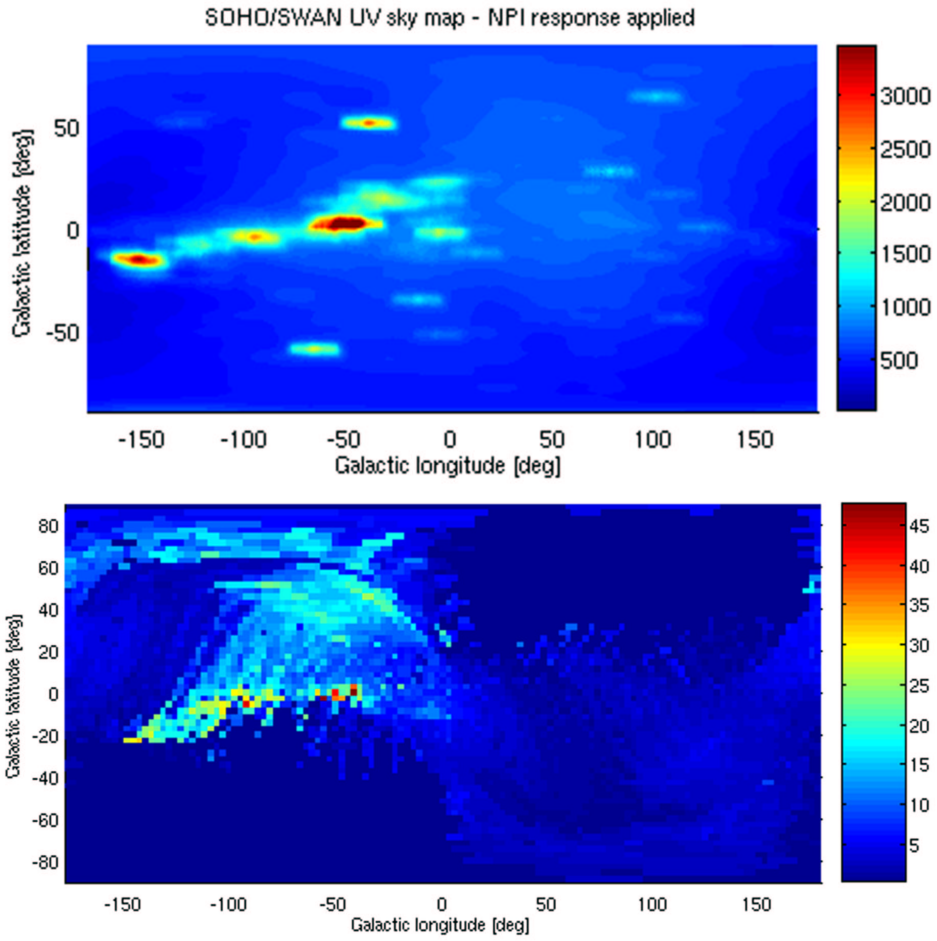


Figure 2.31: The top panel show a UV map (117-180 nm) in galactic coordinates from the SWAN instrument on SOHO [*Bertaux et al.*, 1995] that has been smoothed by the NPI angular response. The bottom panel are the NPI count rates also in galactic coordinates. The stronger signals in the NPI map directly to UV sources in the SWAN image, but not all signals can be explained but galactic UV sources. Adapted from *Holmström et al.* [2005].

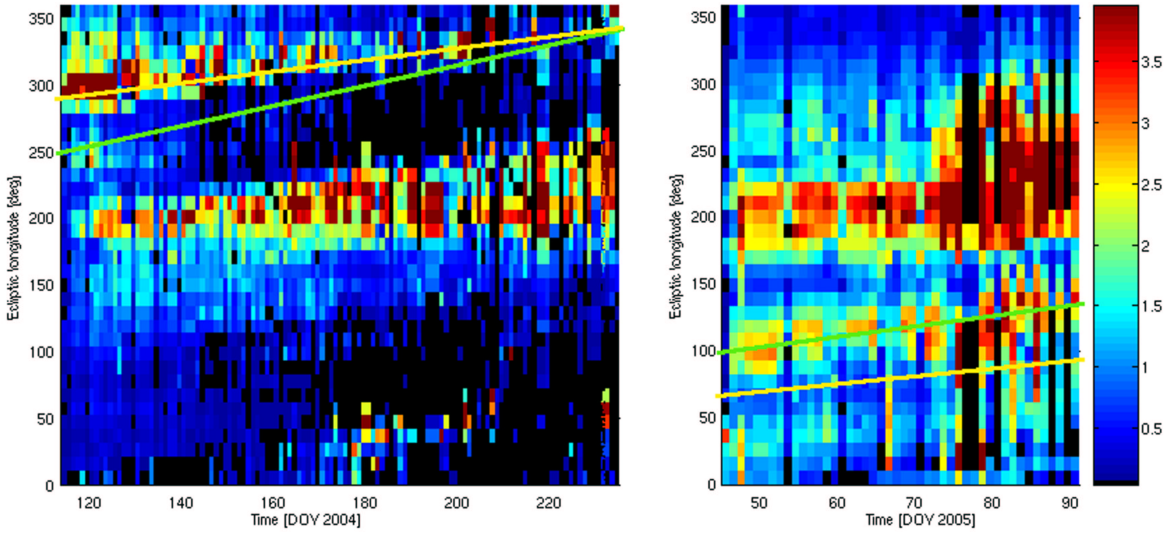


Figure 2.32: Time evolution of the average, daily NPI response in the ecliptic plane $\pm 5^{\circ}$ during (a) 2004 and (b) 2005 eclipse seasons. The x-axes are days from the start of the eclipse period and the y-axis are ecliptic longitudes. There are signals that do not follow the movement of the sun and are therefore not ENAs generated in the Mars-sun interaction nor are they constant in time, which would indicate stellar UV. From *Holmström et al.* [2005].

# Chapter 3

# Venus

*I have no data yet. It is a capital mistake to theorise before one has data. Insensibly one begins to twist facts to suit theories, instead of theories to suit facts.*
– Sherlock Holmes in "A Scandal in Bohemia", Sir Arthur Conan Doyle

**Venus is the brightest object in the sky except for the sun and the Moon. The surface of the planet is invisible beneath its dense atmosphere. Venus orbit lies inside Earth's orbit which means that when viewed from the Earth it shows phases like the Moon. Galileo observed this and put it forward as strong evidence that the heliocentric theory was correct. Mariner 2 was the first spacecraft to visit Venus in 1962. Since then over 20 spacecraft have visited the planet. The orbit of Venus is almost perfectly circular around the sun with an eccentricity of less than 1 %. The rotation of Venus is very slow. It completes one rotation around its axis in 243 Earth days, which is slightly longer than a Venusian year, which is 225 Earth days. This means that one day on Venus from sunrise to sunset is 117 Earth days, limited by the rotation around the sun and not only rotation around its own axis. The rotation around its own axis is retrograde, that is, in the opposite direction compared to the Earth and most of the other planets (Uranus and Pluto also have retrograde rotation). Venus is the second planet from the sun, but holds the record of the hottest surface temperatures in the solar system reaching over 480° C. The surface pressure is almost a hundred times that of the Earth. The atmosphere mostly consist of $CO_2$ (96.5 %) and $N_2$ (3.5 %) with clouds composed of $H_2SO_4$ in several layers. The upper atmosphere rotates much faster than the surface with wind speeds of 350 km/h in the upper cloud layer, but only a few km/h at the surface. An image in ultra violet (UV) light of Venus reveals dark patches where little or no UV is reflected. It is unknown what is absorbing the UV in those places. Venus does not have an intrinsic magnetic field.**[1]

[1] Reference: Bill Arnett, www.nineplanets.org

## 3.1 ENAs at Venus

As of yet, there have not been any dedicated ENA instrumentation in Venus orbit. The first ENA measurements there will be performed with the NPI and NPD sensors on the ASPERA-4 instrument on-board Venus Express in 2006.

Venus, similarly to Mars, lacks a global magnetic field and the solar wind can interact directly with the Venusian upper atmosphere. Fig. 2.3 could in principal also illustrate different ENA sources near Venus. A bow shock is formed that slows and compresses the solar wind ion flow. The deceleration and compression of the solar wind results in an increase of the frozen-in magnetic field. A magnetic barrier is formed. The magnetic and dynamic pressures of the solar wind is balanced by the thermal pressure at the ionopause. The currents generated in the ionosphere as a result of the interaction with the solar wind produce magnetic fields deviating the solar wind flux. During solar maximum the solar EUV is higher and ionization of the upper atmosphere increases. This causes the ionosphere to grow and the ionopause to move outward slightly [*Phillips and McComas*, 1991]. As discussed below, the ENA production depends on the position of this ionopause and on the neutral densities in the upper atmosphere. Note that, the Venusian exosphere does not change very much between solar maximum and minimum [*Keating et al.*, 1985].

Models to describe neutral densities in the upper atmosphere of Venus are mostly based on measurements with the Pioneer Venus Orbiter (PVO). A model for the thermal neutral hydrogen densities was developed from the measured densities of $H^+$, $O^+$, O, and $CO_2$ at 165 km altitude (exobase altitude at Venus is usually set to 170 km) and approximately 18° north latitude [*Brinton et al.*, 1980]. Dayside densities of approximately $5 \times 10^4$ cm$^{-3}$ increase at the terminators rapidly in the predawn sector, while the rise is slower between dusk and midnight. The peak density is about $4 \times 10^7$ cm$^{-3}$ between 4 and 5 local time (Fig 3.1). There is thus an asymmetry in the thermal hydrogen density referred to as the hydrogen bulge on the night side of Venus. The reason for this is the large day-night temperature contrast, which enhances winds that carry H and He from the dayside to the nightside [*Hartle et al.*, 1978]. The assymetry with the maximum density shifted toward dawn is an effect of the rapid rotation in the Venusian upper atmosphere compared to the surface [*Mayr et al.*, 1980]. The thermal oxygen density is modelled by *Mengel et al.* [1989] for altitudes between 80-200 km. Above 140 km the thermal oxygen density in the noon thermosphere is larger than in the midnight thermosphere. The hot oxygen corona on Venus primarily comes from dissociative recombination of $O_2^+$, but also from charge exchange processes between hot ionospheric atomic oxygen ions and neutral hydrogen and oxygen atoms. *Nagy et al.* [1981] have calculated the altitude profile and energy distribution of the hot oxygen constituent. They find that also the hot oxygen densities are higher on the dayside than on the nightside of Venus at high altitudes. A model to describe the hot constituent of the hydrogen neutral density with energies exceeding twice the escape energy (0.56 eV for hydrogen) produced by charge exchanging energetic protons or collisions with hot oxygen atoms was derived from Lyman-$\alpha$ airglow measurements [*Rodriguez et al.*, 1984]. It is in reasonable agreement with results from measurements on-board the Mariner 5 and 10, and Venera 11 and 12 spacecraft. *Keating et al.* [1985] have collected measurements and previous studies into a very comprehensive model called the Venus International Reference Atmosphere (VIRA) model.

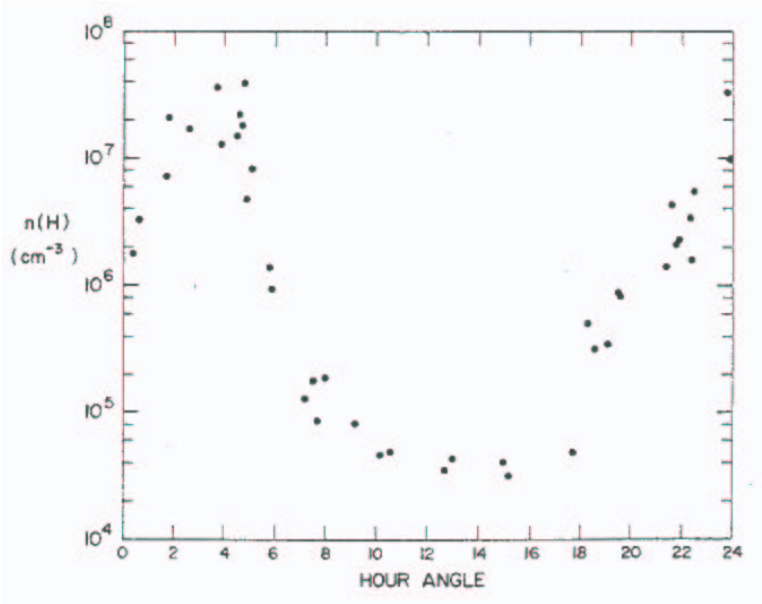


Figure 3.1: Thermal hydrogen density distribution near 165 km altitude. From *Brinton et al.* [1980].

*Fok et al.* [2004] have studied low energy ENA emissions based on extrapolated neutral densities from the VIRA model and plasma distributions around Venus from a three-dimensional MHD model [*Tanaka and Murawski*, 1997]. Hydrogen ENAs of energies 2 eV-10 keV and oxygen ENAs 30-680 eV were studied (Fig 3.2). Strong hydrogen ENA emissions coming from the dayside magnetosheath and from the sun direction were seen. The energy range for oxygen ENAs were chosen so that emissions from the low-altitude ionosphere and a faint increase from the hydrogen bulge on the nightside became visible. There is also a small ENA maximum in the ram direction of their simulated spacecraft.

Another simulation of ENAs at Venus was reported by *Gunell et al.* [2005c]. They have based their simulation on the neutral density models mentioned above and a semi- analytical MHD flow model [*Biernat et al.*, 1999, 2000] that numerically finds steady state solutions to the MHD equations, but uses analytical shapes for the ionopause and bow shock. The model is also extended to include mass loading. This is done by adding an ion source function on the dayside to model photoionization in that region. Based on this model, ENA emissions also appear to have two maxima (Fig 3.3), one in the direction of the sun and one from the Venus magnetosheath. ENA energies above 50 eV were considered. The maxima in the sun direction is attributed to charge exchange processes in the undisturbed solar wind itself upstream of the bow shock. The ENAs from the magnetosheath have a maximum at vantage points $\sim 110^\circ$ SZA in the noon-midnight plane. These results are in reasonable agreement with *Fok et al.* [2004] and the maximum ENA flux from the interaction region between the bow shock and the ionopause is $3.8 \times 10^6$ cm$^{-2}$ sr$^{-1}$ s$^{-1}$ compared to $1.4 \times 10^6$ cm$^{-2}$ sr$^{-1}$ s$^{-1}$ from the upper left panel in Fig. 3.2. However, as *Gunell et al.* [2005c] conclude,

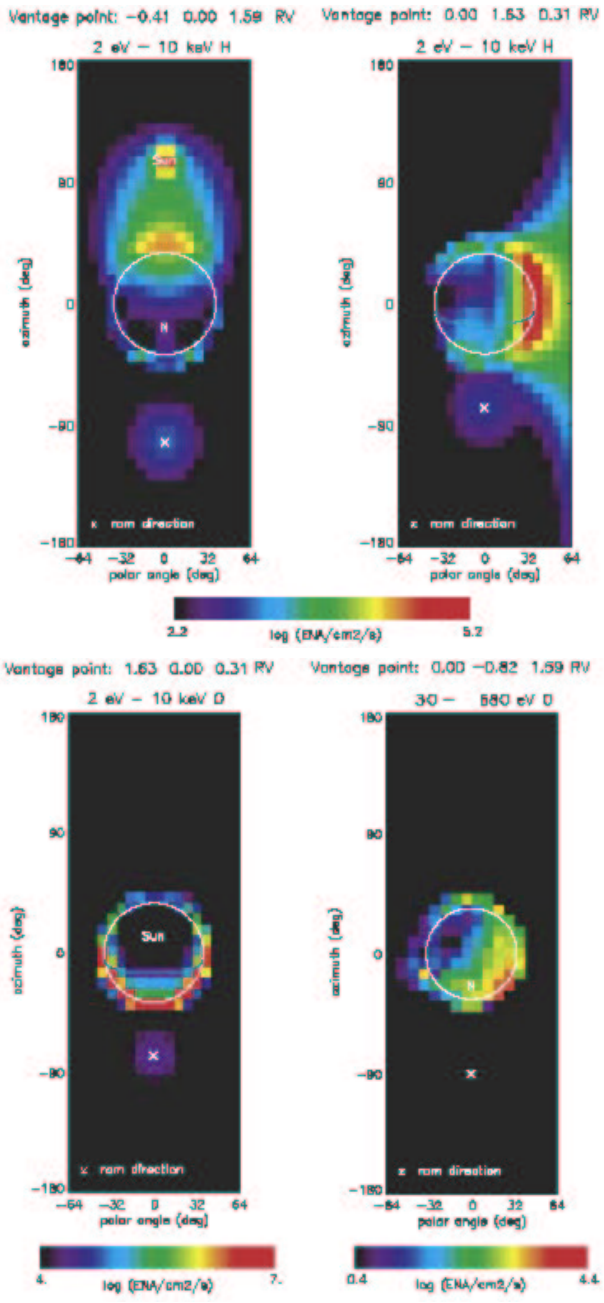


Figure 3.2: Simulated ENA images based on a three dimensional MHD model and the VIRA neutral distribution model. The images show, from left to right, top to bottom, hydrogen ENAs from a vantage point in the noon-midnight meridian, hydrogen ENAs from a vantage point in the dawn-dusk plane, oxygen ENAs from a vantage point in the dawn-dusk plane, and oxygen ENAs from a vantage point in the noon-midnight meridian. From *Fok et al.* [2004].

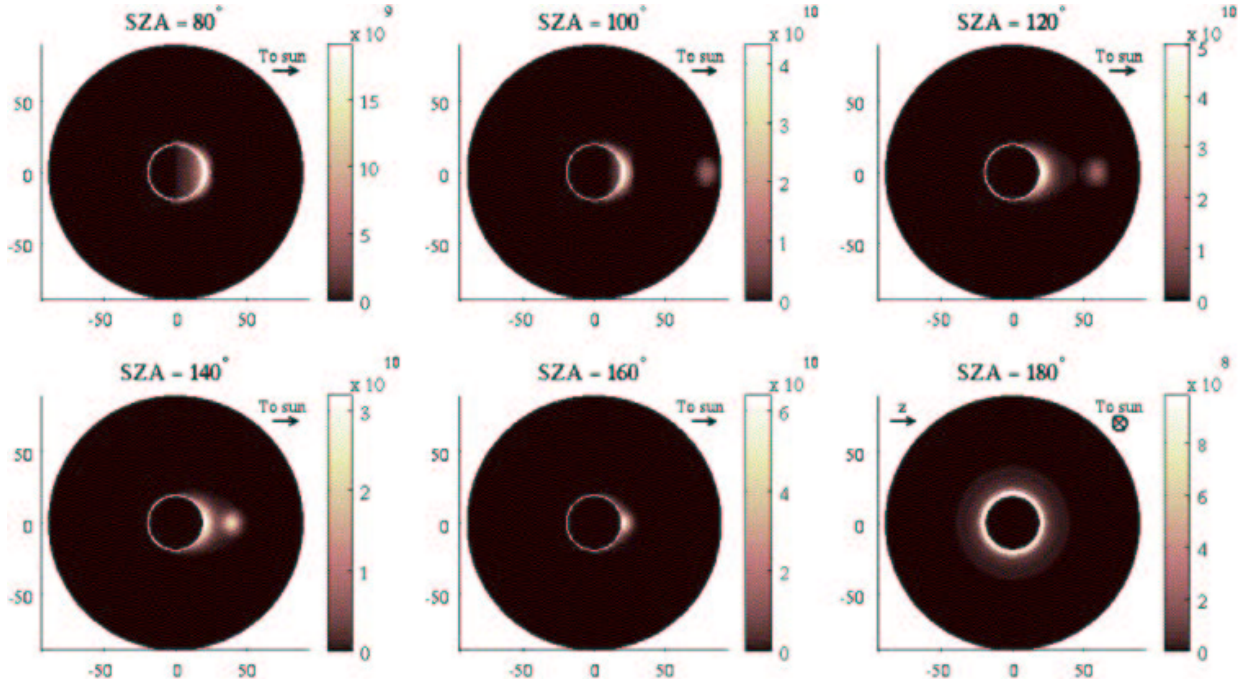


Figure 3.3: Simulated ENA images of Venus from a distance of 3 $R_v$. The images show from left to right, top to bottom the view from 80°, 100°, 120°, 140°, 160°, and 180° SZA. The sun is to the right and each image has its own intensity scale. ENA energies above 50 eV are considered. From *Gunell et al.* [2005c].

observations of the ENA emissions from Venus are needed to verify the models.

A comparison between the ENA simulations based on the different models of the plasma distribution as well as ENA production at Mars and Venus have also been made by *Gunell et al.* [2005c]. Their results during solar minimum indicate that lower ENA production and escape rates are to be expected from Venus. The total hydrogen ENA production at Venus is $7.8 \times 10^{24}$ $s^{-1}$. That is 1/3 of the ENA production at Mars, which is $2.4 \times 10^{25}$ $s^{-1}$ for solar minimum. At solar maximum the neutral density at Mars decrease at high altitudes and the ENA environment becomes similar to Venus.

## 3.2 Venus Express and ASPERA-4

Venus Express hardware is, to a large extent, based on spares from the Mars Express and Rosetta missions. Venus Express was launched less than three years after the mission was approved. This is considered to be extremely fast for a mission of this magnitude. The same philosophy of re-using spare models also included the payload. Four of the seven Venus Express instruments have heritage

or are adopted spares from Mars Express. One instrument is partially a spare from the Rosetta mission, and two are new developments. Venus Express does not include a lander. In some cases, as with the ASPERA-4 instrument the philosophy was to change as little as possible from the Mars Express design. Some changes were necessary because of the harsher environment in Venus orbit compared to Mars orbit. The changes on ASPERA-4 in general and on the NPI sensor in particular are reviewed below. Venus Express was successfully launched on 9 November 2005. It will arrive at Venus in April 2006 and start scientific operations in May/June of that year. The scientific objectives of Venus Express are to make the most comprehensive investigation yet of the Venusian atmosphere and its interaction with the surface and interplanetary environment. Among the many unanswered questions that Venus Express will search for answers to are: what drives the fast rotation of the atmosphere? What is the origin of the ultra violet marks at the cloud tops? And what governs the atmospheric escape processes?

The ASPERA-4 instrument (Fig. 3.4) addresses the last of these questions. The instrument is a copy of Mars Express ASPERA-3 (Section 2.2). As its predecessor it consists of the five sensors ELS, IMA, NPI, NPD1 and NPD2 that measure electrons, ions, and ENAs. The most notable differences compared to the ASPERA-3 instrument concern the instrument thermal design. There were also changes made to cope with the harder radiation requirements of the Venus Express mission. Some electrical components have been upgraded to be radiation tolerant, while others have received protective shielding in the form of tantalum (Ta) plating directly on the components. Also, ELS is surrounded by a metallic skirt to protect the ELS electronics located at the bottom of the sensor very close to the lid of the NPI sensor. There were also a number of other minor design changes and upgrades included in the ASPERA-4 instrument. The scanner has improved driver electronics, IMA has better angular resolution due to updated high voltage supplies with better accuracy and better mass resolution due to an entirely new anode design, and the NPI has slightly higher thresholds on the preamplifiers, which has resulted in lower dark count and curing the sector priority effect as discussed in the next section.

## 3.3 ASPERA-4/NPI particle calibrations

The ASPERA-4 NPI was calibrated against particles in the same facilities as the ASPERA-3 NPI (Section 2.4). The procedure and philosophy of investigating one sector in detail, then making relative measurements of the other 30 sectors was also identical. The detailed measurements were made on sector 4. Table 3.1 lists the different tests and calibrations performed on the ASPERA-4 NPI and the various beam parameters used. The sensor measurement configuration for the particle calibration of the ASPERA-4 NPI was identical to the configuration shown in Fig. 2.9.

Tests were conducted prior to the integration of the ASPERA-4 NPI to study the priority effect (see Section 2.4.1) in more detail. This time, the dependence of the priority effect on the MOCAD preamplifier thresholds was investigated. A setup similar to the one shown in Fig. 2.11, but with the threshold of one MOCAD adjustable from outside the tank was used. MCP bias was raised to 2470 V. The small, 0.7 mm diameter beam (5 keV, $H_2O^+$) was centered on sector 10. The preamplifier threshold was then increased from 0.5 V to 2.2 V in steps of 0.05 V, and the count

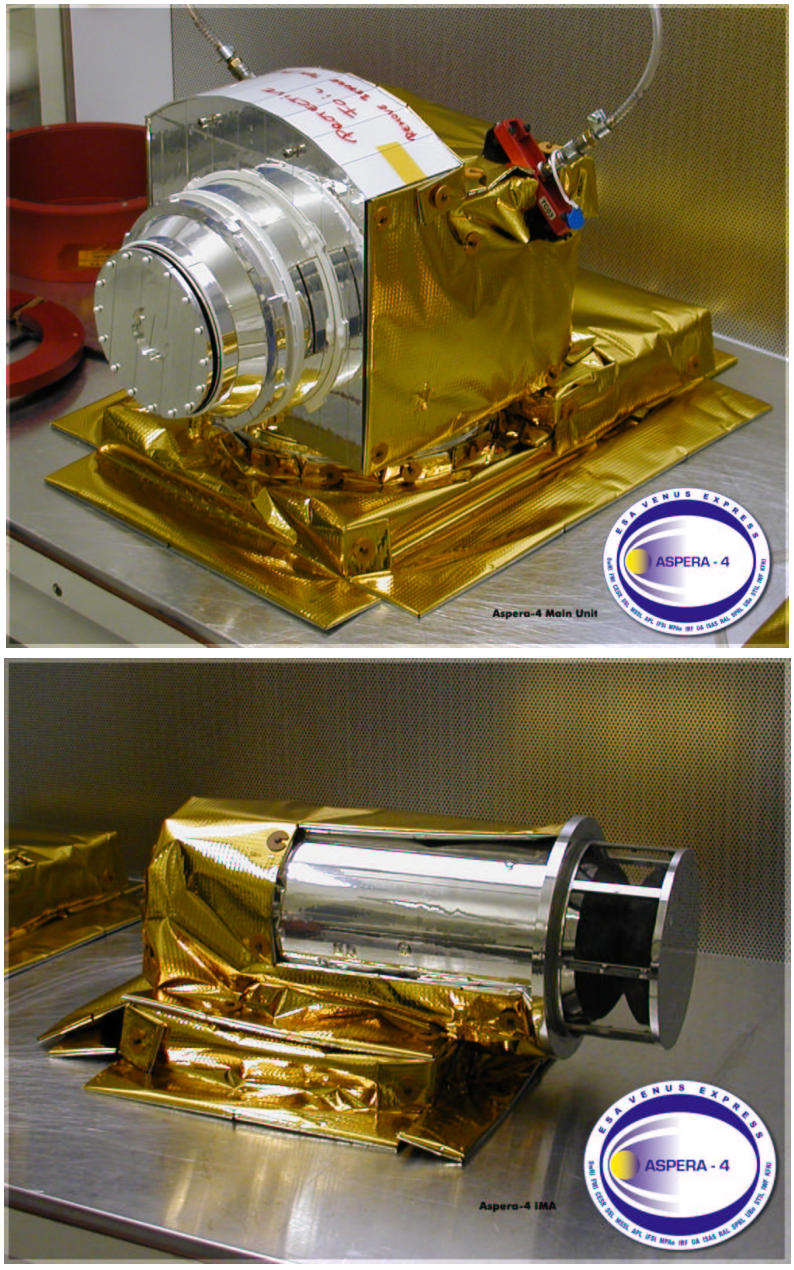


Figure 3.4: The ASPERA-4 instrument consist of five different sensors: The Electron Spectrometer (ELS), Neutral Particle Imager (NPI), and Neutral Particle Detector (NPD1 & NPD2) are mounted on the ASPERA-3 Main Unit (left). The Ion Mass Analyzer (IMA) (right) is separated from the Main Unit.

Table 3.1: Calibrations and functional tests performed on the ASPERA-4 NPI.

| Test | Species | Energy |
|---|---|---|
| Priority effect tests | $H_2O^+$ | 4.8 keV |
| Dark current calibrations | – | – |
| Angular response function calibrations | $H_2O^+$ | 4.8 keV |
| Relative response calibrations | $H_2^+$ | 4.8 keV |
| Efficiency calibrations | $H_2O^+$, $H^+$ | 0.30, 0.67, 1.2 and 4.8 keV |

rate in sectors 10 and 11 was monitored. Fig. 3.5 shows a plot of the count rate in sectors 10 and 11 for different threshold settings. The count rate is normalized to the maximum count rate in the respective sectors and the plot therefore shows the count rate percentage compared to the count rate at 0.5 V thresholds. Since the percentage in sector 11 falls faster than the percentage in sector 10, the conclusion is that the pulses responsible for the priority effect have low pulse heights and raising the preamplifier thresholds in the sensor should reduce the effect. The final preamplifier thresholds for the ASPERA-4 NPI is set to 0.78 V (compared to the ASPERA-3 NPI thresholds of 0.52 V). After integration, a functional test of the NPI sensor was performed to verify the basic functionality of the sensor. The sector priority effect observed in the ASPERA-3 NPI was found to be negligible in the ASPERA-4 NPI (Fig. 3.6). The nominal operating MCP bias voltage is set to 2430 V.

The measurements of dark current were made at the beginning of the calibrations and two weeks later at the end of the calibrations (Fig. 3.7). The is a clear anomally in sector 22, but it is significantly lower at the end of the calibrations (Fig. 3.8). The anomaly is not visible at all in the calibrations against UV photons, which were performed almost four months later (see Section 3.4). It is therefore concluded that the "hot spot" was caused by some impurity on, or within the MCP plates at the position corresponding to sector 22. Table 3.2 lists the total dark count for each NPI sector during 60 seconds sampling at different MCP bias. The dark count rate is a factor $\sim 10$ higher for the ASPERA-3 NPI compared to the ASPERA-4 NPI. This is an effect of the higher preamplifier thresholds on ASPERA-4 NPI.

A thorough investigation of all 30 open sectors would be too time consuming. The calibration plan of the NPI sensor therefore includes a full investigation of the response of one sector only (sector 4) and then an investigation of the relative response of the other sectors. The characterization of one reference sector includes the angular response (scans of azimuth and elevation angles) at different beam energies. Also, the efficiency was calculated for different energies. When the response from the reference sector was known, a relative response of the other sectors was found from a 360° azimuth scan with elevation angle fixed at the maximum response of the reference sector.

Full azimuth and elevation scans were performed on sector 4 and responses for the nominal MCP bias (2430 V) and an additional two MCP bias settings (2380 V and 2470 V) were recorded. The normalized responses are in Fig. 3.9. The ion beam configurations for these measurements can be

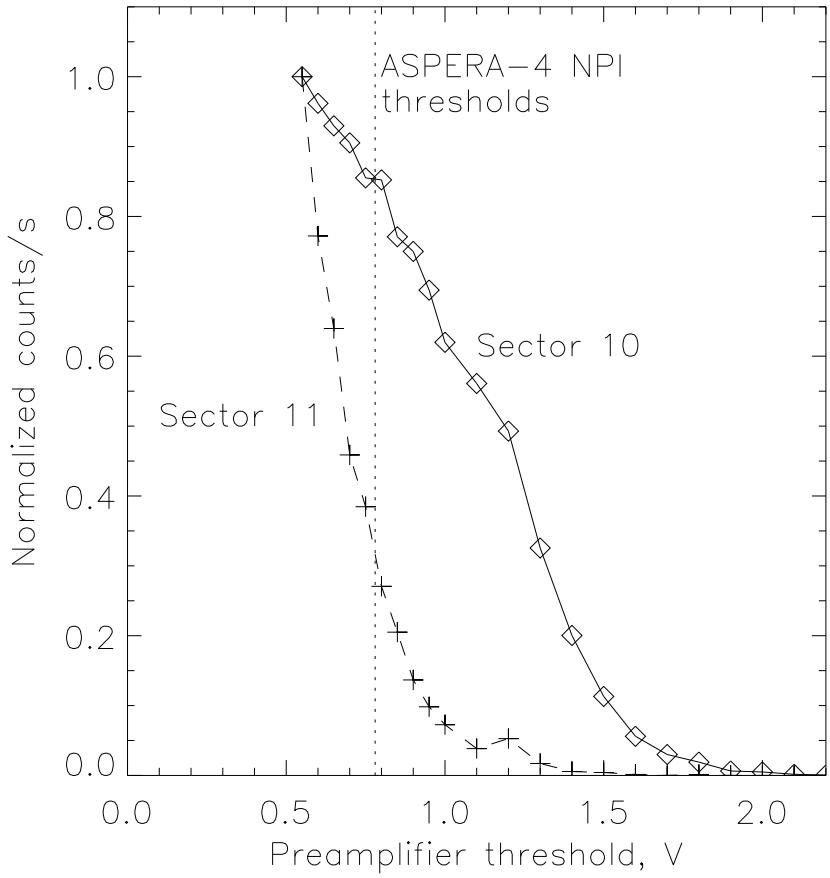


Figure 3.5: The response in sectors 10 and 11 with a constant beam (4.8 keV, $H_2O^+$) in the center of sector 10. The MCP bias was 2470 V and the maximum count rates (normalization factors) in sectors 10 and 11 were 5959 and 702 counts $s^{-1}$ respectively.

Table 3.2: Dark count at different MCP bias. Sampling time is 60 seconds.

| Sector | MCP bias 2340 V | MCP bias 2380 V | MCP bias 2430 V | MCP bias 2470 V |
|---|---|---|---|---|
| 0 | 0 | 0 | 4 | 5 |
| 1 | 2 | 3 | 5 | 2 |
| 2 | 0 | 5 | 5 | 5 |
| 3 | 0 | 1 | 6 | 10 |
| 4 | 1 | 2 | 4 | 5 |
| 5 | 2 | 3 | 2 | 3 |
| 6 | 1 | 0 | 6 | 4 |
| 7 | 0 | 2 | 4 | 4 |
| 8 | 1 | 1 | 3 | 4 |
| 9 | 1 | 1 | 4 | 6 |
| 10 | 2 | 2 | 2 | 9 |
| 11 | 0 | 2 | 2 | 4 |
| 12 | 1 | 2 | 6 | 5 |
| 13 | 0 | 0 | 3 | 5 |
| 14 | 0 | 2 | 2 | 11 |
| 15 | 0 | 1 | 2 | 3 |
| 16 | 3 | 0 | 5 | 6 |
| 17 | 1 | 3 | 4 | 3 |
| 18 | 1 | 3 | 3 | 7 |
| 19 | 1 | 3 | 3 | 7 |
| 20 | 0 | 3 | 4 | 4 |
| 21 | 0 | 2 | 5 | 5 |
| 22 | 0 | 4 | 23 | 59 |
| 23 | 1 | 2 | 2 | 6 |
| 24 | 2 | 0 | 1 | 4 |
| 25 | 1 | 3 | 1 | 4 |
| 26 | 1 | 2 | 1 | 4 |
| 27 | 1 | 1 | 3 | 3 |
| 28 | 1 | 2 | 3 | 3 |
| 29 | 0 | 1 | 5 | 4 |
| 30 | 2 | 1 | 5 | 6 |
| 31 | 3 | 4 | 3 | 5 |
| Total | 29 | 61 | 131 | 215 |

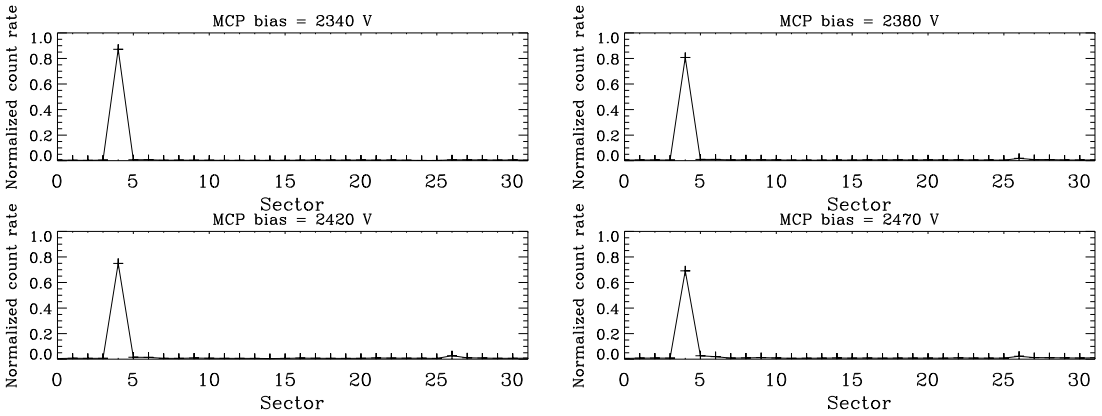


Figure 3.6: Measurements with the calibration beam directed into NPI sector 4 (neighboring sectors were mechanically blocked) for different MCP bias. The response does not notably change sector with higher MCP bias as was the case for the ASPERA-3 NPI (compare with Fig. 2.10).

found in Table 3.1. A comparison to the angular response function of one sector on ASPERA-3 NPI is shown in Fig. 3.10. The plot shows the response in the central azimuth and elevation planes of the NPI sector aperture. The angular response of the ASPERA-4 NPI is slightly narrower than the ASPERA-3 NPI angular response at FWHM. The priority effect causes the slight asymmetry toward the higher numbered neighboring sector (towards negative azimuth angles in the plot). This effect is larger for the ASPERA-3 NPI than for the ASPERA-4 NPI.

The azimuth scan response for the NPI sensor at nominal MCP bias (2430 V) is shown in Fig. 3.11 and the beam parameters used are in Table 3.1. The relative sensitivity of the different sectors are in Table 3.3. It shows the averaged response of the sector centers (azimuth center $\pm 2°$) for each sector relative to sector 4 and should be used to normalize the different sector responses. The relative response showed that the reference sector 4 has much higher response compared to the other sectors.

The particle efficiency $\varepsilon$ of the NPI sensor was measured in the same way as for the ASPERA-3 NPI and calculated using equation 2.2. The measurement beam parameters for this measurement are in Table 3.1. Fig. 3.12 is a plot of the efficiency to $H_2O^+$ and $H^+$ ions with and $H_2O^+$ ions without neighboring sectors blocked. Blocking the neighboring sectors has a negative effect on the efficiency. Because the calibration beam is larger than one sector aperture, part of it is injected into the neighboring sectors. A small portion ($\leq$ 10 %) of these particles reaches sector 4 from reflections at the neighboring sectors' target block surfaces (Fig. 3.11). In space ENA sources are much larger than one NPI sector aperture. ENAs from these sources will therefore always cover also the neighboring NPI sectors and the situation corresponding to the blocked neighboring sectors will never occur. The particle mass seem to have little effect on the efficiency at least at energies $\geq$ 1 keV (Fig. 3.12, right). A comparison between the efficiencies of ASPERA-4 and the ASPERA-3 NPI is shown in Fig. 3.11. The efficiency in the ASPERA-4 NPI is slightly higher than for ASPERA-3

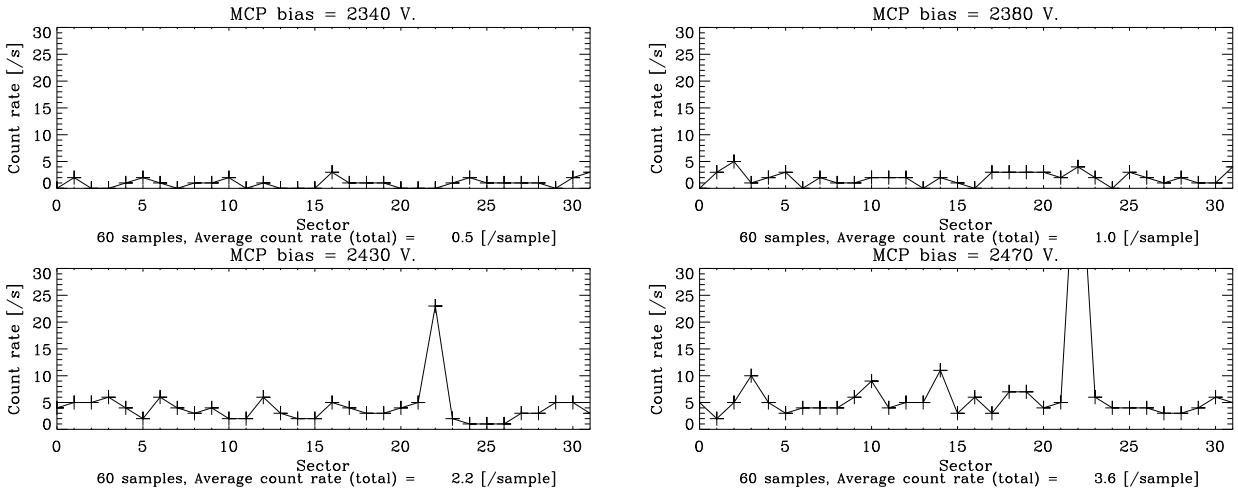


Figure 3.7: Dark count rate (60 s sampling time) for all sectors at different MCP bias.

NPI, even with the higher MOCAD thresholds.

Since the geometry of the sensor has not changed the same geometrical factor as for the ASPERA-3 NPI can also be assumed for the ASPERA-4 NPI. The geometrical factor of $G = 2.7 \cdot 10^{-3}$ cm$^2$ sr is used.

## 3.4 ASPERA-4/NPI Lyman-$\alpha$ photon calibrations

Because of programmatic reasons UV calibrations have not been performed on the ASPERA-3 NPI, but it was possible to do for the ASPERA-4 NPI. The UV calibrations have been conducted at the UV calibration facility of the Lunar and Planetary Laboratory at the University of Arizona. In their facility UV light is generated in a DC glow discharge light source. The discharge excites a flowing gas (H/He mixture at a ratio of about 1:50 in this case) to emit its characteristic spectrum. Light from the glow discharge enters a Seya-Namioka monochromator, which selects the wavelength of interest (spectral passband is about 1 nm) and also collimates the exit beam into a vacuum tank. Inside the vacuum tank is a gimbal that can rotate the sensor under test in two perpendicular axes and translate it in a plane perpendicular to the UV beam. Just after the beam enters the vacuum tank, a portion of it strikes a channeltron beam monitor. This channeltron continuously monitor the beam intensity during the measurements. Following the calibrations, another, absolutely calibrated channeltron can be substituted in the position of the test sensor. It is used to map the intensity of the beam, and to thereby determine (from intercalibration with the beam monitor channeltron) the absolute photon flux into the entrance aperture of the calibrated sensor during the calibrations.

The NPI electrical configuration for the UV calibrations was identical to that of the particle calibration. Similarly to the particle calibration the approach was to find the detailed UV response of only one of the 32 sectors of the NPI. Then make a relative measurement of the central position

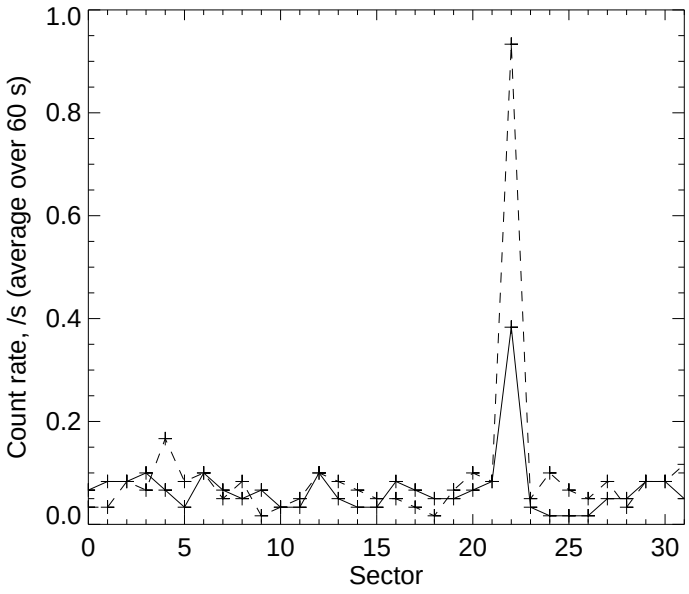


Figure 3.8: Average dark counts/s over 60 s for all sectors (MCP bias 2430 V) at the start of calibrations (dashed line) and at the end of calibrations (solid line). The anomaly in sector 22 has significantly decreased.

of the other 31 sectors.

To be able to produce a count in the NPI a photon will have to, first, hit the aperture within a specific angular range. The deflection plate surfaces in the NPI are coated with copper sulfide normally used as UV-absorbing coating. Assuming a photon impacts the NPI target block it may be absorbed or reflected towards the MCP stack. In case of absorbtion there will be a low energy photoelectron ejected from the target block surface. Since the front of the MCP plates are negativly biased at $-2430$ V such electrons cannot reach the MCP detector and there is no count associated with the photoelectron. The NPI target block is coated with DAG-213, a resin-based graphite dispersion similar to aqua-DAG, which is a graphite dispersion in water. The photoelectric properties of DAG-213 is expected to be close to those of aqua-DAG. The expected efficiency of the target block to UV photons ($\varepsilon_{tb}$) is around $10^{-5}$ derived by *Barabash et al.* [1995] in simplified UV calibrations of the similar instrument PIPPI on the Astrid-1 spacecraft (see Section 1.2.6 for PIPPI description). However, there could be variations in the coating between different target blocks. The MCP UV detection efficiency for Lyman-$\alpha$ wavelengths ($\varepsilon_{MCP}$) is $\sim 1$ %. So the combined expected efficiency of the NPI for Lyman-$\alpha$ photons is

$$\varepsilon_{Ly} = \varepsilon_{tb} \cdot \varepsilon_{MCP} = (10^{-5}) \cdot (10^{-2}) = 10^{-7}. \tag{3.1}$$

During the calibrations the UV-intensity was continuously monitored using the channeltron beam

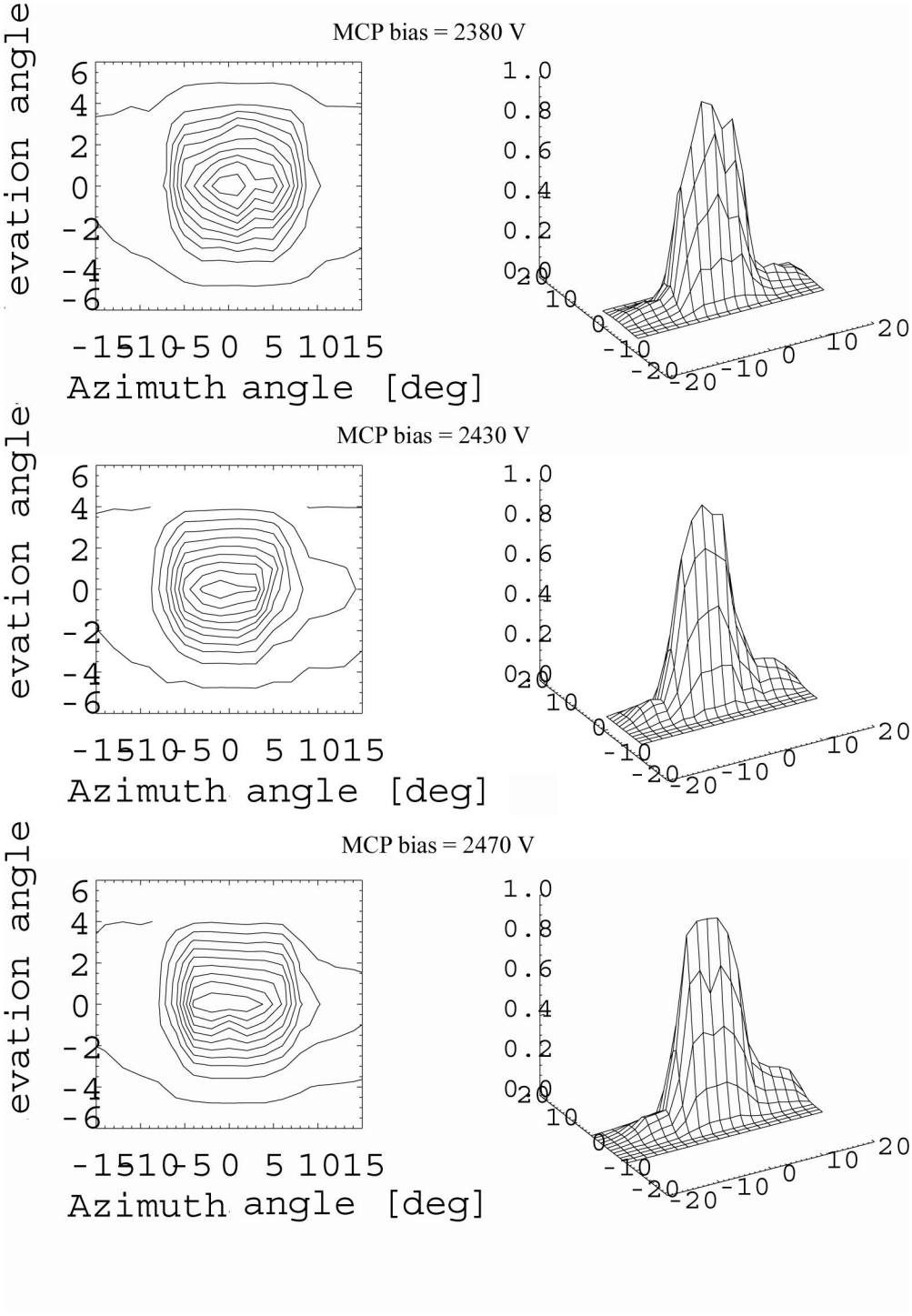


Figure 3.9: Angular scan of sector 4 at MCP bias 2380, 2430, and 2470 $V$.

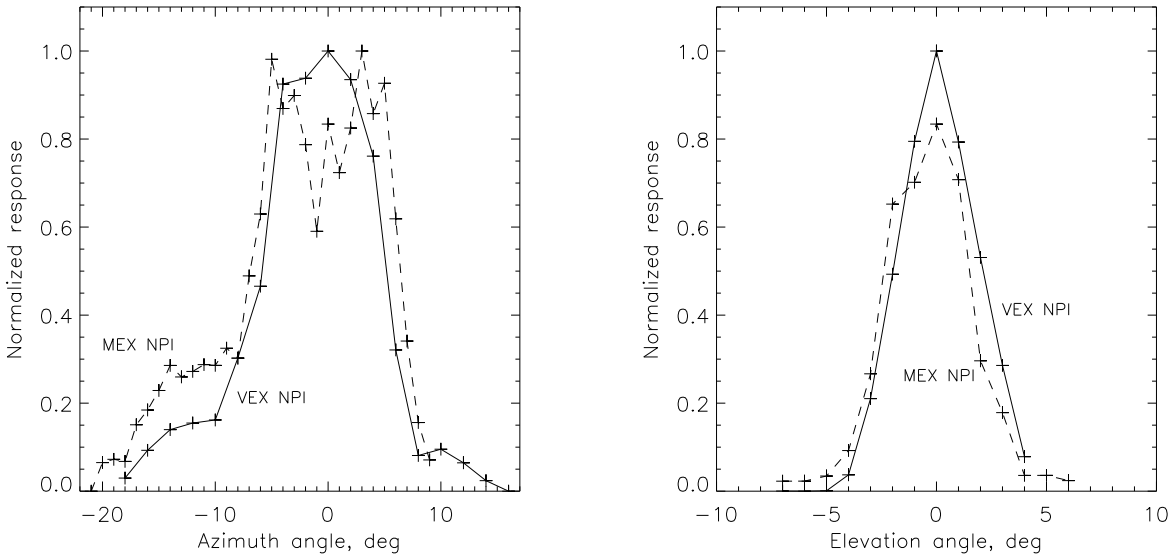


Figure 3.10: Comparison between the ASPERA-3 (MEX) NPI (dashed lines) and ASPERA-4 (VEX) NPI (solid lines) angular response functions. Azimuth angle is defined in the plane along the large dimension of an NPI aperture and elevation along the short. The measurements were made at nominal MCP bias for the respective sensors.

monitor. Since only a fraction of the beam is monitored, estimations of the total photon intensity rely on intercalibrations of the beam monitor and an absolutely calibrated channeltron used to characterize the beam immediately following the NPI calibrations. A beam map (Fig. 3.14) was acquired using the absolutely calibrated channeltron. From the beam map and intercalibration a rough estimate of the photon intensity into the NPI aperture at different readings of the beam monitor was found (the scaling factor was $k = 386$, based on a simple fit to the beam map in Fig. 3.14). A common beam monitor reading during the calibrations was $C_{bm} = 18$ kHz. The estimated count rate of the NPI when the beam is pointed into the center of an aperture (as in Fig. 3.14) based on the efficiency from equation 3.1 is then:

$$R_{UV} = C_{bm} \times k \times \varepsilon_{Ly} = (18 \cdot 10^3) \times (386) \times (10^{-7}) = 0.7 \text{ s}^{-1} \text{ (estimated)},$$

compared to a recorded count rate during the calibrations of $\sim 32$ s$^{-1}$. To define the absolute NPI sensitivity calibrations were conducted at three different Lyman-$\alpha$ intensities against the parallel UV beam. The beam monitor read out, Lyman-$\alpha$ intensity and NPI count rate recorded are in Table 3.4 and the result is shown in Fig. 3.15.

The NPI angular response against UV was measured. Because of limited space and restricted movement of the gimbal in the calibration tank, the angular scan was made with respect to the aperture plane of the NPI (sector 4). There should therefore not be any counts in any other sector

Table 3.3: Sensitivity (measured count/s) to particles for all sectors relative to the sensitivity of sector 4.

| Sector | 0 | 1 | 2 | 3 | 4 | 5 | 6 | 7 | 8 | 9 | 10 |
|---|---|---|---|---|---|---|---|---|---|---|---|
| Relative sensitivity | 0.45 | 0.60 | 0.74 | 0.88 | 1.00 | 0.95 | 0.41 | 0.28 | 0.41 | 0.23 | 0.22 |
| Sector | 11 | 12 | 13 | 14 | 15 | 16 | 17 | 18 | 19 | 20 | 21 |
| Relative sensitivity | 0.27 | 0.46 | 0.46 | 0.44 | 0.00 | 0.00 | 0.52 | 0.47 | 0.49 | 0.49 | 0.47 |
| Sector | 22 | 23 | 24 | 25 | 26 | 27 | 28 | 29 | 30 | 31 | |
| Relative sensitivity | 0.47 | 0.29 | 0.36 | 0.26 | 0.40 | 0.39 | 0.37 | 0.63 | 0.48 | 0.58 | |

Table 3.4: Recorded count rate for different Lyman-$\alpha$ photon intensities.

| $R_{BeamMonitor}$ [kHz] | I [$s^{-1}$] | $C_{NPI}$ [$s^{-1}$] |
|---|---|---|
| 3.4 | $1.4 \cdot 10^6$ | 5.5 |
| 9.0 | $3.5 \cdot 10^6$ | 18.0 |
| 18.0 | $6.9 \cdot 10^6$ | 31.9 |

than number 4. If there was, it must be a result of internal reflections since photons from the beam were directed into sector 4 only for all angles. The results of the angular scan is shown in Fig. 3.16. Fig 3.16 (bottom) also shows the sum of all counts during the angular scan in all sectors. There are visible counts in sectors 3, 4, and 5. The response in sectors 3 and 5 were 10.5 % and 15.6 % of the sector 4 counts, respectively.

The response to Lyman-$\alpha$ photons in the other 31 sectors was measured only in the center-aperture of each sector following the approach similar to the particle calibrations. The geometry of the calibration tank allowed only six sectors to be measured at a time. Then the vacuum had to be broken and the NPI remounted. Measurements of all 32 sectors required six mountings with pumping time in between. The relative measurements was thus a rather lengthy process. The beam intensity varied somewhat between mountings. The intensity is normalized in Fig. 3.17. Compensation is based on continuous beam monitor read outs during the measurements.

To ensure that there are no reflections from the deflector spokes separating the different sectors a translation measurement was carried out. The size of the beam did not cover the entire width of the NPI, which was why a translation was required to verify that reflections from the spokes of sectors other than the sector in the direction of the UV source could reach the detector. Sector aperture number 4 was centered on the UV beam and the NPI was then translated horizontally according to Fig. 3.18. The space in the tank limited the translation to less than the full diameter of the NPI. However, reflections from aperture spokes further away than the translation range is

Table 3.5: Sensitivity (measured count/s) to UV for all sectors relative to the sensitivity of sector 4.

| Sector | 0 | 1 | 2 | 3 | 4 | 5 | 6 | 7 | 8 | 9 | 10 |
|---|---|---|---|---|---|---|---|---|---|---|---|
| Relative sensitivity | 1.18 | 0.84 | 1.014 | 1.03 | 1.00 | 0.88 | 0.53 | 0.54 | 0.78 | 0.69 | 0.84 |
| Sector | 11 | 12 | 13 | 14 | 15 | 16 | 17 | 18 | 19 | 20 | 21 |
| Relative sensitivity | 0.77 | 0.77 | 0.62 | 0.88 | 0.00 | 0.00 | 1.00 | 0.87 | 0.77 | 0.84 | 0.74 |
| Sector | 22 | 23 | 24 | 25 | 26 | 27 | 28 | 29 | 30 | 31 | |
| Relative sensitivity | 0.67 | 0.50 | 0.68 | 0.57 | 0.81 | 0.98 | 0.96 | 1.05 | 0.93 | 1.50 | |

highly unlikely as it would require a multitude of reflections to reach even the target block. The resulting count in sector 4 is shown in Fig. 3.19 (left).

The UV calibration showed that the NPI is sensitive to Lyman-$\alpha$ photons. The detection efficiency is $\varepsilon_{Ly} \simeq 5 \times 10^{-6}$ in the photon intensity range of $0 - 10^7$ s$^{-1}$ in one sector. Some internal reflections are present in the NPI since there were counts in the neighboring sectors during the angular scan measurement even though the beam was directed into sector 4 only at all times during that measurement. The neighboring sector count rate from such reflections were on the order of 15 %.

## 3.5 Simulated ENA images from ASPERA-4/NPI at Venus

The plane of the Venus Express polar orbit in an inertial frame, rotate around the planet (Fig. 3.20). When it is in the noon - midnight plane, the vantage points it provides will be closed to the ones considered in the simulations shown in Fig. 3.3. To simulate expected ENA images from NPI it is thus sufficient to take calculated ENA fluxes *Gunell et al.* [2005c] shown in Fig. 3.3 and converted them to count rates using the calibrated NPI efficiencies and angular resolutions. Fig. 3.21 shows the expected images assuming an attitude where the scanner rotational axis points to the center of Venus. We assumed the angular pixel $11.25° \times 5.6°$. The higher FWHM over the elevation angle came from the assumed 32 s spin period. To simplify the calculations at this initial phase of the analysis we assumed the angular response function to be flat. Smearing due to the scanner motion is also neglected. Equation 2.4, with ASPERA-4 NPI values is used to convert the ENA intencity into count rates. An efficiency of $\varepsilon = 10^{-3}$ was used.

The expected counts rate for a single scan are quite low and typically within the range $10^{-1}$ to $10^1$ counts/s. Therefore integrations of several scans will be required to improve statistics provided the background is low. The obtained results are not unexpected because as pointed out in Section 3.1 the simulated ENA intensities from Venus are lower, down to one order of magnitude less, than at Mars. Another, major problem to face is much higher UV fluxes at Venus than at Mars. The

maximum solar Lyman-$\alpha$ flux measured by the PVO spacecraft was $4.76 \times 10^{11}$ cm$^{-2}$ s$^{-1}$ during solar maximum [*Ajello et al.*, 1987]. Based on the NPI photon calibrations, the NPI count rate in direct sunlight would then be on the order of $10^6$ s$^{-1}$. UV emissions from the hydrogen exosphere (dayglow) are expected to be higher at Venus than at Mars. Measurements with a Lyman-$\alpha$ photometer on-board the Venera 9 spacecraft showed that dayglow intensities decrease from $\sim 10.5$ to 0.5 kilo Rayleigh for lines of sight 0-4500 km above the limb [*Bertaux et al.*, 1978] (measured from the dayside). If one Rayleigh in this case corresponds to $1 \times 10^6/4\pi = 7.96 \times 10^5$ photons cm$^{-2}$ sr$^{-1}$ s$^{-1}$ then, from the photon calibrations, the NPI response is:

$$1000 \times 7.96 \times 10^5 \times G \times \varepsilon_{Ly} = 10.7 \text{ counts kR}^{-1} \text{ s}^{-1}.$$

This means that the count rate in the NPI from Lyman-$\alpha$ dayglow close to the limb exceed 100 counts/s. This should be compared with the expected ENA count rates of 0.1 to 10 counts/s. It became clear from the Mars Express mission that NPI can not conduct dayside measurements when the planet's limb is within its field of view and this will be the case also for Venus. However, similarly to Mars one can observe ENA emissions from close to the ionopause and on the night side but they will require integration times of the order of 10 sec provided 100 % duty cycle that might be difficult to achieve on a single orbit due to fast spacecraft motion near the pericenter. Therefore, statistics will be accumulated over several orbits and the obtained images will present only a general picture of the interaction region.

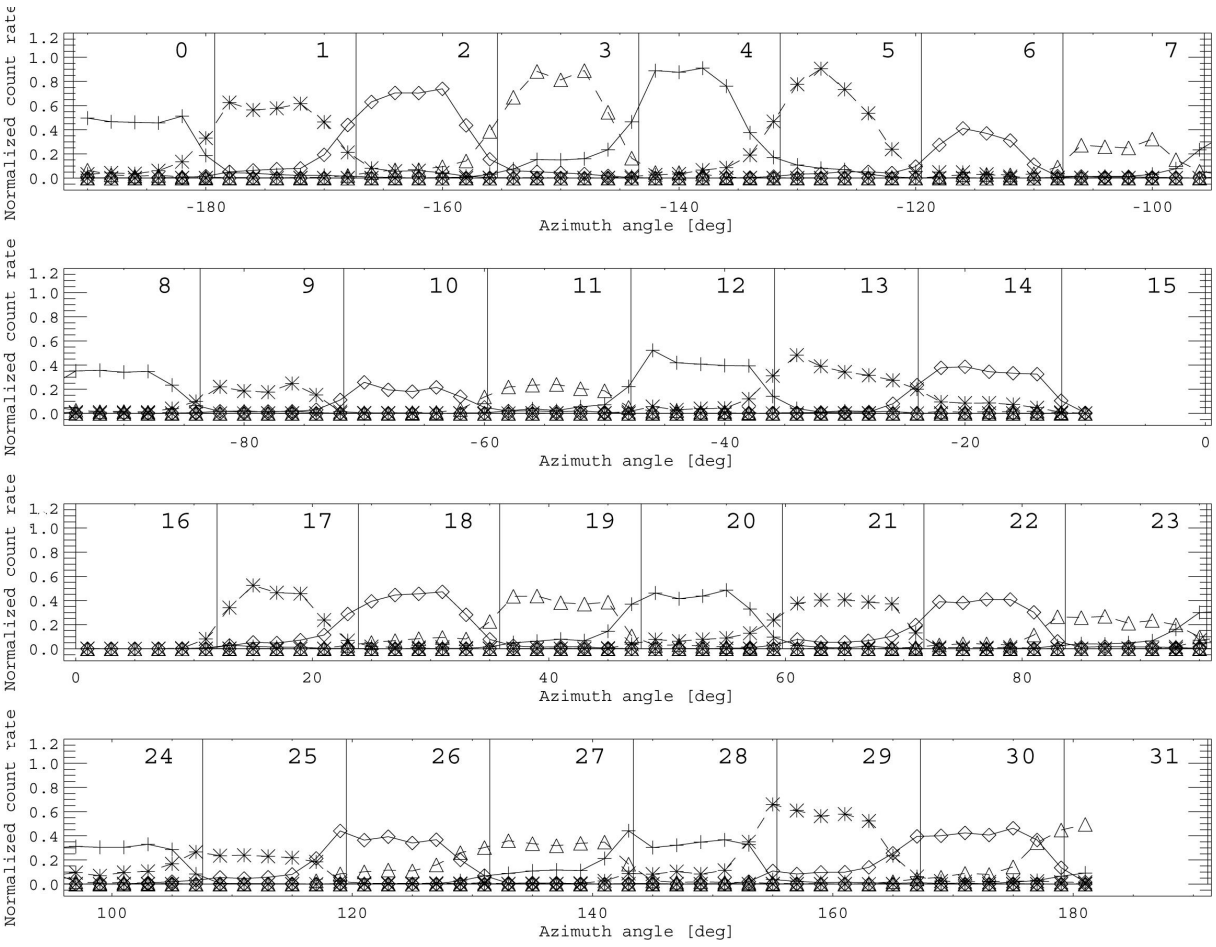


Figure 3.11: 360° azimuth scan of normalized sector response. The sector numbers are displayed. Measurement was made with an MCP bias of 2300 V.

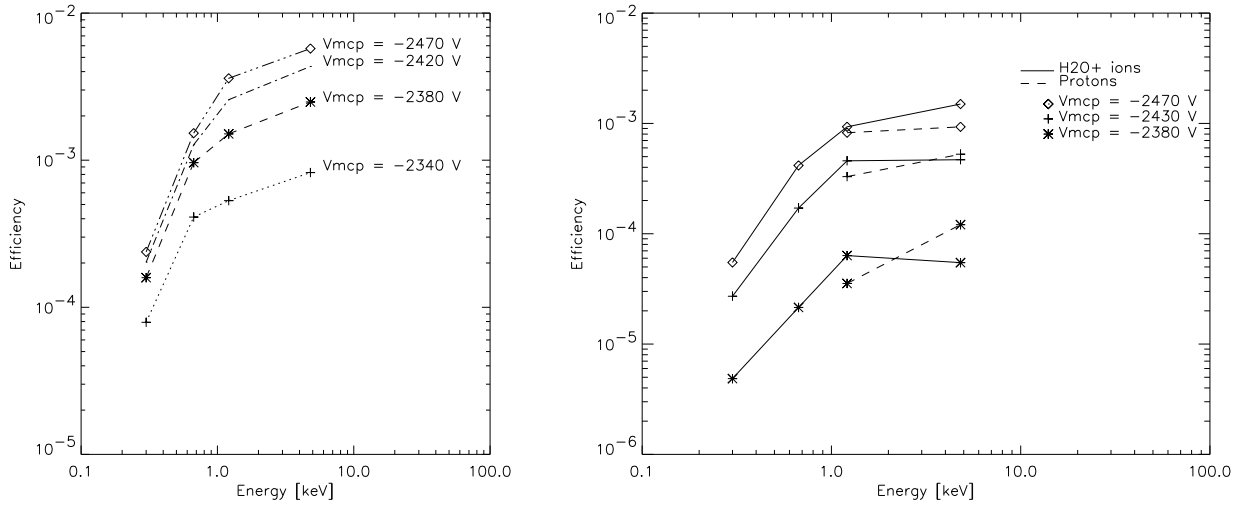


Figure 3.12: (Left) Efficiency using $H_2O^+$ ions with neighboring sectors open. (Right) Efficiency using $H_2O^+$ and $H^+$ ions with neighboring sectors mechanically blocked.

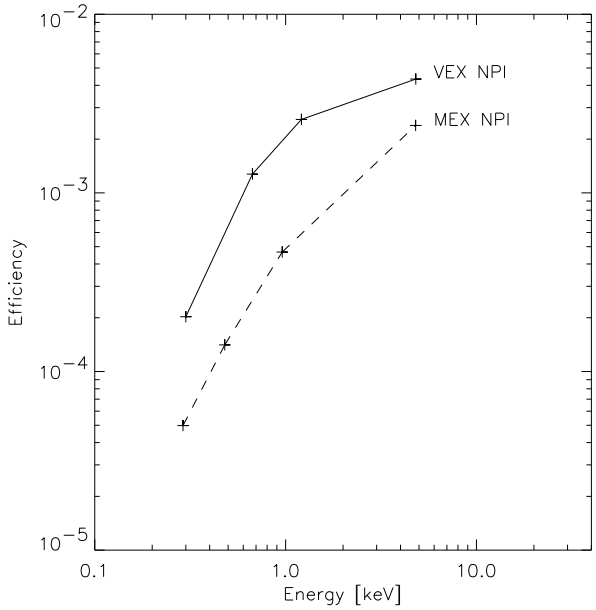


Figure 3.13: Comparison between the ASPERA-3 (MEX) NPI and ASPERA-4 (VEX) NPI efficiencies for nominal MCP bias (2310 V and 2430 V).

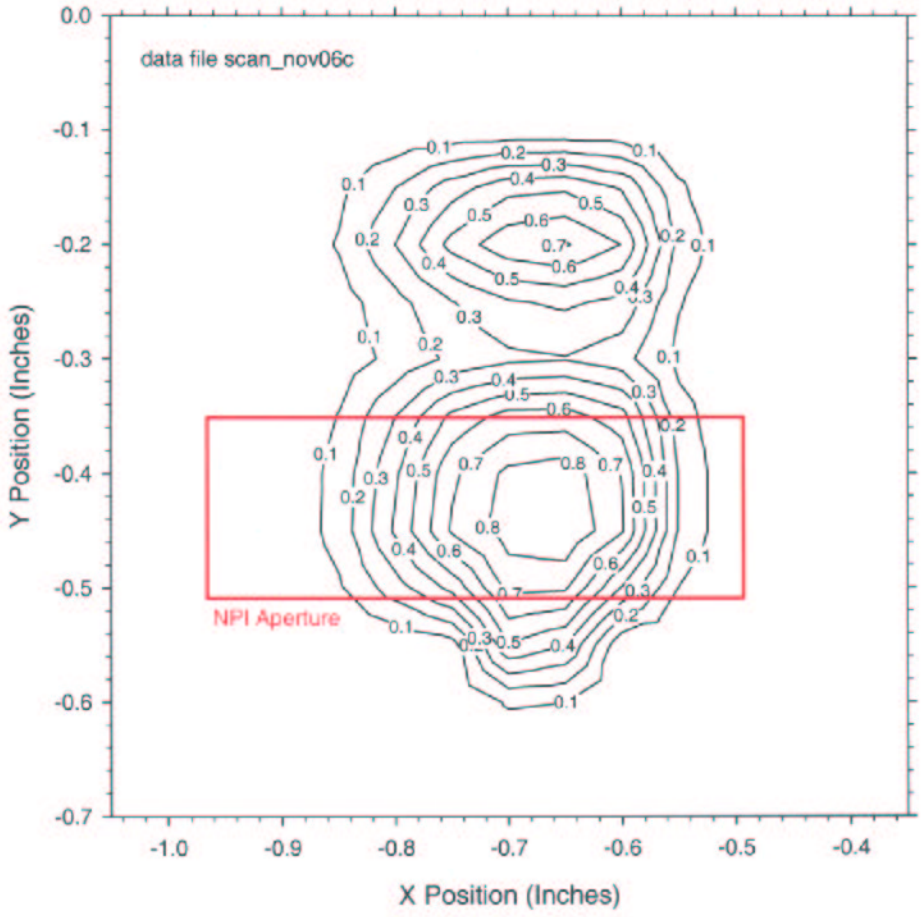


Figure 3.14: The measured beam map with the aperture used during the UV calibration of ASPERA-4 NPI.

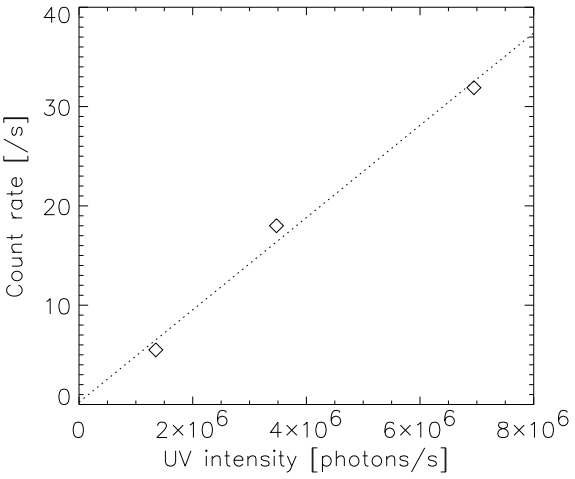


Figure 3.15: NPI count rate versus UV intensity.

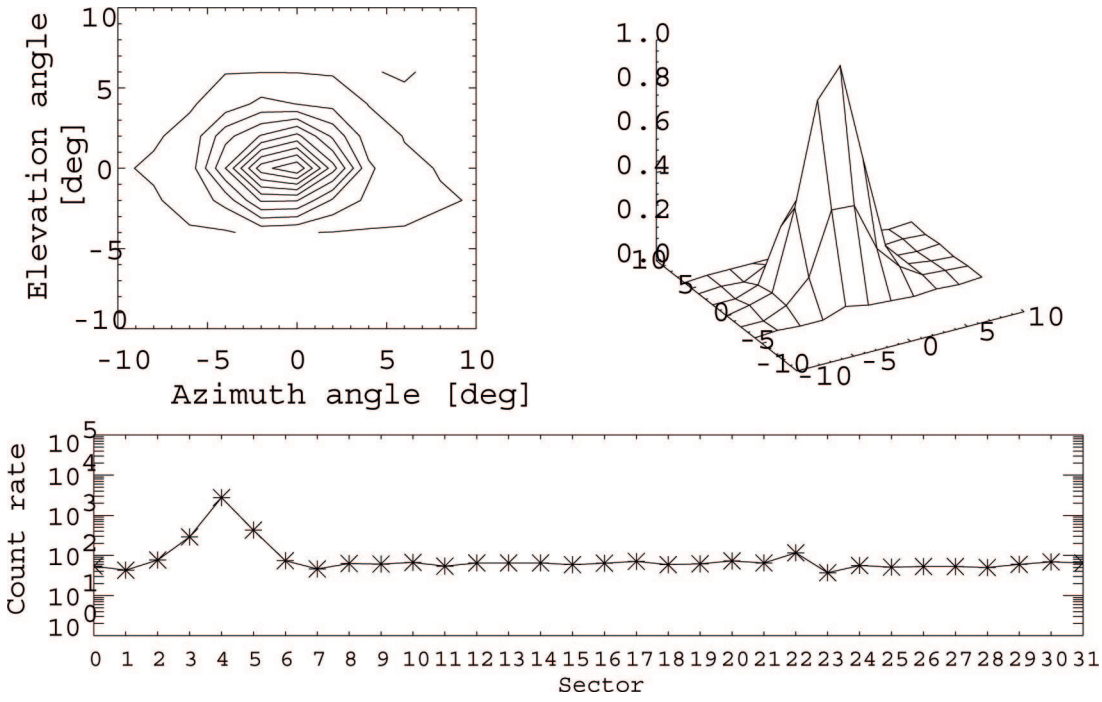


Figure 3.16: Angular scan of sector 4 with the rotation plane coinciding with the sector aperture plane (top). MCP bias was 2430 V. The total count in all NPI sectors during the angular scan shows some response in sectors 3 and 5 indicating internal reflections (bottom).

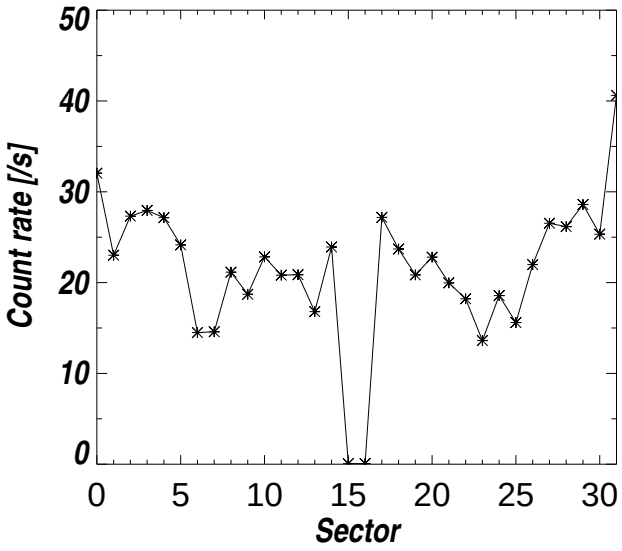


Figure 3.17: Relative sensitivity of all NPI sectors to Lyman-$\alpha$ photons.

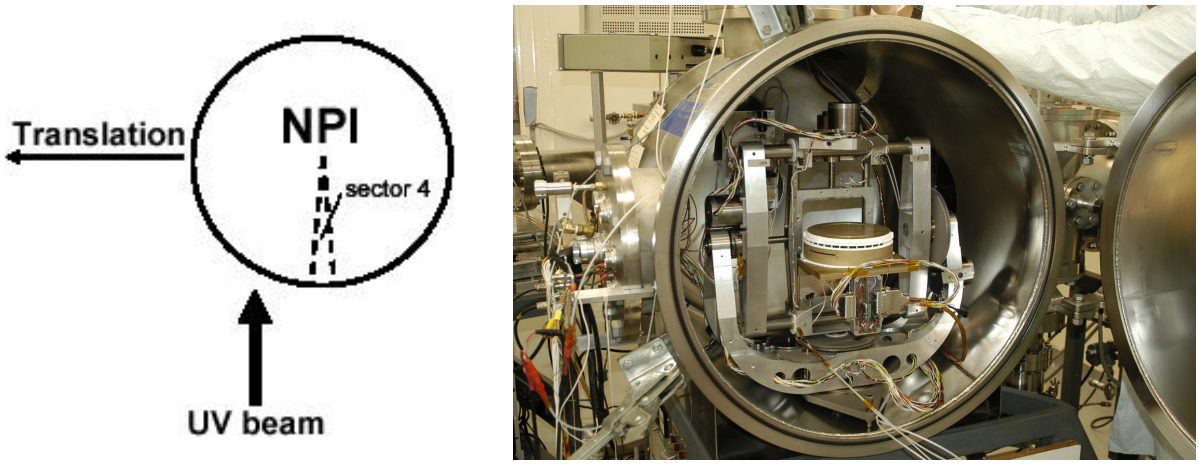


Figure 3.18: Translation measurement set up (left). Sector 4 was directed towards the UV beam and the sensor translated in steps of 3 mm. The NPI inside the photon calibration facility at the Lunar and Planetary Laboratory, University of Arizona, Tucson (right).

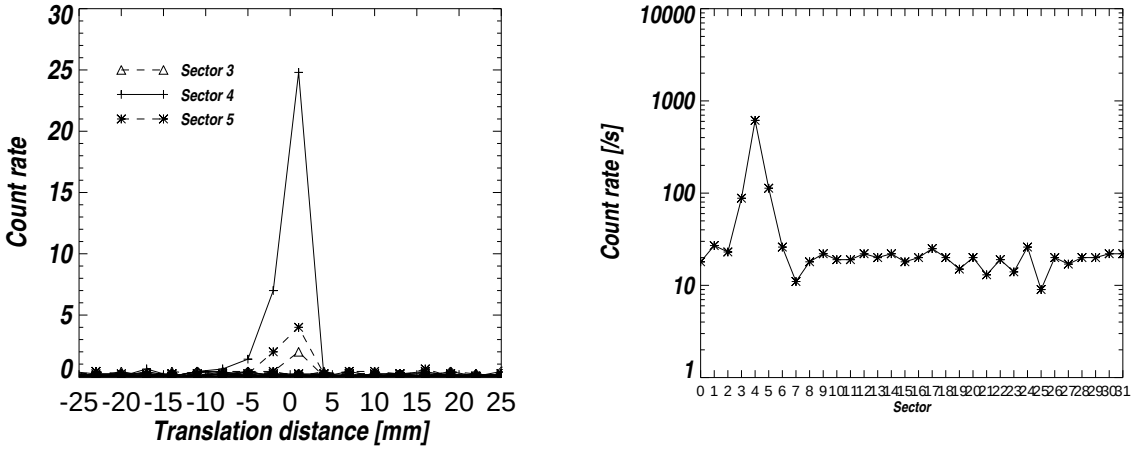


Figure 3.19: Translation measurement with $\Delta x = 3$ mm (left), and total count during translation measurement (right).

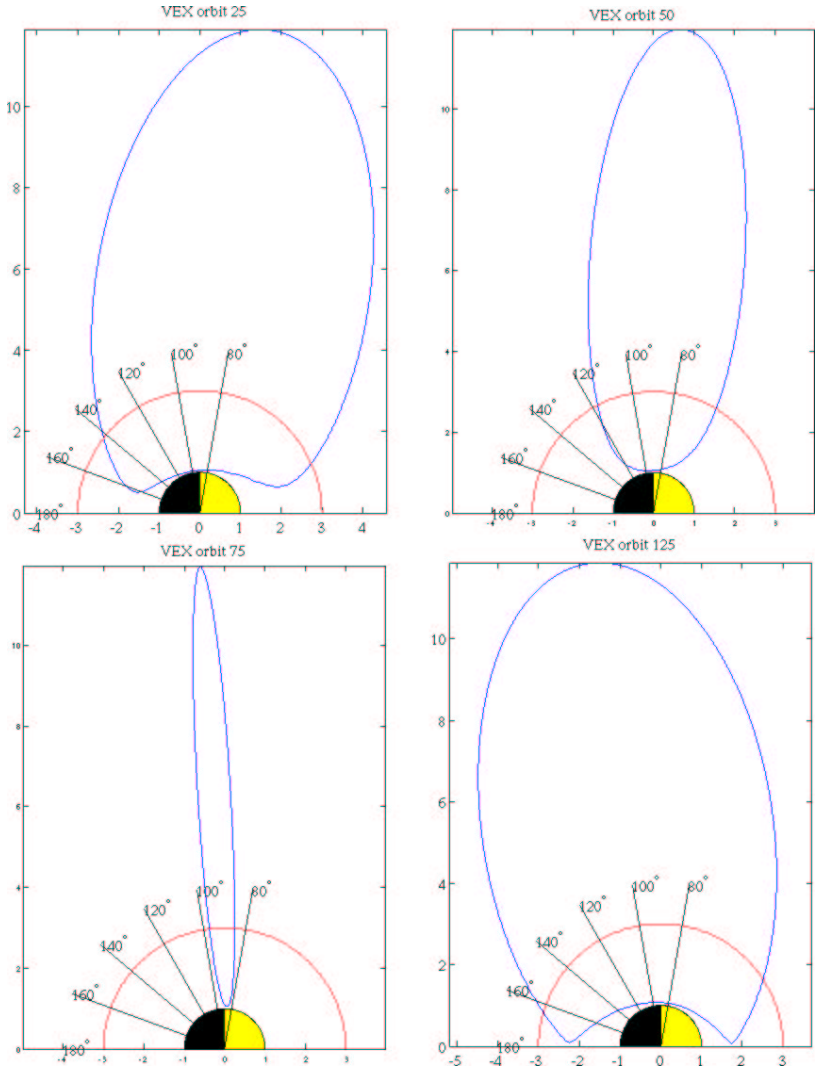


Figure 3.20: The planned Venus Express orbit around Venus. Orbits number 25, 50, 75, and 125 are shown. The coordinate system is a cylindrical representation of a three-dimensional coordinate system, where the origin is in the center of Venus, the $x$-axis is directed toward the sun, the $z$-axis is directed northward, perpendicular to the ecliptic plane, and the $y$-axis closes the right-handed system. The y-axes in the plot is the $(y^2 + z^2)^{1/2}$ which is the distance to the Venus-sun line. The black semi-circle marks a distance of 3 $R_v$ from the center of Venus and the black lines show different SZA.

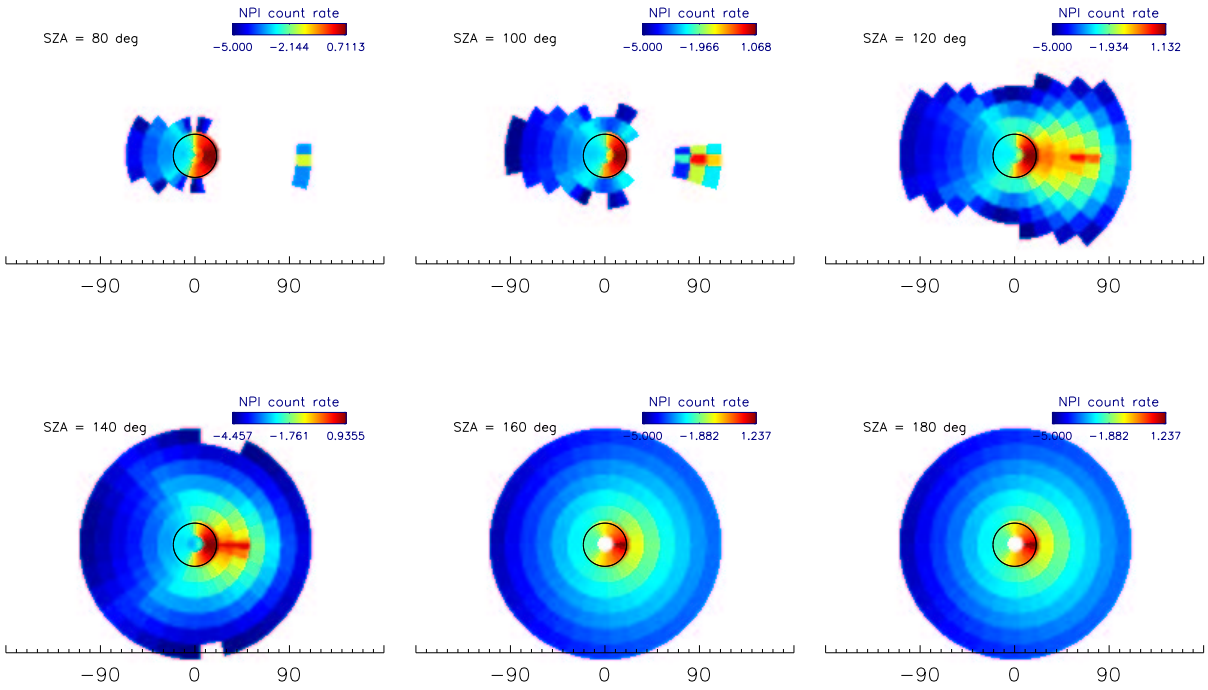


Figure 3.21: Simulated NPI count rates (per second) from ENAs at Venus based on the same model and vantage points as in Fig. 3.3. The scales are different in each image. White color marks count rates below $10^{-5}$ $s^{-1}$.

# Chapter 4

# Earth

*Mid pleasures and palaces though we may roam,*
*Be it ever so humble, there's no place like home.*
- John Howard Payne

*The real voyage of discovery consist not in seeking new landscapes but in having new eyes.*
- Marcel Proust

**The Earth is the third planet, on average 149,6 million km defined as 1 astronomical unit AU, from the sun. It is the only planet in the solar system that we know harbors life. An important factor in this is that it is also the only one in the solar system where water can be present on the surface in liquid form. About 71 % of the Earth's surface is covered with water. The interior of the planet is divided into several layers each presenting different chemical composition and seismic properties. In the center is a solid inner core probably made of iron or a combination of nickel and iron and, possibly, some lighter elements. Surrounding the inner core is a semi-fluid outer core that is responsible for the Earth's magnetic field that typically reach tens of thousand km into space on the dayside and several hundreds of thousand km on the nightside. The core has a radius of 3500 km, which is slightly larger than the radius of the planet Mars. The next 2800 km or so are made up of different layers in the mantle. The crust is about 40 km thick and primarily made of silicon dioxide (quartz). Its thickness varies considerably (thinner under oceans, thicker under continents). The Earth atmosphere consists of 78 % nitrogen and 21 % oxygen. The rest is made up of traces of argon, carbon dioxide and water. The small amount of carbon dioxide is extremely important to maintain the Earth's temperature through the greenhouse effect. Without it, the oceans would freeze and life as we know it would be impossible.**[1]

[1] Reference: Bill Arnett, www.nineplanets.org

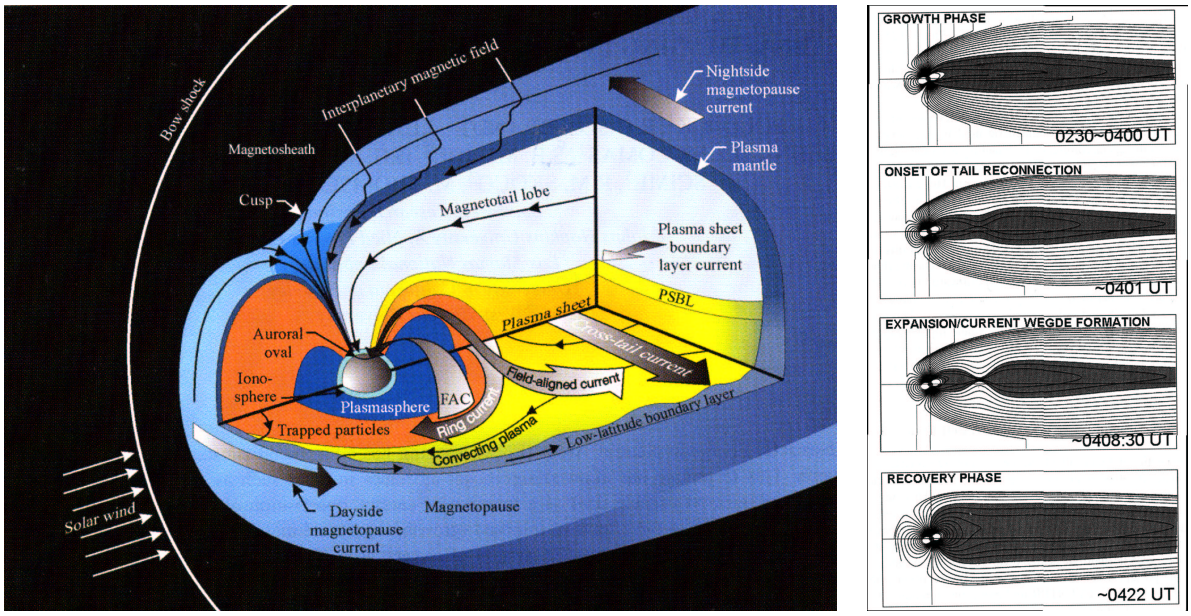


Figure 4.1: A sketch of the accumulated known processes and structures of the Earth's magnetosphere (left) and an illustration of the magnetosphere from a side view that shows the dynamics during a substorm on 27 August, 2001 (left). Note the dipolarization of the near Earth magnetic field in the tail region. Adapted from *Pollock et al.* [2003] and *Baker* [2003].

## 4.1 ENAs at the Earth

The presence of a magnetosphere (Fig. 4.1) makes the structure and energy of ENA emissions from the Earth very different from Mars and Venus. The magnetosphere presents an obstacle to the solar wind flow and a bow shock is formed at a typical distance of 10-18 $R_E$. The Earth is submerged in a gigantic, magnetic bubble with a sunward extension of typically 5-10 $R_E$, while on the nightside the magnetic field lines are stretched out to several 100s $R_E$. The boundary of this magnetospheric bubble is called the magnetopause. Different plasma populations exists within the magnetosphere. The Earth's ring current is a westward current around the Earth at geocentric distances of between 2-6 $R_E$. It is carried by energetic charged particles trapped in the Earth's inner magnetosphere. High energy($> 1$ MeV) populations of the ring current is responsible for the formation of the radiation or Van Allen belts.

The solar wind carries with it an embedded interplanetary magnetic field (IMF) of about $\mathbf{B} \approx 5$ nT at Earth orbit. The direction of the IMF varies with activity on the sun and the interaction of this interplanetary field with the geomagnetic field results in a transfer of energy, momentum, and mass to the magnetosphere. This interaction and changing solar wind conditions can lead to an energization of ion and electron populations within the magnetosphere and its reconfigurations resulting in global disturbances or deviations from the quiet state. Sometimes the disturbances

lasts for several days in what is called a geomagnetic storm. Storms are often triggered by coronal mass ejections from the sun, which are more common during solar maximum (a good account of magnetic storms can be found in [*Tsurutani et al.*, 1997]). Typical magnetospheric storms have three phases; an initial phase when the dynamic pressure of the solar wind increase, a main phase when particles are energized and injected into the inner magnetosphere where they contribute to the ring current (see below), and a recovery phase when the energized particles are lost in charge exchange processes and interaction with the plasmasphere [*McPherron*, 1997]. A magnetospheric substorm developes when energy accumulated in the magnetotail are suddenly released and dipolarization of the stretched magnetic field lines in the magnetotail causes sunward acceleration of the plasmasheet charged particles and their injection towards the nightside of the planet. The ring current immersed in the extentended hydrogen exosphere is the main source of ENAs in the Earth magnetopshere.

Naturally, ENA observations at Earth have evolved further than elsewhere in the solar system and have truly become a useful tool for imaging and understanding processes in the storm time magnetosphere. The IMAGE mission [*Burch*, 2000] has played an important part in this evolution with three ENA imagers on-board that image ENAs in different energy intervals (the LENA, MENA, and HENA instruments are briefly described in Section 1.2.1). Before the IMAGE spacecraft the first dedicated ENA instrument in orbit, Prelude In Planetary Particle Imaging (PIPPI) [*Barabash et al.*, 1998] on the Astrid microsatellite [*Norberg et al.*, 1995], made ENA measurements from a low polar orbit (1000 km). It confirmed some of the predicted phenomena such as the dusk-dawn asymmetry [*Barabash et al.*, 1997; *Brandt et al.*, 2001a].

*Brandt et al.* [2001a] showed measurements of high energy (26-37 keV hydrogen and 46-64 keV oxygen) ENAs with the PIPPI instrument (Fig. 4.2). The observations were of ENAs from mirroring ions charge exchanging with the upper atmosphere in the pre-midnight sector on auroral latitudes (L shells $L = 4-8$). The measurements were compared to an ENA model based on a six element (H, He, N, O, $N_2$, and $0_2$) neutral Chamberlain model with properties derived from the Mass Spectrometer Incoherent Scattering Extended (MSISE-90) model [*Hedin*, 1991] and a parameterized model of the ion distribution in the equatorial ring current. Both $H^+$ and $O^+$ were considered. Through forward modeling, minimizing the difference of the results by varying parameters of the model, they concluded that a significant part of the measurements are a result of oxygen precipitation on the upper atmosphere at the considered latitudes. The measurements also showed a dawn-dusk asymmetry that is consistent with an asymmetric ring current due to the E×B drift from the midnight sector toward the dusk side.

Another ENA population visible from low altitudes are up-flowing ENAs from the polar cap. *Brandt et al.* [2001b] report ENA emissions (of intensity $\leq 10^6$ $cm^{-2}$ $sr^{-1}$ $s^{-1}$) from magnetic latitudes $70° - 85°$ (emission altitude 400 km assumed) of energies $\leq$ 13 keV for hydrogen and $\leq$ 46 keV for oxygen (Fig. 4.3). Two sources are suggested; (1) up-flowing ions that charge exchange at the exobase and (2) backscattered ENAs from precipitating ions that undergo several charge exchange and stripping transitions as they reach lower altitudes and are reflected through backscattering (ENA albedo). Comparison of the estimated ion flux in source (1) above required to produce the observed emissions showed that such intensities are indeed possible and can explain the ENA emissions alone. ENA albedo was not expected at the observation latitudes. *Brandt et al.* [2001b] conclude that ENA outflow in the polar region is an important atmospheric escape

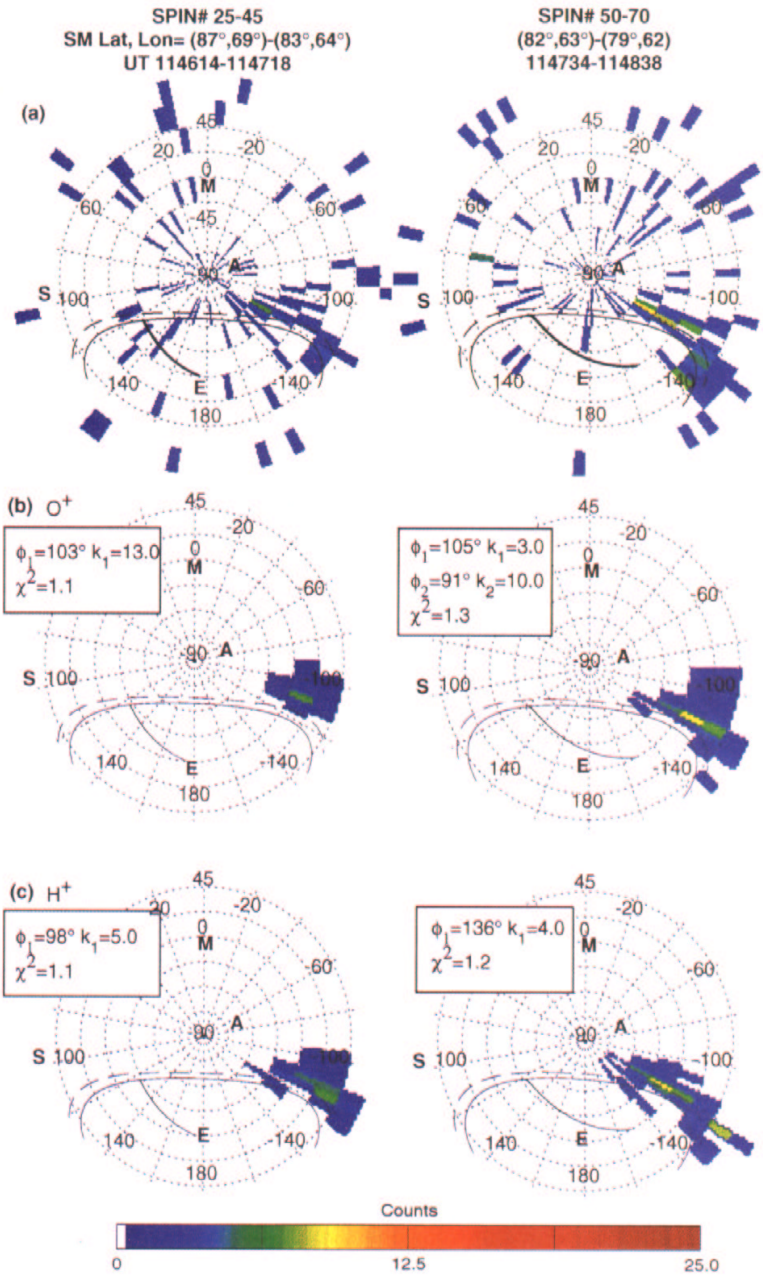


Figure 4.2: Observed and simulated ENA images accumulated during one minute for two different vantage points during a satellite pass over the polar cap. (a) is the observed image, (b) a simulation of oxygen ENAs, and (c) a simulation of hydrogen ENAs. The images are in a fish-eye view where 90° denotes the spin axis of the satellite. The thin solid line is the Earth's limb and the thick solid line is the terminator. The letters S, E, and A indicates the solar, nadir, and anti-sunward direction respectively. From *Brandt et al.* [2001a].

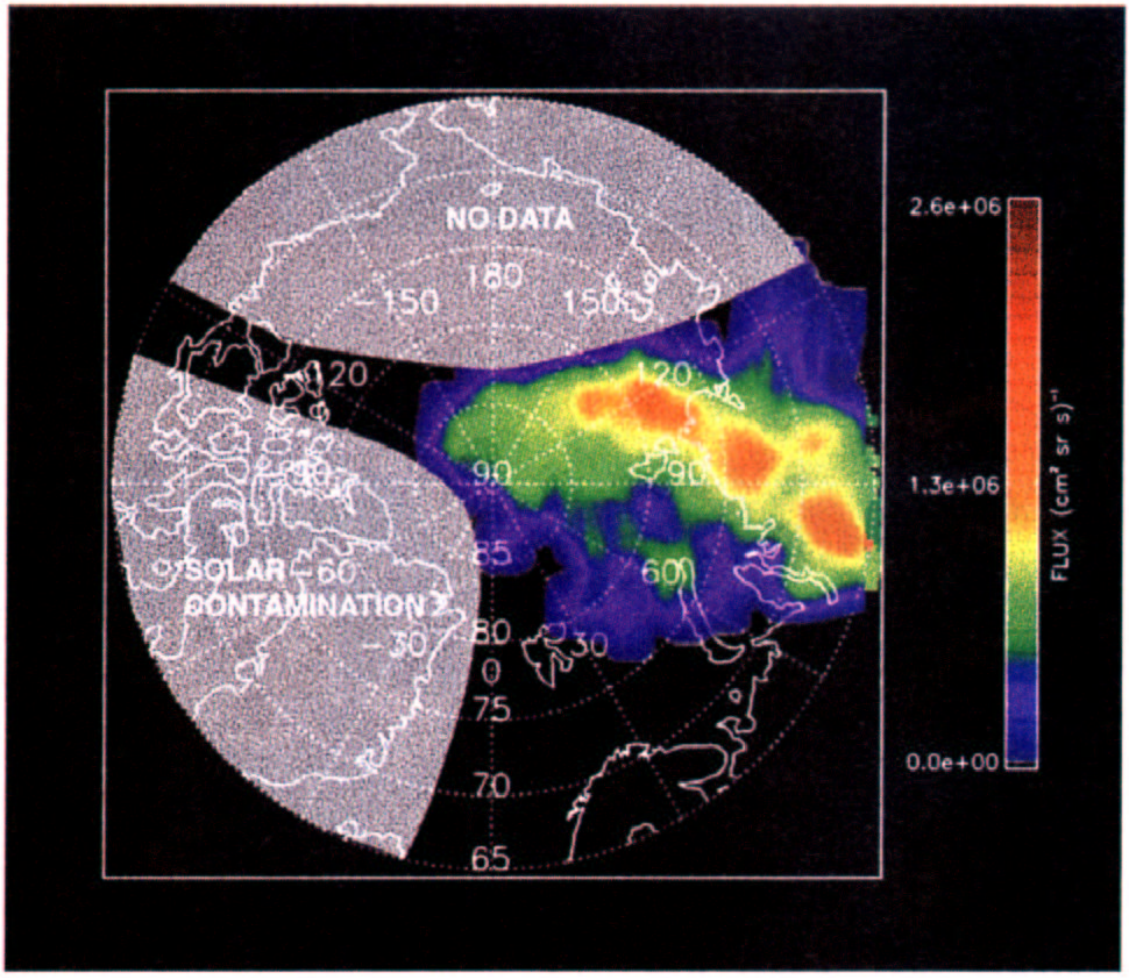


Figure 4.3: Average of ENA images during $\approx$ 10 min minus a three-counts background. Total low altitude ENA outflow is estimated to $\leq 10^{27}$ $s^{-1}$ and the peak flux is $10^6$ $cm^{-2}$ $sr^{-1}$ $s^{-1}$. From *Brandt et al.* [2001b].

mechanism.

The ENA instruments on the IMAGE spacecraft have made several observations of the ENAs from the inner magnetosphere during substorms [*Burch et al.*, 2001; *Brandt et al.*, 2002a; *Mitchell et al.*, 2003; *Pollock et al.*, 2003]. The typical substorm MENA/HENA observation of ENAs (Fig. 4.4) start with an increased intensity in the midnight sector. In the late main stage and recovery phase of the substorm the low energy (< 10 keV) ENA emissions stay close to the midnight sector with some diffusion toward the dawn and dusk regions, while higher energy (16-27 keV) emissions drift around the Earth toward dusk and the even higher energy (39-60 keV) emissions reach the afternoon sector on the dayside [*Pollock et al.*, 2003].

From a constrained linear inversion method [*Brandt et al.*, 2002a; *Demajistre et al.*, 2004] and subsequent comparisons with a parameterized ion distribution model (such as that presented in *Roelof and Skinner* [2000]) a parent ion distribution in the equatorial ring current can be extracted from high altitude ENA images. The linear constrained inversion method was used in *Brandt et al.* [2002a] to study global energetic ion distribution in the plasma sheet (out to $R_E = 14$) from inverted ENA images during two substorms in the main phase of the October 4, 2000 storm. Fig. 4.5 shows the ENA emissions in the 10-60 keV energy range of the second substorms sequence with auroral onset at 9:22 UT (the small inserted images of the auroral oval comes from the FUV instrument [*Mende et al.*, 2000]). There is a clear intensity decrease of ENA emissions in the $L > 8$ region after 9:32 UT, while the nightside emissions increase with time in $L \leq 4$. Inversion of the ENA images showed that also the parent proton distribution in the plasma sheet moves earthward as the magnetic field is dipolarized (correlated with magnetic field measurements on the GOES satellite at geosynchronous orbit). It is pointed out that there are uncertainties involved in the inversion of the images in particular the assumption of a dipole magnetic field, which tend to attribute the ENA emissions to protons trapped in L-shells closer to the Earth than they may be in reality with a slightly stretched magnetosphere (Fig. 4.6) (a magnetic L-shell is defined as the distance, in Earth radii, from the center of the Earth to where the magnetic field lines cross the equatorial plane. $L = 4$ crosses the equatorial plane at a geocentric distance of 4 $R_E$ for example). This is particularly is a problem for retrieving ion densities from high L-values. Nevertheless, such observations combined with the inversion process opens the possibility to globally image the proton plasma and use ENA imaging as a true diagnostic of other processes in the magnetosphere. An early example is *Roelof* [1989], where ion pressures and pressure driven electric currents in the inner magnetosphere are derived from the first ENA image [*Roelof*, 1987]. Another example of ENA image analysis using linear inversion is *Brandt et al.* [2002b], where statistics of ring current ion distributions derived from inverted ENA images during 18 periods of prolonged southward IMF $B_z$ component (i.e. during storm main phase) between the years 2000 and 2002 are presented and correlated with the IMF $B_y$ component and solar wind velocity.

*Mitchell et al.* [2003] investigated high energy (52-180 keV) oxygen ENAs during the 21 October 2001 and 6 November 2001 storms. They found that the oxygen ENA signatures differs from the hydrogen ENAs in that the oxygen ENAs are much more concentrated to low altitudes near the planet. Because of poor angular resolution for oxygen ENAs they cannot for certain conclude to which extent the measured ENAs are a result of ionospheric loss or if there are fresh injections of $O^+$ from the equatorial ring current resupplying the emission region. In the case for ionospheric loss the

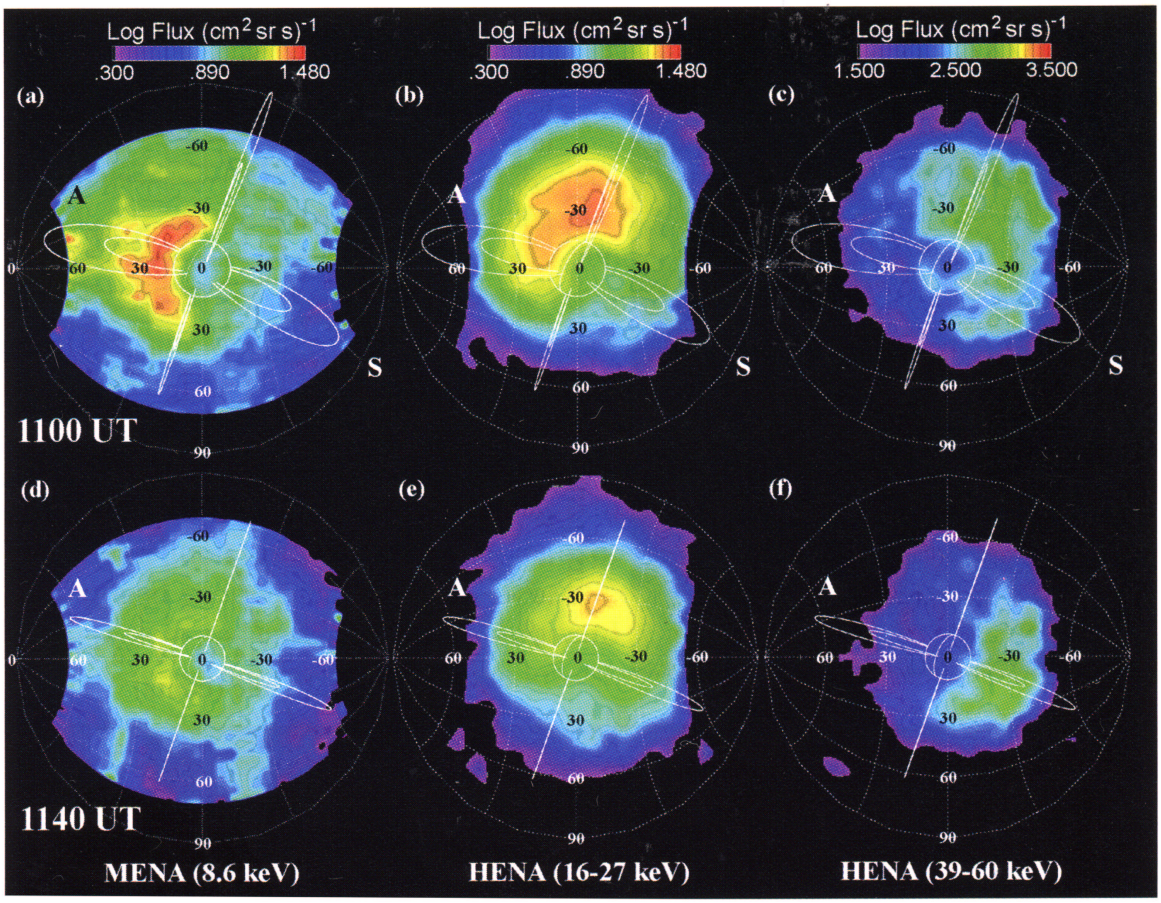


Figure 4.4: ENA images from the later stage and recovery phase of a substorm measured by the MENA and HENA instruments. The two rows are separated 40 minutes in time and the three columns show different ENA energy ranges. Magnetic L-shells $L = 4$ and $L = 8$ are indicated with white lines in the noon, midnight, dawn, and dusk directions. 'S' indicate the noon direction. From [*Pollock et al.*, 2003].

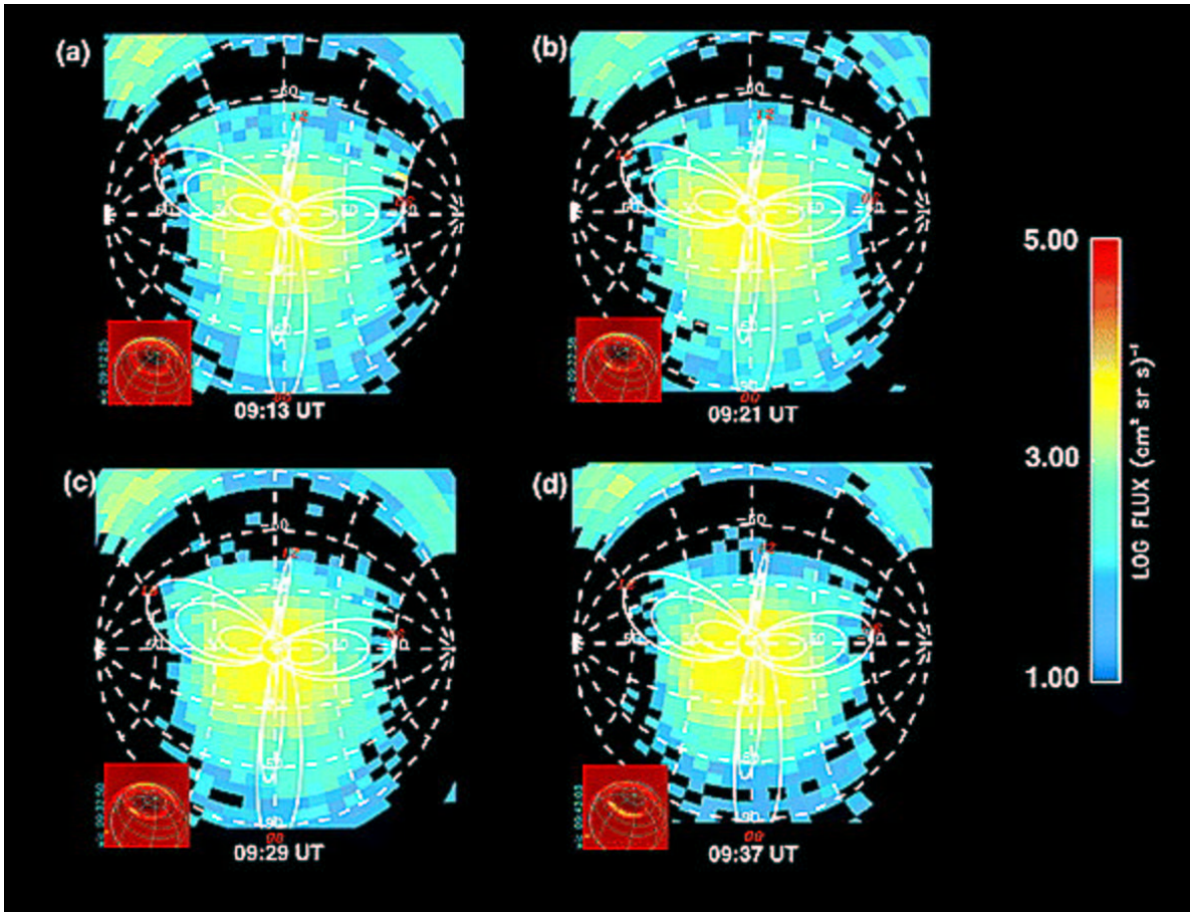


Figure 4.5: An ENA image sequence in the 10-60 keV range of the substorm with auroral onset at 9:22 UT. Magnetic L-shells $L = 4$ and $L = 8$ are indicated with white lines in the noon, midnight, dawn, and dusk directions. The inserted red images are auroral images from the FUV camera on IMAGE. From *Brandt et al.* [2002a].

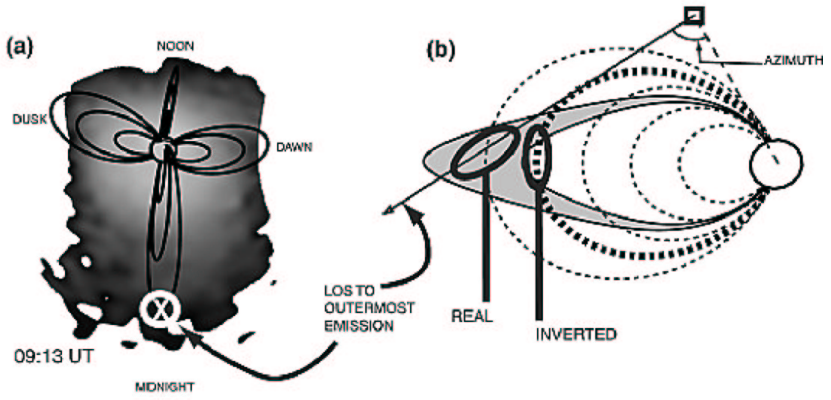


Figure 4.6: The effect of using a dipole magnetic field model in the linear inversions of ENA images at lines of sight that transverse high altitude regions is that the radial location of the outer edge of the equatorial ion distribution is underestimated. (a) shows a typical ENA image with a line of sight through an outer region marked. (b) Solid lines represent a stretched magnetic field and the dashed lines the dipolar model. The inverted ENA image will associate the parent ion distribution with a lower radial altitude.

problem is that such oxygen ions would have to undergo a massive energization to be measured as ENAs in the 52-180 keV HENA energy range. However, simulations have shown that combining the acceleration processes involved in E×B drift and convection to ring current altitudes with a rapid (one minute) dipolarization of the magnetic field oxygen ions may be accelerated to several 100s keV [*Delcourt*, 2002], which is consistent with the observations. Dipolarization during the onset of auroral substorms was observed by *Brandt et al.* [2002a].

The LENA instrument has investigated low energy ($<$ 1 keV) ENA emissions. Initial results showed that LENA is able to measure the neutral component in the solar wind from inside the magnetosphere [*Collier et al.*, 2001]. During southward turning of the IMF $B_z$ component a higher neutral solar wind intensity was observed, which is explained by the magnetopause moving inward allowing the solar wind to penetrate closer to the Earth and higher densities of the exosphere, thus increasing the ENA production from charge exchange [*Collier et al.*, 2005]. LENA has also observed ENAs from the magnetosheath during extreme solar wind conditions and associated magnetopause motion [*Moore et al.*, 2003; *Taguchi et al.*, 2004]. Comparing the results with a model based on ion flux in the sheath and the hydrogen density in the exosphere indicates that the polar magnetic cusp motion can be monitored using LENA ENA images during both disturbed and quiet magnetosphere conditions [*Taguchi et al.*, 2004].

Table 4.1: List of scientific instruments included in the Double Star mission.

| **Instrument** | | **TC-1** | **TC-2** |
|---|---|---|---|
| Flux Gate Magnetometer | (FGM) | √ | √ |
| Hot Ion Analyzer | (HIA) | √ | – |
| High Energy Electron Detector | (HEED) | √ | √ |
| High Energy Proton Detector | (HEPD) | √ | √ |
| Heavy Ion Detector | (HID) | √ | √ |
| Active Spacecraft Potential Control | (ASPOC) | √ | – |
| Plasma Electron And Current Experiment | (PEACE) | √ | √ |
| Spatio–Temporal Analysis of Field Fluctuations/ Digital Wave Processor | (STAFF/DWP) | √ | – |
| Low Energy Ion Detector | (LEID) | – | √ |
| Low Frequency Electromagnetic Wave detector | (LFEW) | – | √ |
| Neutral Atom Detector Unit | (NUADU) | – | √ |

## 4.2 The Double Star mission and the Neutral Atom Detector Unit (NUADU)

The Chinese Double star mission consists of the two spacecraft TC-1 and TC-2. TC-1 was launched in an equatorial orbit (perigee × apogee = 570 × 78970 km, inclination 28.5°) in December 2003 and TC-2 in a polar orbit (682 × 38279 km, inclination 90.1°) in July 2004. The mission was designed to study the coupling between processes in the equatorial inner magnetosphere and the associated responses in the polar regions. The scientific payload of the two spacecraft consists of both Chinese and European instruments. The European instrumentation consists to a large extent of duplicates or spare models of the CLUSTER II mission [*Escoubet et al.*, 1997]. A main driver for the mission from a European point of view was that the two Double Star satellites with its duplicate instrumentation would function as additional fifth and sixth measurement points added to the four satellites comprising the CLUSTER II mission. Table 4.1 lists the instruments on the TC-1 and TC-2 spacecraft.

TC-1 and TC-2 are both cylindrical, spin-stabilized satellites of diameter 2.1 m and height 1.23 m. The total mass of each satellite was 330 kg at launch, of which 30 kg was payload mass. The spin rate is 15 rpm and the nominal spin axis was perpendicular to the ecliptic plane for both satellites. The designed life time of the spacecraft was 18 months for TC-1 and 12 months for TC-2. TC-2 encountered early problems believed to have been caused by a major magnetospheric storm in the end of July 2004 shortly after launch. Both the main and redundant computers of the satellite attitude control system failed. Both attitude computers have also failed on the TC-1 spacecraft. As a result the slow natural drift of the satellites' spin axes cannot be corrected. The attitude is now derived from magnetometer data at each perigee pass. The drift of the spin axes is about 0.9°/month on TC-1 and about 1.5°/month on TC-2. According to predictions of the evolution of

the drift made by the satellite manufacturer (Chinese Academy of Space Technology, CAST) the TC-1 spin axis will reach 9° and TC-2 spin axis 30° by July 2006. Nevertheless, all instruments are still operating nominally and a mission extension until the end of 2006 has been approved.

The Neutral Atom Detection Unit (NUADU) [*McKenna-Lawlor et al.*, 2004] is an exception to the European part of the Double Star payload in that it is not a duplicate or spare instrument from the CLUSTER II mission and it flies only on-board the polar TC-2 satellite. NUADU measures ENAs in the energy range between 20-300 keV. The NUADU scientific objectives are:

- to define the morphology of the ring current under different magnetospheric conditions and, thereby, characterize the inner magnetosphere;
- to study particle energization processes in the inner magnetosphere and image plasma convection and sub-storm injections;
- to monitor the ring current and define space weather conditions;
- to study the interaction of the ring current with the upper atmosphere;
- to investigate the inter-relationship between the ring current and the electric field of the inner magnetosphere;

Multi-point studies with other ENA imagers have also been foreseen. An example of collaborative studies with the HENA instrument on IMAGE and NUADU simultaneously imaging ENAs from the ring current from vantage points over the North and South poles are presented in Section 4.5.2. Multi-point ENA images can drastically improve the accuracy of the ENA image inversion, especially in what concerns constraining pitch-angle distributions. NUADU is particularly suitable for this task because of the high angular resolution.

## 4.3 NUADU design

The NUADU design is based on the very simple PIPPI-SSD sensor concept [*Barabash et al.*, 1998], in which viewing sectors are arranged in a fan geometry. Each sector has its own SSD. The instantaneous coverage over polar angle is 180° and the full $4\pi$ solid angle coverage is achieved over one spacecraft spin. The main NUADU design driver was to increase the PIPPI-SSD geometrical factor per pixel 10 times (7 times was achieved) and improve angular resolution. Table 4.2 lists the NUADU properties. NUADU is made up of a cylindrical sensor head and an electronics box (Fig. 4.7). Fig. 4.8 shows NUADU's accommodation on the TC-2 spacecraft. The sensor head of NUADU (Fig. 4.9) has on the inside of one half-cylinder 16 SSDs in four levels. On the other half of the cylinder are 16 apertures (each aperture is $46.5 \times 10$ mm) in four levels, each aperture corresponding to one detector. The four levels are separated with electrostatic deflection plates in the for of discs that remove singly charged particles up to energies of $\approx 300$ keV. The full angular coverage of each NUADU sector is $5° \times 15°$ and they overlap such that the FWHM angular resolution is $5° \times 11.25°$ and the 16 sectors cover 180° in one plane in space (Fig. 4.10). NUADU covers the full $4\pi$ for one spacecraft period (4 s). The sampling time 31.25 ms thus corresponds to

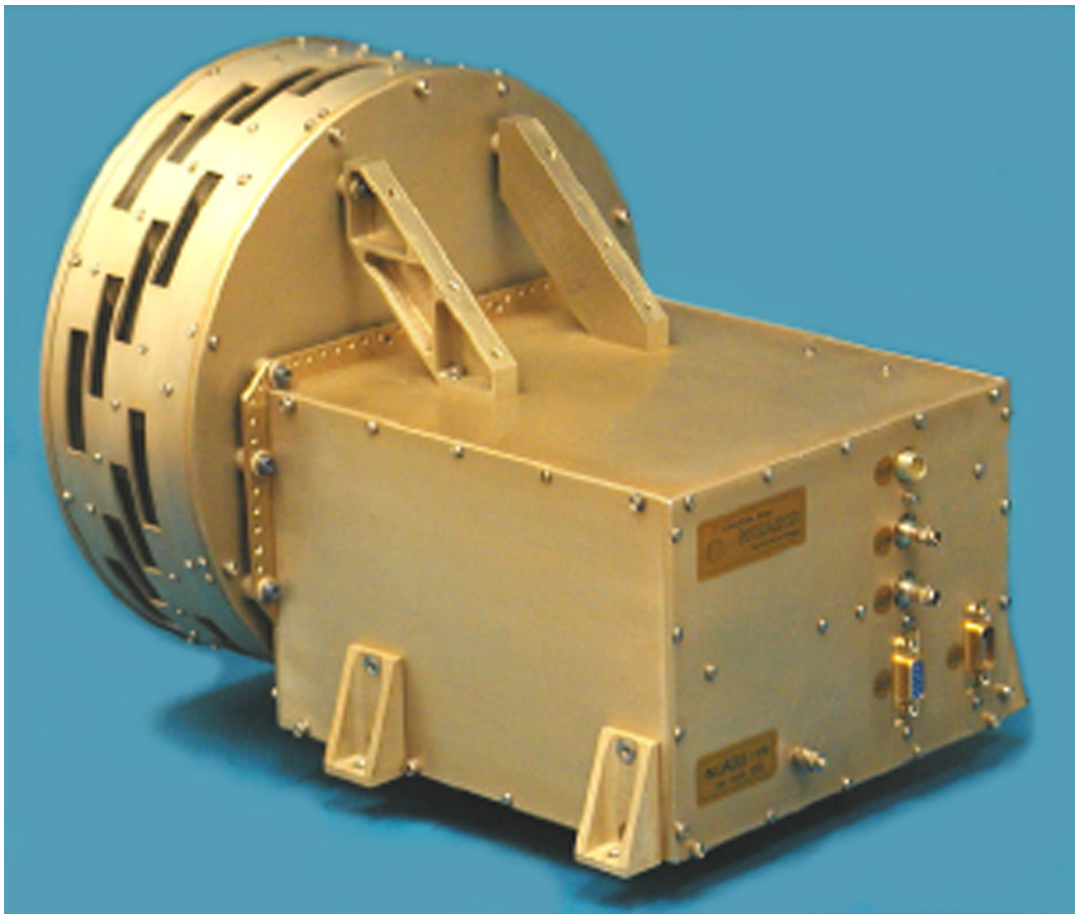

Figure 4.7: The NUADU instrument consisting of a cylindrical sensor head mounted on an electronics box.

Table 4.2: Summary of NUADU properties.

| **Parameter** | **NUADU** |
|---|---|
| Particles to be measured | ENA |
| Energy, keV per charge | $\approx$ 20-300 |
| Energy resolution, $\Delta E/E$ | 8 % (H), 28 % (O) |
| Mass resolution | -* |
| Intrinsic field of view | $5° \times 180°$ |
| Angular resolution, FWHM | $2.5° \times 11.25°$ |
| G-factor/pixel, cm$^2$ sr | $1.23 \cdot 10^{-2}$ |
| Efficiency, % | $\sim$ 100 |
| Time resolution (full 3D), s | 4 (one spin) |
| Sampling time (min), ms | 31.25 |
| Mass, kg | 4.5 |
| Power, W | 4.0 (including heater) |

* See text.

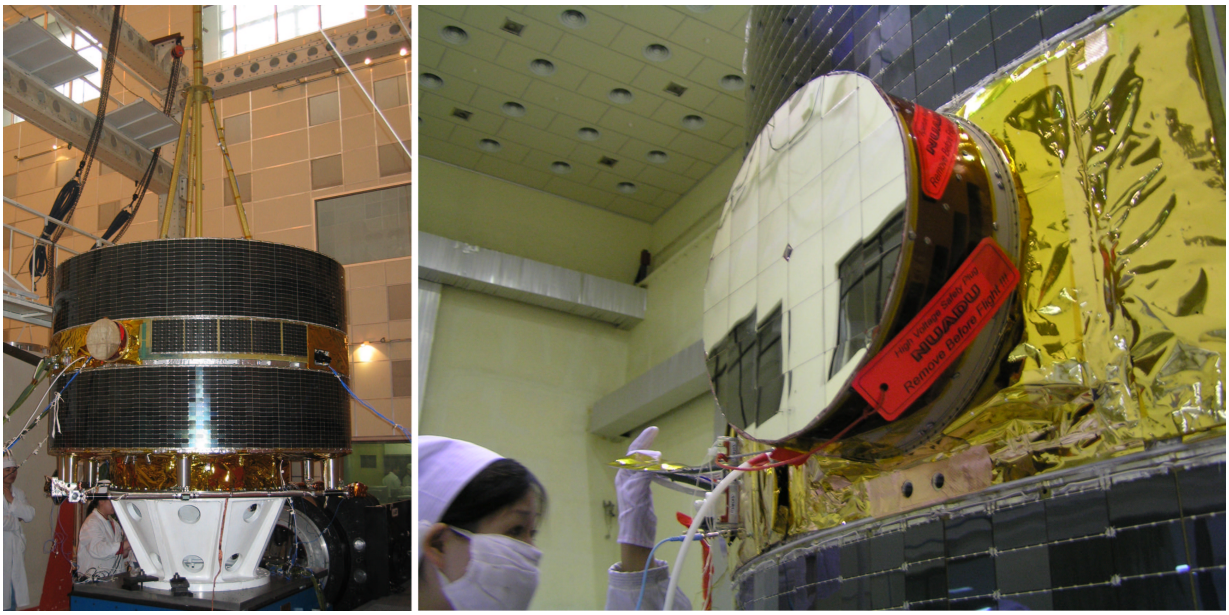


Figure 4.8: NUADU mounted on the TC-2 spacecraft. As the spacecraft rotates the NUADU sectors will cover the complete $4\pi$ sky.

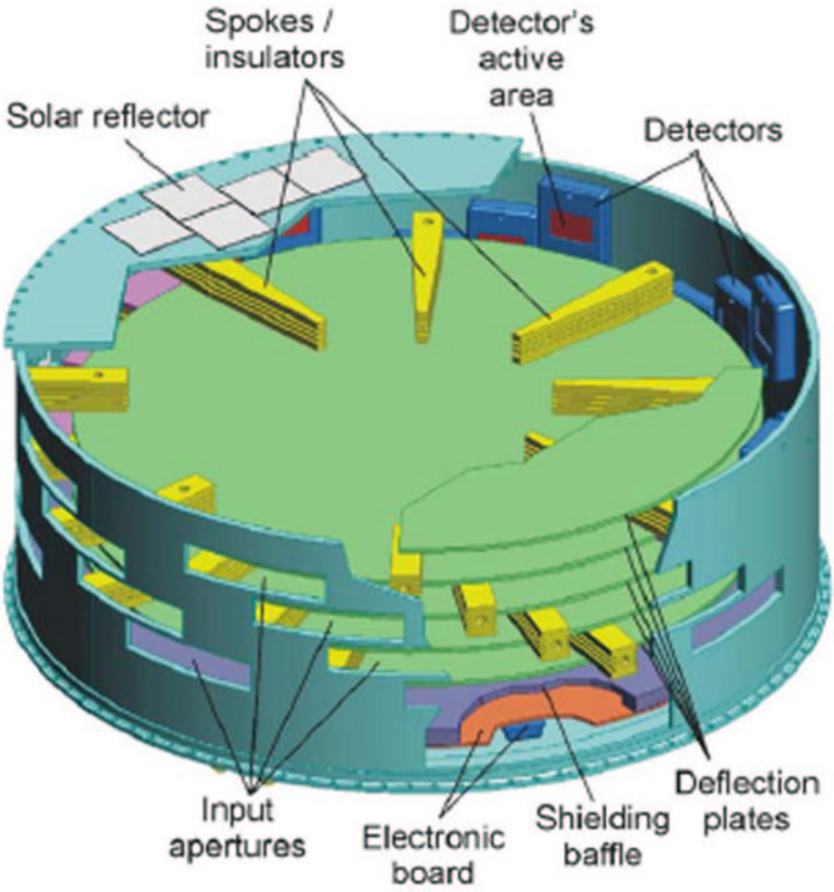


Figure 4.9: Cut-away view of the NUADU sensor head.

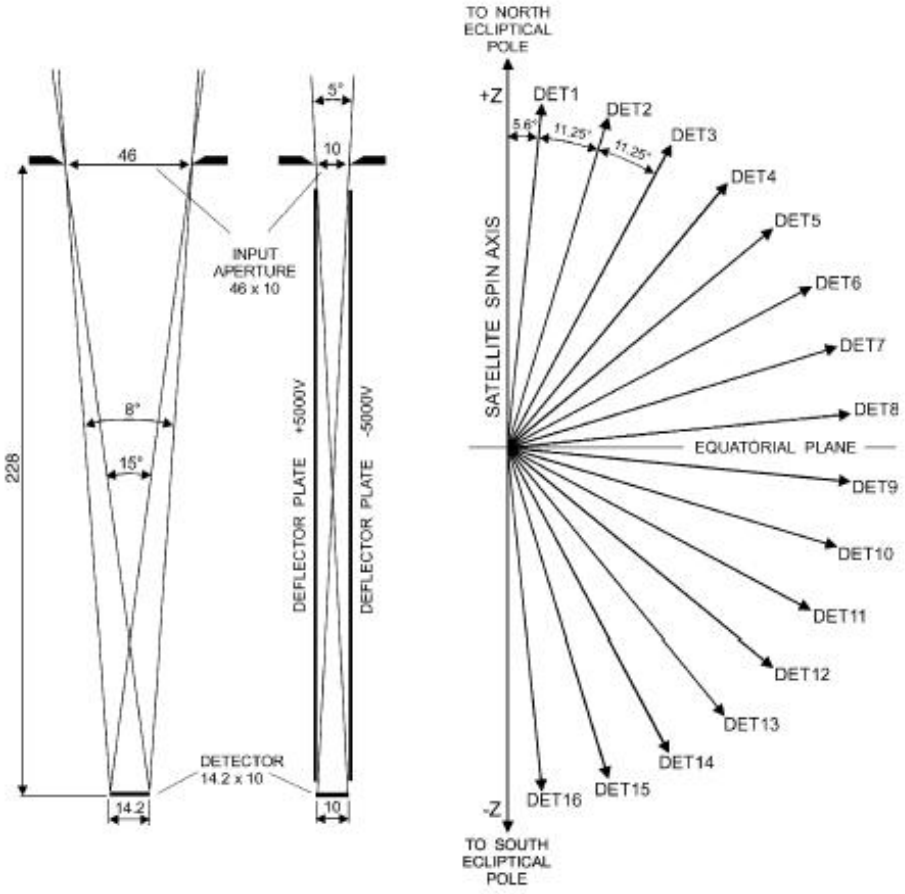


Figure 4.10: Field of view of the NUADU sectors.

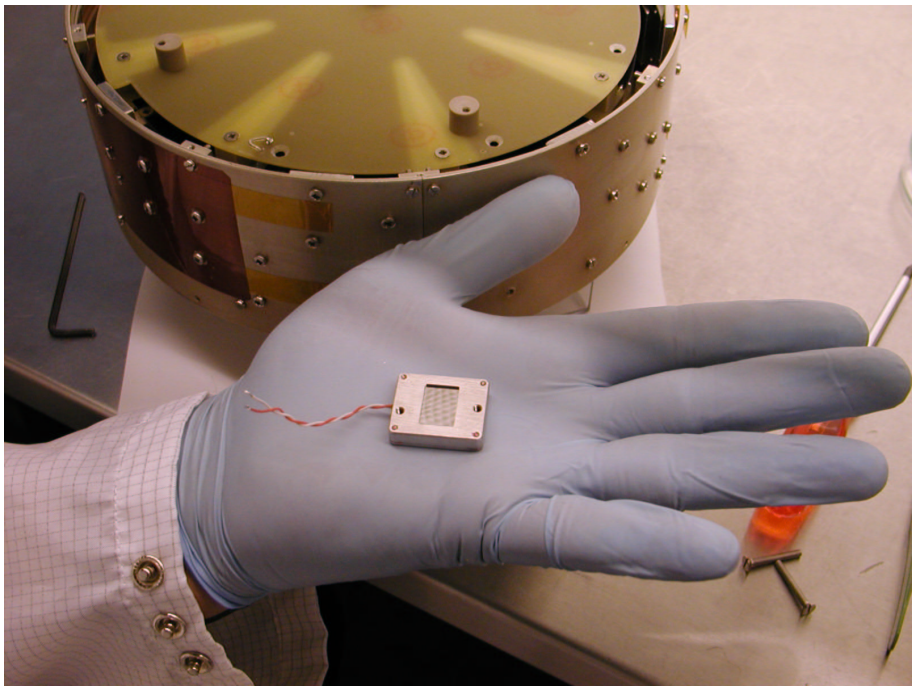

Figure 4.11: The passivated implanted planar silicon SSD with the NUADU qualification model in the background.

an angle of $(360 \times 0.03125)/4 = 11.25°$. The pixel size is $11.25 \times 2.8°$ in a $16 \times 128$ matrix of the entire $4\pi$ solid angle that NUADU measures on each spacecraft spin. To increase the accumulation time there is a possibility to integrate images over several spins in the NUADU DPU.

The detectors in the sensor head are custom designed passivated implanted planar silicon (PIPS) detectors (Fig. 4.11). The contacts in the detectors are implanted rather than traditional surface barrier contacts, which makes them more rugged and reliable. The thickness of the active region in the detectors is 300 $\mu$m and they are fully depleted in order to extend their energy range. The active area of one detector is 14.2 mm $\times$10 mm, and is encapsulated in a stainless steel casing. To block photons and make the detectors 'light tight' there is a $(140 \pm 10)$ nm thick layer of aluminum deposited over the active area on each detector. The detector dead layer is $\approx 45$ nm.

Between the apertures and the detectors there is a 228 mm long drift distance through the electrostatic deflection plates. The five plates in total are made from copper-epoxy fiberglass and coated with copper sulfide (also used on the NPI deflector plates as described in Chapters 2 and 3) to decrease photon and particle reflections. The plates are separated with poly-ether-ether-ketone (PEEK) insulators, that also function as spokes to collimate the incoming beam over polar angle. The electric field strength between the plates is 10 kV/cm by setting the plate voltages to $\pm$5000 V (every other plate has negative voltage). This results in a deflector cut-off energy at $\approx$ 320 keV

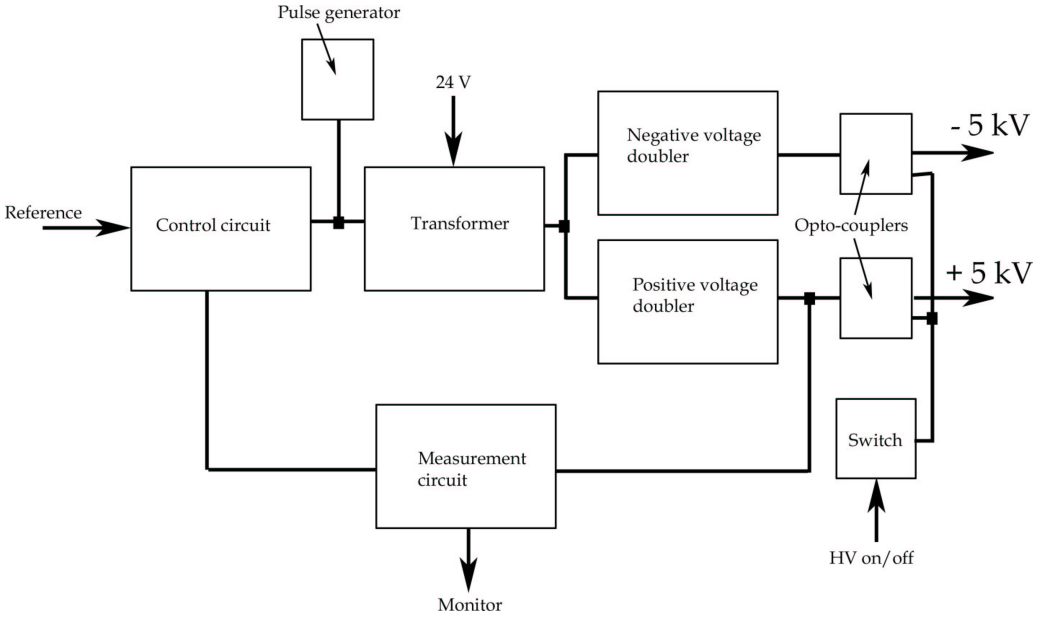


Figure 4.12: Block diagram of the NUADU high voltage supply.

(see Section 4.3.2 for details). The high voltage power supply that supplies the high voltage to the NUADU deflection system was designed, manufactured and tested at IRF in Kiruna. Details about the power supply and its testing are discussed in Section 4.3.1 below.

The sensor head also houses front-end electronics based on 16 Amptek A225 preamplifiers and pulse amplifiers, one for each detector. The conversion gain of each amplification channel was set to 5 V/MeV using 59.6 keV photons from a $^{241}$Am source. Each detector has individual 4-level discriminator and 8-bit counter. This provides a significant level of redundancy since the 16 front-end electronic channels operate independently all the way from detector to counter. The counters are connected to the NUADU DPU, which controls their gating, periodic readout and reset. The DPU also handles data frame formatting and the transmitting them to the spacecraft data handling system via a MIL-STD-1553B interface. A NUADU standard data frame consists of 17 bytes of house-keeping data, 8196 bytes of scientific (image) data and one checksum byte.

### 4.3.1 NUADU high voltage supply

The purpose of the NUADU high voltage supply is to provide two stable voltage outputs that is connected to the electrostatic deflector plates. The output voltage is controlled between $0 - \pm 5000$ V by setting a reference voltage between 0-2.5 V. The design is based on the high voltage supply for the ASPERA-3 NPI sensor. Fig. 4.12 shows a block diagram of the NUADU high voltage supply. An internal pulse generator is connected to a transformer that is operated in a push/pull arrangement (f = 29.1 kHz) with 24 V supplied to the middle of the primary coil. The secondary

Table 4.3: Thermal test results of the NUADU high voltage supply.

| Measurement | T= +50° C | T= −30° C |
|---|---|---|
| + HV | $5.25 \pm 0.01$ kV | $4.93 \pm 0.01$ kV |
| - HV | -5.29 ± 0.01 kV | -4.97 ± 0.01 kV |
| $I_{24\ V}$ | $9.25 \pm 0.39$ mA | $5.27 \pm 0.06$ mA |

coil of the transformer is connected to 7-step voltage doublers, that in every step doubles and rectifies the peak voltage of the oscillation from the transformer. There are two doublers, one with a positive output and one with a negative output. The output from the positive voltage doubler is divided to a value between 0-2.5 V corresponding to the output voltage of 0-5000 V. The divided voltage is then fed back to an amplifier that compares the feedback signal to the reference voltage controlling the pulses that drives the transformer. The feedback signal is also extracted as an high voltage monitor output.

The supply should in addition to direct voltage mode, also operate in a switching mode where the output is toggled between 0 and ±5000 V with a frequency $> 0.5$ Hz. In this mode NUADU will measure ENAs when the high voltage is ON and ENAs plus charged particles when the high voltage is OFF. Switching the 24 V supply voltage to the transformer creates long transients (on the order of 4 seconds) because of the inherent impedance in the voltage doublers. Instead, the positive and negative outputs from the voltage doublers are switched using high voltage opto-couplers, in which the supply output voltages are controlled optically by a controlling the current through an LED. The opto-couplers (Amptek HP601B) are used to switch the high voltage outputs on/off with a TTL level input signal and allow much faster switching (transients on the order of 500 ms).

Besides extensive functional testing the high voltage supply was subjected to thermal vacuum tests conducted at the IRF thermal vacuum test facility. The high voltage supply was placed in $10^{-6}$ mBar vacuum and properly out-gassed for function and thermal cycling tests. The function test was performed in room temperature ($\approx 20°$ C). Two 122 pF capacitors were connected between the high voltage outputs and ground to simulate the load of the deflection plates in NUADU. The results of the functional tests is in Fig. 4.13 which shows the high voltage, monitor voltage, and 24 V current at different reference voltages. As can be seen in the plots there is a remaining voltage of $\approx \pm 300$ V when the reference voltage is set to 0 V. This is because of dark currents in the HP601B opto-couplers. To switch the high voltage output completely OFF the 24 V supply should be switched OFF. The thermal cycling tests followed the diagram in Fig. 4.14 with stable and switching mode run at each test temperature. The temperatures used were $-30°$ and $+50°$ C. The results showed an expected drift with temperature as the resonant frequency of the transformer drifts with temperature. To reduce this drift the design of the supply includes a temperature sensitive capacitor that compensates for some of the resonance drift in the transformer. A total of 10 cycles were run on an electrical qualification model and an additional 3 cycles on the flight model of the supply. The results of the thermal cycling tests on the flight model are in Table 4.3.

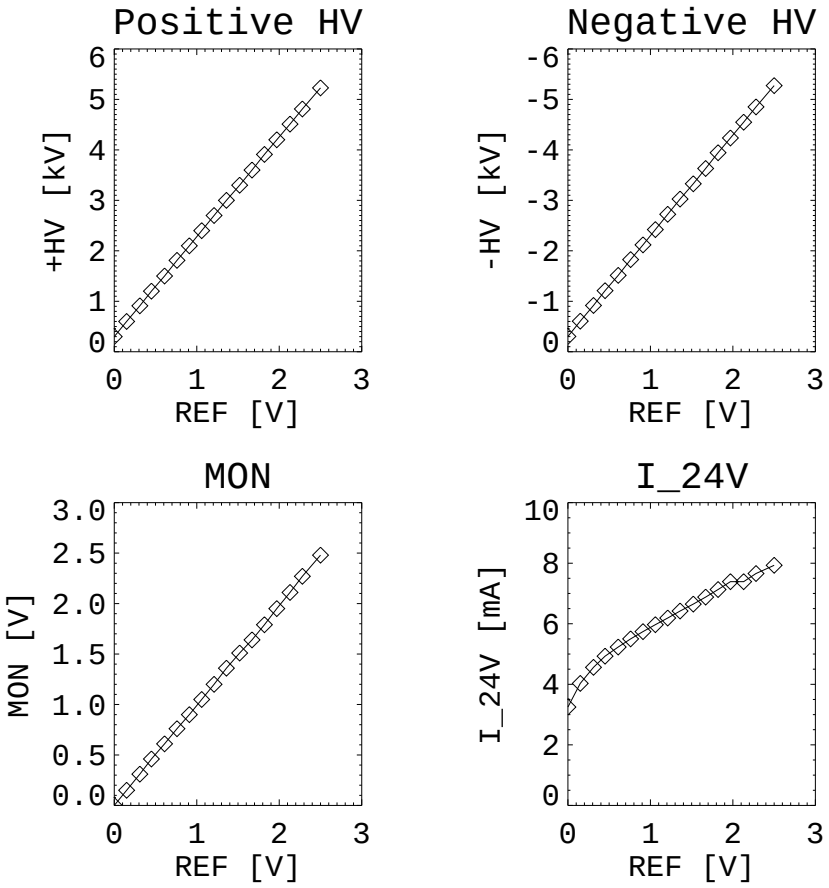


Figure 4.13: High voltage output (top left and right), monitor (bottom left), and 24 V current (bottom right) versus reference voltage for the NUADU high voltage supply. The measurement were made at room temperature ($\approx 20^\circ$ C).

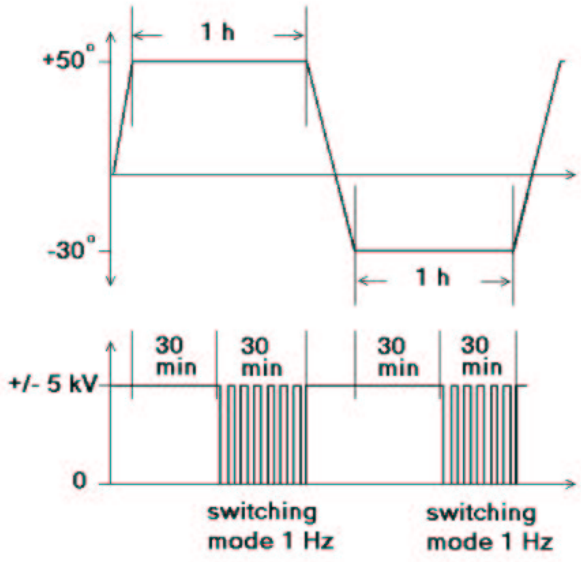


Figure 4.14: The test temperatures and high voltage setting during one cycle in the thermal test.

### 4.3.2 NUADU deflector cut-off energy and G-factor

To determine the cut-off energy of the deflection system particle simulations were performed using the SIMION 3D 7.0 ion optics simulation software. The software models electrostatic fields inside a created 3-dimensional array of electrodes and allows ions to be flown within this modelled potential array. To find the potentials of points in the space between electrodes, SIMION solves the Laplace equation (with the electrodes as boundaries) and then uses an iteration method to find the potential in a given point from evaluation of its nearest neighbor values. The modelled potential array (Fig. 4.15) differed from the final NUADU mechanical design on a number of points. The modifications in the simulation model include thicker outer wall to prevent leakage ions (SIMION treats everything $< 2$ mm as a mesh, inner diameter of the cylinder is correct), only one sector on deflection level 1 is modelled (all other apertures and detectors are omitted), only the sensitive area of the detector is included, deflector plate holders (PEEK spokes) are not included (deflector plates are floating in space), and a 0.5 mm insulating layer between the inner wall of the sensor and the -24 V mesh covering the aperture is not included. Protons and electrons were flown in sets with a specific start energy. Equally spaced (every $4.6 \times 2.0$ mm) starting points covering the aperture were used. From each starting point ions were flown from azimuth ($\alpha$) angles of $-30°$ to $30°$ and elevation ($\beta$) angles of $-10°$ to $10°$. $\Delta\alpha$ and $\Delta\beta$ were $1°$. A total of 66 starting points gives $21 \cdot 61 \cdot 66 = 84546$ particles flown per energy setting. The energies used in this simulation ranged from 1 keV to 1 MeV. A user program was created within SIMION to count the number of ions that hit the detector sensitive area.

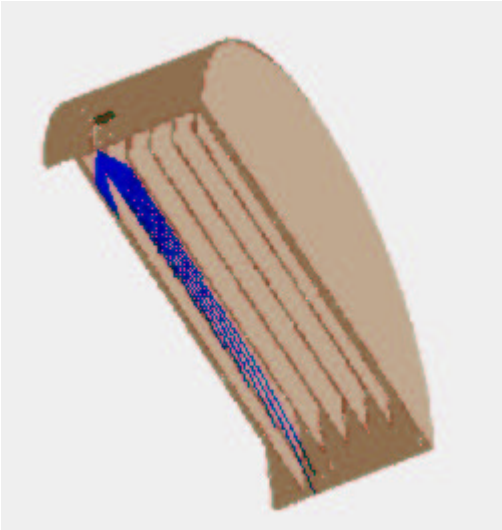

Figure 4.15: The SIMION NUADU model.

The deflector cut-off is defined here at the transmittance level 1 %, that is, the energy at which $N_{HV}/N = 0.01$, where $N_{HV}$ is the number of ions that hit the detector with the deflection voltage on and $N$ is number of ions that hit the the detector with deflector voltage at 0 V. The result of the SIMION simulations are shown in Fig. 4.16. It shows the $N_{HV}$/N ratios for singly charged protons launched at different energies with ±1, ±2.5, and ±5 kV on the deflection plates. The seemingly oscillating nature of the lines is an artifact of the finite launch positions and number of particles in the simulation. The simulated cut-off energy of the NUADU deflection system with nominal deflection voltage (10 kV) is $E_{cut} = 320$ keV for singly charged particles. This can be compared to an estimated value of $E_{cut} = 335$ keV based on equation 1.8.

The geometrical factor of a two element telescope is found from equation 1.5. For the geometry in Fig. 1.5 this is equal to the rather complicated expression [*Sullivan*, 1971]:

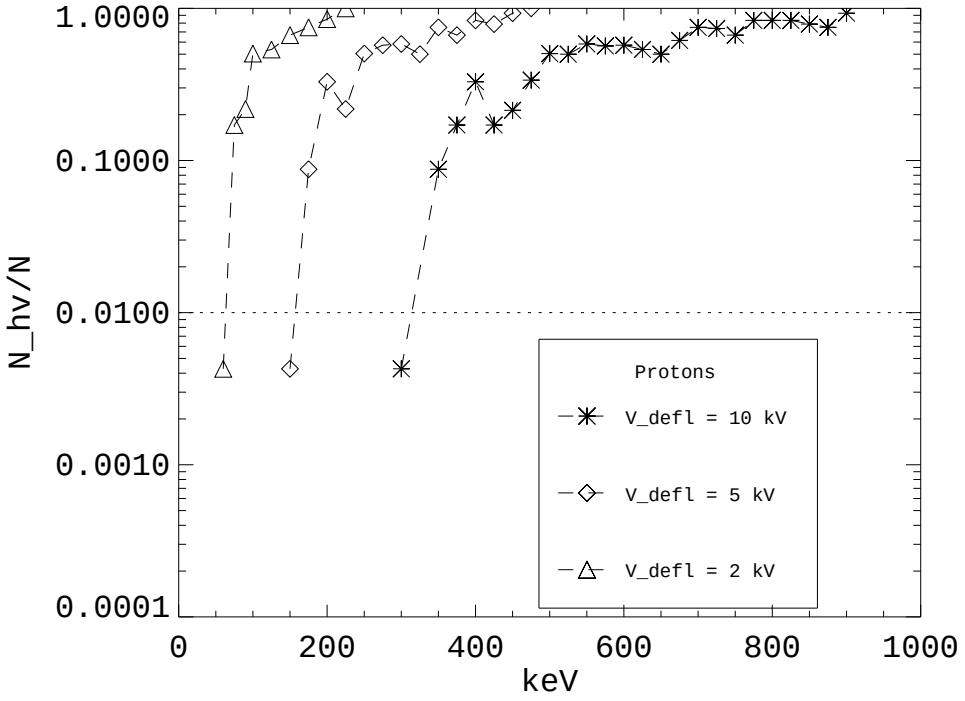


Figure 4.16: Simulated cut-off energy of the NUADU deflection system. The plot show percent of particles that reach the detector for different deflector HV settings and for different energies with respect to a deflector HV setting of 0 V. Protons were simulated.

$$
\begin{aligned}
G \;=\; & l^2 \ln \frac{l^2+\alpha^2+\delta^2}{l^2+\alpha^2+\beta^2} \cdot \frac{l^2+\gamma^2+\beta^2}{l^2+\gamma^2+\delta^2} + \\
& +2\alpha(l^2+\beta^2)^{1/2} \tan^{-1} \frac{\alpha}{(l^2+\alpha^2)^{1/2}} + \\
& +2\beta(l^2+\alpha^2)^{1/2} \tan^{-1} \frac{\beta}{(l^2+\beta^2)^{1/2}} - \\
& -2\alpha(l^2+\delta^2)^{1/2} \tan^{-1} \frac{\alpha}{(l^2+\delta^2)^{1/2}} - \\
& -2\beta(l^2+\gamma^2)^{1/2} \tan^{-1} \frac{\beta}{(l^2+\gamma^2)^{1/2}} - \\
& -2\gamma(l^2+\beta^2)^{1/2} \tan^{-1} \frac{\gamma}{(l^2+\beta^2)^{1/2}} - \\
& -2\delta(l^2+\alpha^2)^{1/2} \tan^{-1} \frac{\delta}{(l^2+\alpha^2)^{1/2}} +
\end{aligned}
\tag{4.1}
$$

$$+2\gamma(l^2+\delta^2)^{1/2}\tan^{-1}\frac{\gamma}{(l^2+\delta^2)^{1/2}}+$$
$$+2\delta(l^2+\gamma^2)^{1/2}\tan^{-1}\frac{\delta}{(l^2+\gamma^2)^{1/2}}\ ,$$

where

$$\begin{aligned}\alpha &= \frac{a_1+a_2}{2},\\ \beta &= \frac{b_1+b_2}{2},\\ \gamma &= \frac{a_1-a_2}{2},\\ \delta &= \frac{b_1-b_2}{2}.\end{aligned}$$

Inserting the values for a NUADU sector (ignoring the curvature of the aperture from the cylindrical shape of the sensor head) the theoretical geometrical factor is

$$G = 1.227\cdot 10^{-2}\ \text{ sr cm}^2.$$

The geometrical factor can be approximated from:

$$G \leq \frac{S_1 S_2}{l^2} \tag{4.2}$$

where $S_1$ is the aperture area, $S_2$ is the detector area and $l$ is the distance between the two. This gives an approximate geometric factor of $G_{approx} = 1.246\cdot 10^{-2}$ cm$^2$ sr for the NUADU sensor, which is very close (within 2 %) to the exact value. An estimation of the geometrical factor based on the SIMION simulation results is found from:

$$G_{sim} = \Delta A\Delta\alpha\Delta\beta\sum_{hit}\cos\varphi_i \simeq \Delta A\Delta\alpha\Delta\beta\cdot N_{hit}. \tag{4.3}$$

Here $\Delta A$ is the elemental aperture area enclosed by four neighboring starting points, $\Delta\alpha$ and $\Delta\beta$ are the azimuth, and elevation angle increments between flown ions, $\varphi_i$ is the incident angle of a hit on the detector, and $N_{hit}$ is the number of ions that hit the detector. Because $\varphi$ is close to 90° ($l \gg \sqrt{S_1}$ and $\sqrt{S_2}$) for all hits, $\cos\varphi_i \simeq 1$. For the SIMION simulation a geometrical factor of:

$$G_{sim} = 1.3116\cdot 10^{-2}\ \text{ sr cm}^2$$

was obtained. This value is close, but somewhat higher than the theoretical value of G= $1.227\cdot 10^{-2}$ sr cm$^2$ because $\cos\varphi_i$ is replaced by unity.

The angular response of one sector on NUADU was also simulated using straight particle trajectories. The result is shown in Fig. 4.17 for azimuth and elevation directions. The noisy representation in the plot for azimuth response comes also from the finite number of particles used in SIMION, but the FWHM values correspond very well with the design values.

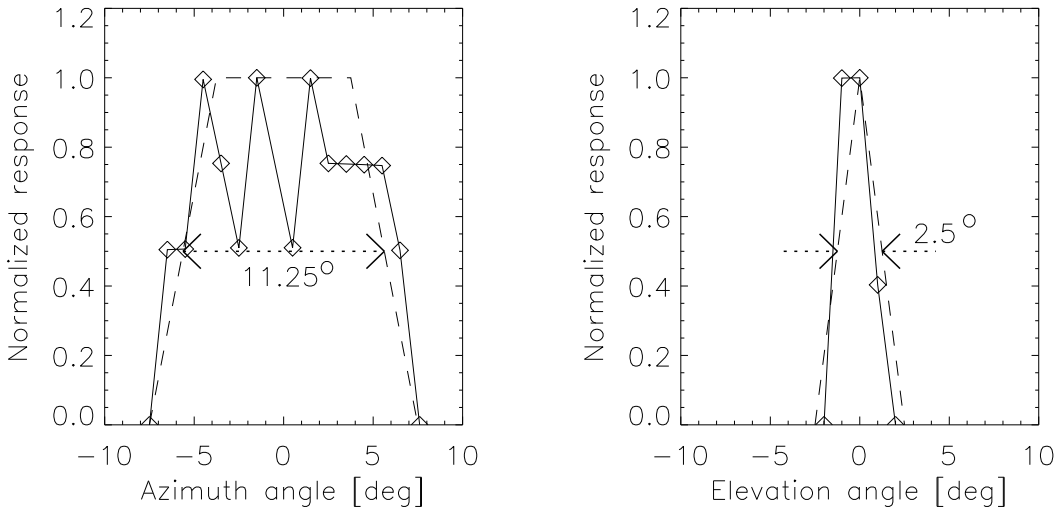


Figure 4.17: Simulated azimuth and elevation response of one NUADU sector. The dashed lines show the response calculated from the geometry of one the sector.

## 4.4 NUADU calibrations

Since the geometry of the sensor is simple the calibration was focused on the energy response of the 16 SSDs for hydrogen and oxygen at several energies. This was primarily required to set the thresholds in the four discriminators that in turn determine the energy channels in NUADU.

The NUADU sensor head was calibrated at the Manne Siegbahn Laboratory (MSL), Stockholm University, Sweden. The 30 m diameter CRYRING accelerator (Fig. 4.18) at MSL was used to generate neutral beams of H and O at different energies. Ions of the species are first injected into the ring at energies 300 keV for $H_2^+$ and 50 keV for $O^+$ then accelerated or decelerated to the energy of choice. A neutral component is continously generated in the ring in charge exchange processes with the very thin, but existing residual gas (the pressure in the ring is typically $10^{-11}$ mBar). Since this component is not charged it cannot follow the curved path of the ions around the ring and instead continue straight in the tangential direction from the ring. A neutral beam can thus be extracted from a 0° tangential output through a long drift tube. During the calibration NUADU was placed in a small vacuum tank at the end of such a tube (see Fig. 4.18). The species and energies used during the calibration are in Table 4.4.

Since the accelerator at MSL is rarely used to generate particles at the low energies required during the NUADU calibration it is quite a challenging to control the beam intensity between each energy/species change. Therefore, a simple beam monitor (BEAMON) was developed with the purpose of verifying the calibration beam intensity before exposing the NUADU flight detectors to it. BEAMON (Fig. 4.19) is based on a spare passivated implanted planar silicon (PIPS) detector from the PIPPI instrument [*Barabash et al.*, 1998] and the charge sensitive preamplifier Cremat CR-

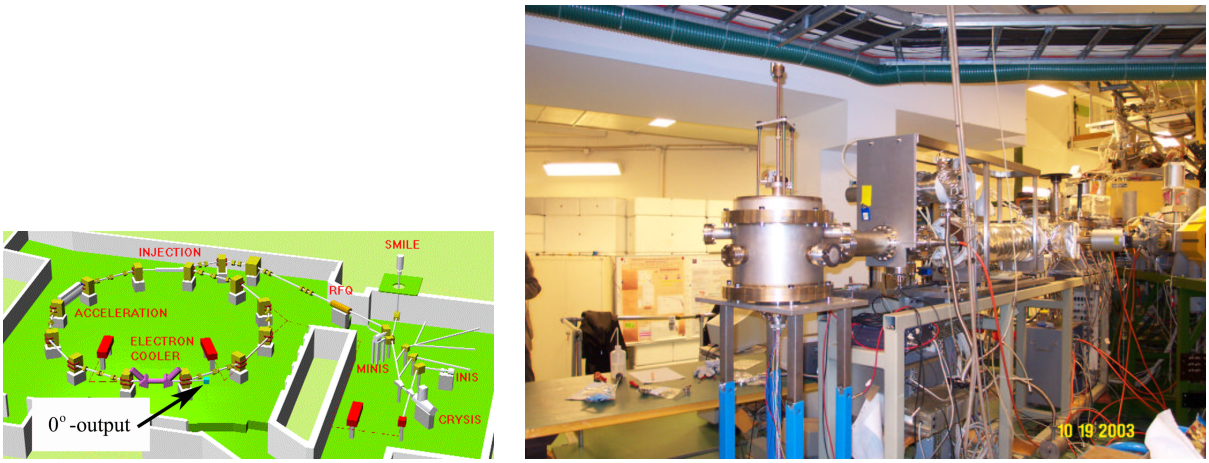


Figure 4.18: The Manne Siegbahn Laboratory CRYRING accelerator with a diameter of 30 m. The tangential 0° output with the NUADU calibration vacuum chamber on the end of a long drift tube is shown to the right.

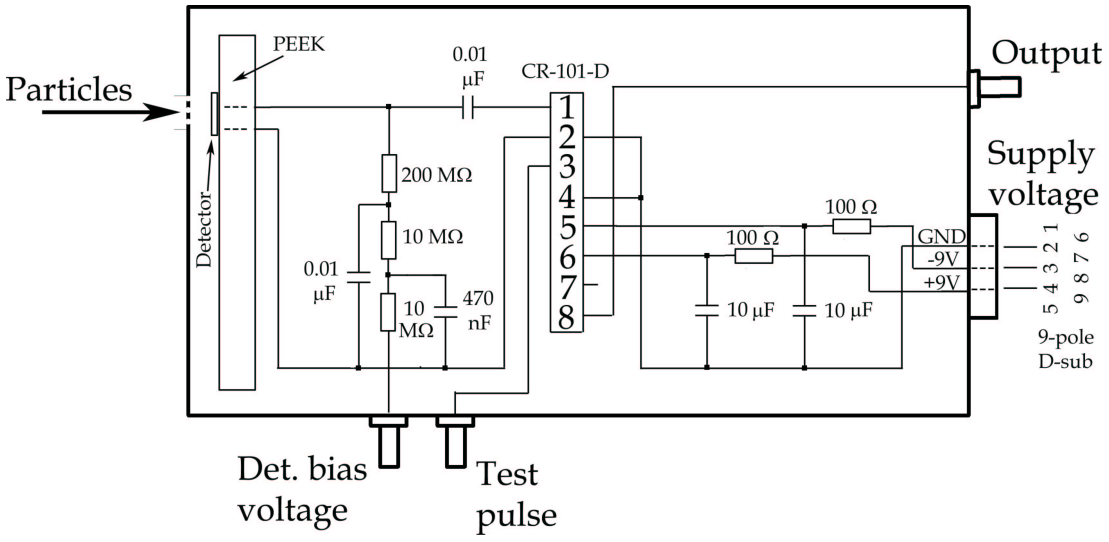


Figure 4.19: BEAMON the beam monitor. Based on a single SSD and preamplifier BEAMON was used to verify the intensity of the calibration beam before the NUADU flight detectors were exposed to it.

Table 4.4: Calibration energies in keV.

| Species: | | | | | |
|---|---|---|---|---|---|
| H | 512.4 | 293.0 | 150.6 | 60.4 | |
| O | 501.8 | 393.5 | 301.1 | 229.9 | 149.8 |

101-D with a gain of 1.2 V/pC. During the MSL calibration output from BEAMON was connected to a shaping amplifier, then a single channel analyzer converting the charge pulses into TTL level pulses, and finally a counter to determine the intensity of the calibration beam.

During the measurements the responses of all 16 NUADU detectors were measured and the output pulse heights from the NUADU amplifiers were recorded with an AmpTek MCA8000 multichannel analyzer (MCA). The measured pulse height distributions are shown in Fig. 4.20 (hydrogen) and Fig. 4.21 (oxygen). There are some accelerator specific effects appearing in the pulse height distributions. To be able to go to low energies in the MSL ring accelerator, $H_2^+$ was used instead of $H^+$. The injection energy into the ring was 300 keV. Most of the $H_2^+$ molecules in the ring that collide with the residual gas are split up into one neutral H and one $H^+$. For example using a $H_2^+$ beam at 1 MeV in the ring an H atom of energy 500 keV can be extracted via the tangential output. However, there is about a 10 % probability that the entire $H_2^+$ molecule is neutralized and a $H_2$ molecule at 1 MeV is extracted instead. The $H_2$ component is visible in the calibrated pulse height distributions as a small peak at twice the H energy (marked with $H_2$ in Fig. 4.20). Also, the ion injection energy from the ion source into the ring is at 300 keV for hydrogen and at 125 keV for oxygen. The beam is then accelerated or decelerated in the ring to the desired energy. During this time several full revolutions in the ring are completed. This means that until the final beam energy is achieved there are neutrals at the instantaneaous energy ejected at the 0° output during every revolution that are measured with NUADU. The effect is visible in Fig. 4.20 and Fig. 4.21 as a slightly elevated background. Also the injection energy is visible in Fig. 4.20. It is important to emphasize that the measured pulses are separated in time and not an effect in the NUADU detector.

During the calibrations detectors 2 and 12 suddenly became noisy. These detectors were replaced after the calibration. Results of detectors 2 and 12 are omitted here as they are no longer included in the sensor.

To set the thresholds for the NUADU discriminators, which determine the instrument energy channels, the MCA channel numbers have to be related to energy and also to voltage pulse amplitudes from the NUADU amplifiers. Fig. 4.22 shows the MCA linearity and Fig. 4.23 the MCA channel number and amplifier output as functions (linear) of the particle energy for hydrogen and oxygen. From Fig. 4.22 and Fig. 4.23, if E is in keV and V is in volts, then for H:

$$V = (0.00496682 \times E_H) - 0.156747 \tag{4.4}$$

and for O:

$$V = (0.00330185 \times E_O) - 0.364899 \tag{4.5}$$

The discriminator thresholds on NUADU are in Table 4.5. Setting of the discriminator thresholds

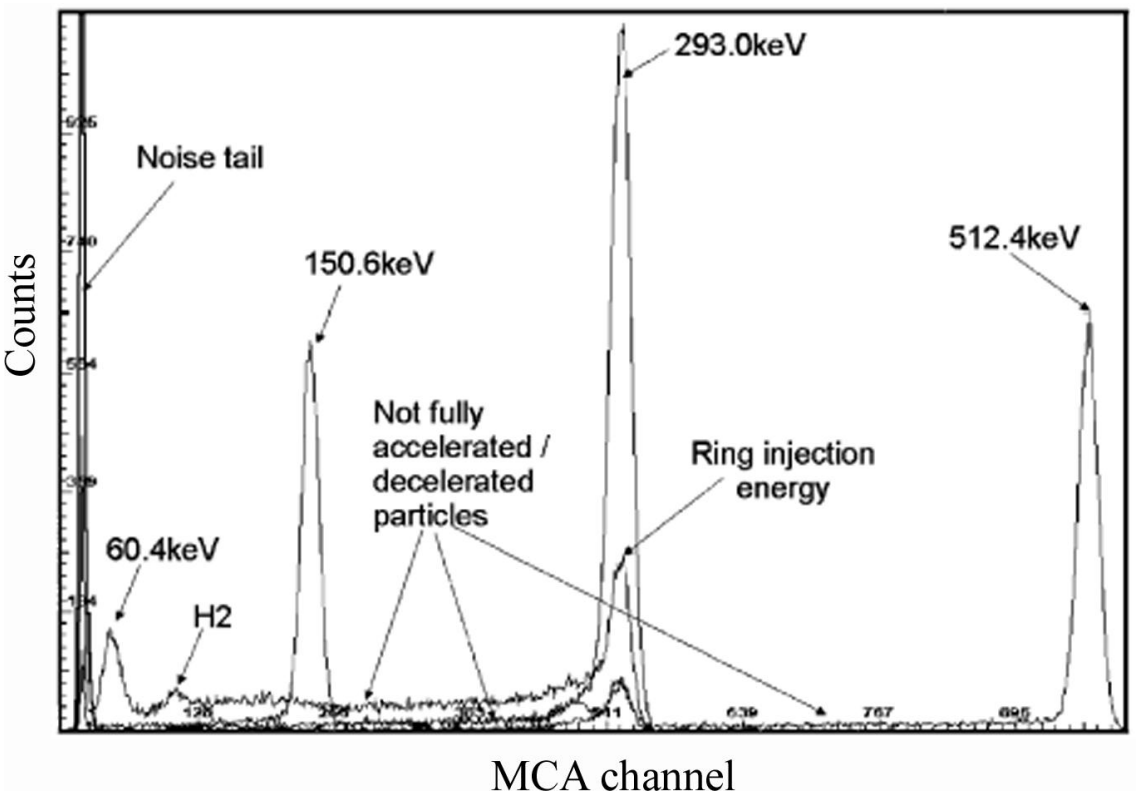


Figure 4.20: Detector 11 responses to hydrogen of all energies during the calibration.

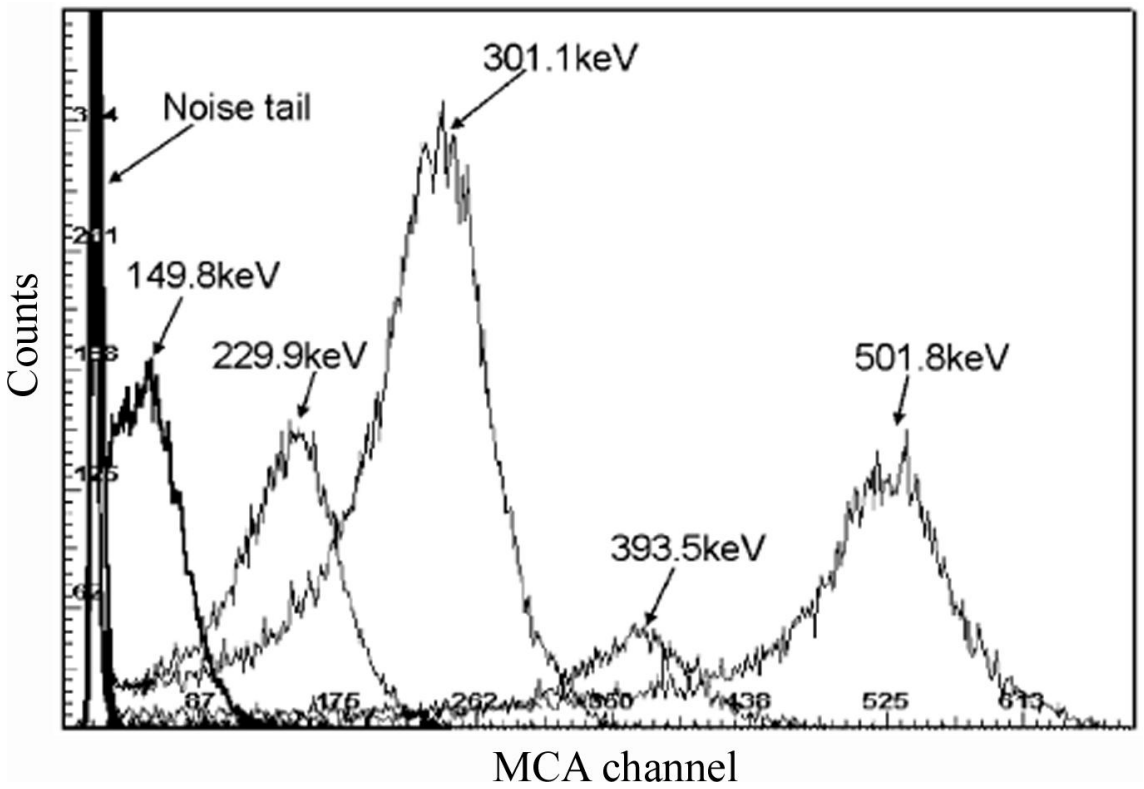


Figure 4.21: Detector 11 responses to oxygen of all energies during the calibration.

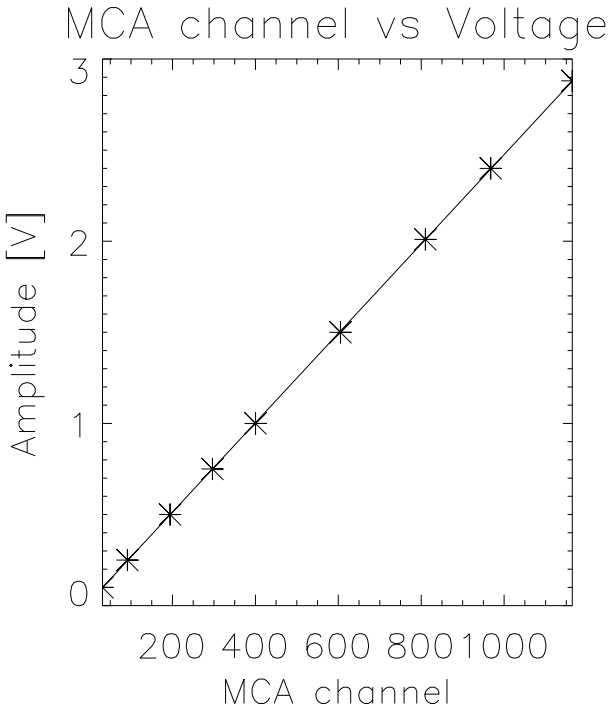


Figure 4.22: The MCA channel is linearly related to the voltage pulses. This information is then used to set the discriminator thresholds to energies.

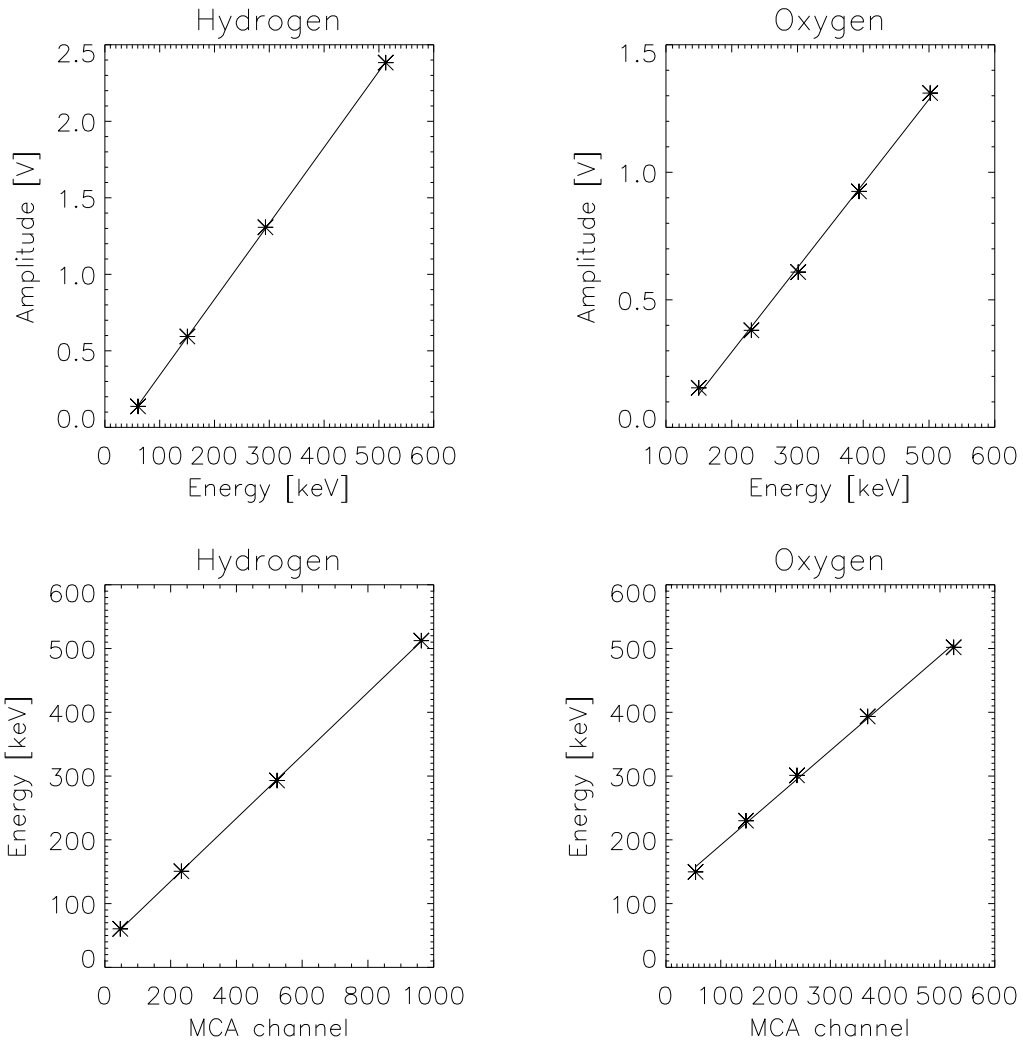


Figure 4.23: The plots shows how voltage pulse amplitudes and channel numbers are related to the particle energy for Hydrogen and Oxygen.

Table 4.5: Discrimination thresholds set in the NUADU instrument.

| Threshold | Pulse height | Energy (hydrogen) |
|---|---|---|
| TH1: | Noise level | $\approx 20$ keV |
| TH2: | 92 mV | 50 keV |
| TH3: | 246 mV | 81 keV |
| TH4: | 626 mV | 158 keV |

Table 4.6: Energy levels of the NUADU instrument in keV.

| Energy channel | H (keV) | O (keV) |
|---|---|---|
| E1: TH1–TH2 | $\approx 20$–50 | $< 138$ |
| E2: TH2–TH3 | 50–81 | 138–185 |
| E3: TH3–TH4 | 81–158 | 185–300 |
| E4: TH4–$E_{cut}$ | 158–300 | $> 300$ |

took into account the following factors:

1. The expected ENA energy spectra determined by the charge exchange cross section dependence on energy.
2. The NUADU deflector cut-off energy (300 keV).
3. Energy resolution/straggling in the metalization and dead layers.
4. Possibility of indirect mass identification related to the stronger dependence on energy of the proton resonance charge-exchange than oxygen-hydrogen charge exchange.

In addition, the thresholds in NUADU were set to correspond to the energy levels of the HENA instrument [*Mitchell et al.*, 2000] on the IMAGE spacecraft for hydrogen to ease the comparison of the data. The NUADU deflector cut-off energy is 320 keV. This value varies slightly with temperature, but the effect is considered to be negligible. To allow for some margin a cut-off energy of 300 keV is used. The final energy levels in NUADU are listed in Table 4.6. Fig. 4.24 shows the expected H- and O-ENA fluxes for the distributed magnetospheric conditions (Kp=7) as would be detected by an ENA instrument on the TC-2 orbit as well as the energy- pulse-amplitude dependence. The discriminator thresholds are marked by vertical lines. Since very few hydrogen ENAs are expected above 150 keV because of a drop-off in the charge-exchange cross section, TH4 is set such that the E4 energy channel will be dominated by oxygen ENAs. Conversely, since very little oxygen is expected above 185 keV because of energy straggling in the detector metalization layer and dead layer, energy channels E1, E2, and E3 are dominated by hydrogen ENAs. From balancing the energy levels with the expected intensities, NUADU may differentiate between hydrogen and oxygen at disturbed magnetospheric conditions.

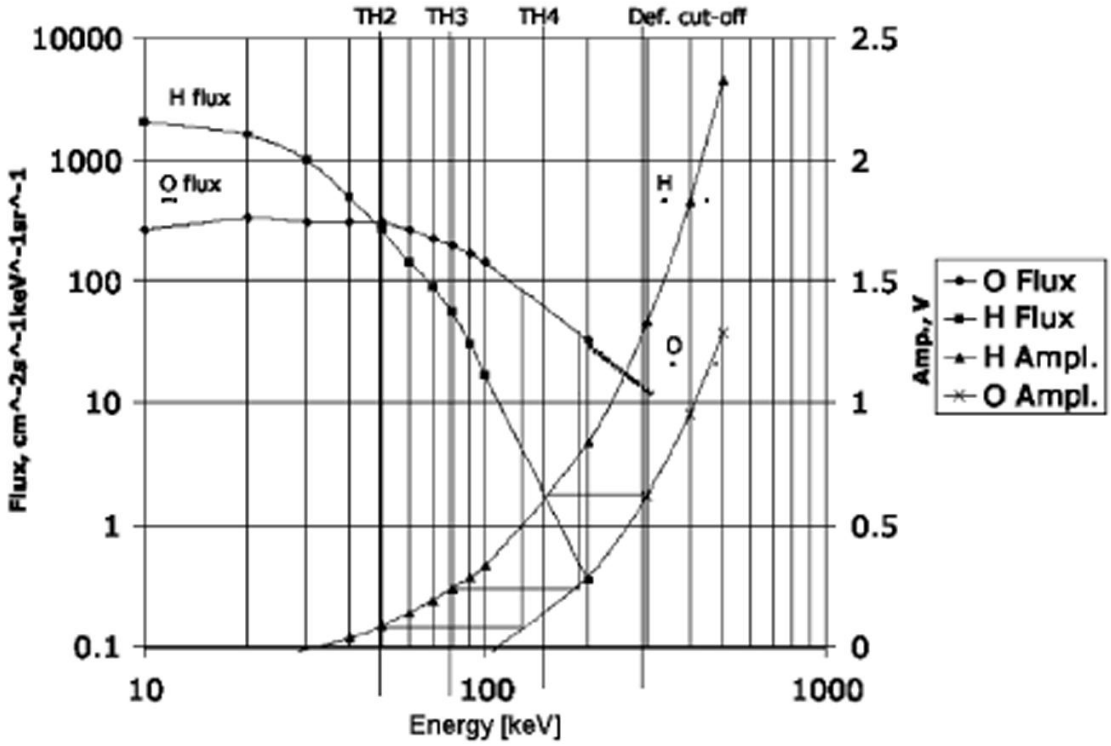


Figure 4.24: The expected ENA flux for distributed magnetospheric conditions (Kp=7) and pulse amplitude to energy relationships for Hydrogen and Oxygen.

The energy calibration of each detector showed small variations between detector performance (see Tables 4.7 and 4.8). Any variation could be an effect of slight differences in the thickness of

Table 4.7: Centroid (C) and FWHM (F) in MCA channels at calibration energies for Hydrogen.

| Energy [keV]: | 60.4 | | 150.6 | | 293.0 | | 512.4 | |
|---|---|---|---|---|---|---|---|---|
| Detector: | C | F | C | F | C | F | C | F |
| 1 | 50.7 | 16.3 | 242 | 18.5 | 542 | 22.9 | 947 | 21.2 |
| 2 | – | – | – | – | – | – | – | – |
| 3 | 49.6 | 17.6 | 238 | 19.2 | 534 | 22.3 | 978 | 22.2 |
| 4 | 48.4 | 17.4 | 237 | 17.9 | 532 | 20.4 | 979 | 21.3 |
| 5 | 48.2 | 15.4 | 236 | 17.6 | 531 | 21.2 | 976 | 20.7 |
| 6 | 48.3 | 16.5 | 235 | 18.3 | 528 | 22.8 | 971 | 22.2 |
| 7 | 46.6 | 14.2 | 254 | 16.6 | 528 | 20.5 | 965 | 20.7 |
| 8 | 47.8 | 16.6 | 235 | 18.5 | 526 | 21.5 | 967 | 21.8 |
| 9 | 47.8 | 16.5 | 233 | 17.7 | 526 | 22.1 | 965 | 22.1 |
| 10 | 48.0 | 16.7 | 233 | 18.3 | 523 | 22.1 | 968 | 22.3 |
| 11 | 46.8 | 16.1 | 254 | 18.6 | 523 | 21.7 | 962 | 20.5 |
| 12 | – | – | – | – | – | – | – | – |
| 13 | 46.7 | 17.6 | 236 | 20.8 | 534 | 22.5 | 980 | 23.6 |
| 14 | 49.4 | 16.5 | 236 | 19.3 | 531 | 23.0 | 976 | 21.9 |
| 15 | 49.5 | 15.0 | 236 | 19.4 | 529 | 22.7 | 973 | 24.0 |
| 16 | 47.7 | 11.5 | 235 | 19.4 | 526 | 23.1 | 969 | 22.0 |
| Mean | 48.3 | 16.0 | 238 | 18.6 | 529 | 22.1 | 970 | 21.9 |
| Std. dev. | 1.19 | 1.59 | 6.79 | 1.01 | 5.16 | 0.87 | 8.68 | 1.02 |

the metalization and dead layers, and amount of impurities in the detectors. The oxygen atoms undergo many more deflections along their path through the layers resulting in both wider and over-all lower pulse height distributions in Fig. 4.21 compared to Fig. 4.20.

For hydrogen the $\Delta E/E$ at FWHM for 150.6 keV is 8 % for all detectors (mean) and for 300 keV oxygen the resolution is 28 %. The result of all detectors for the different energies (calculated using the relationships in Fig. 4.22 and 4.23) are shown in Fig. 4.25 for hydrogen and Fig. 4.26 for oxygen. Detector number 13 shows slightly higher pulse heights at high energies. This could be due to that detector having a slightly thinner metalization or dead layer.

## 4.5 NUADU first observations

Two NUADU observations from the first year in orbit are presented here. First, low altitude ENA emissions were recorded by NUADU at TC-2 spacecraft south polar passages during a moderate magnetospheric storm in September 2004, then a high altitude image of ring current ENA emissions from a vantage point on the northern hemisphere were recorded by NUADU, while, simultaneously,

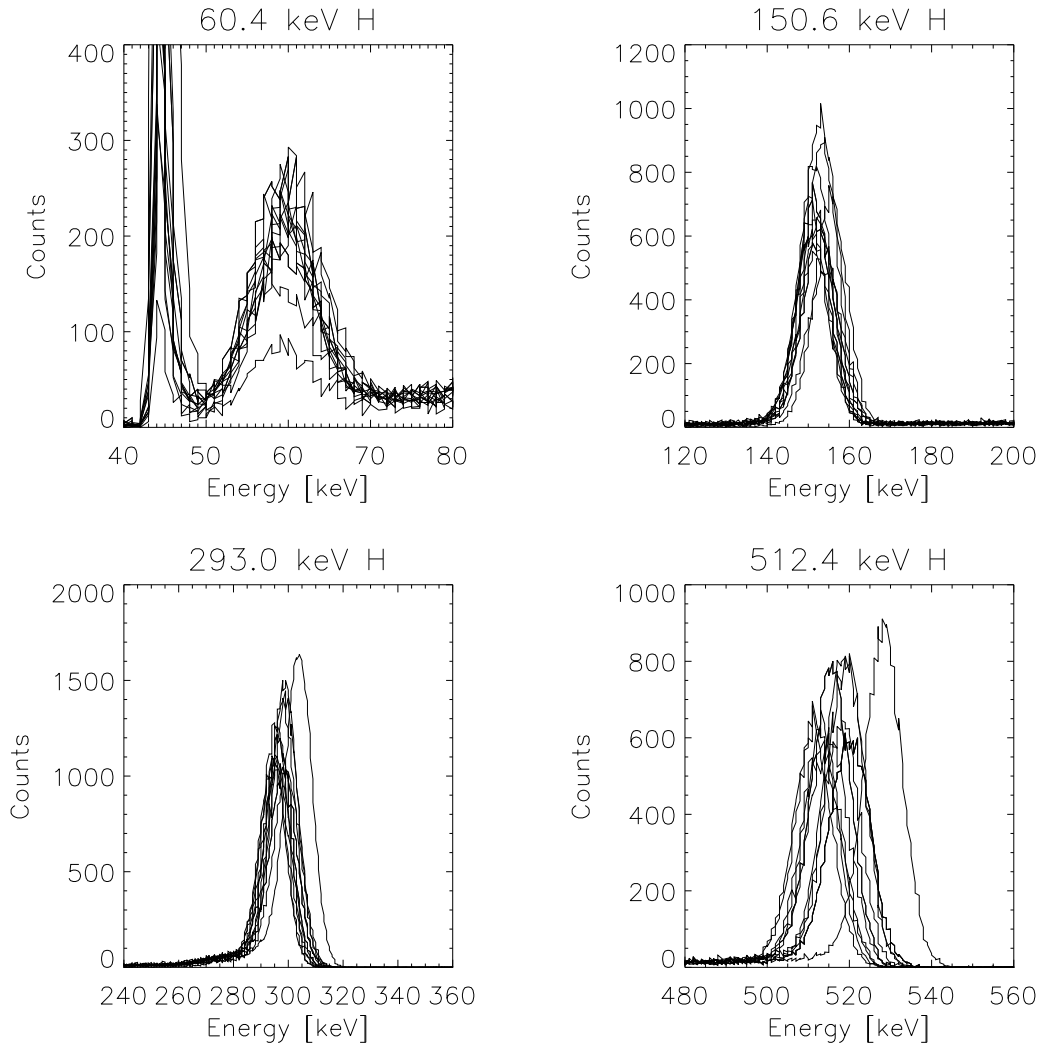


Figure 4.25: Response of all detectors to Hydrogen of different energies. Detector 13 shows slightly higher pulse heights at high energies. This could indicate a thinner than average metalization layer.

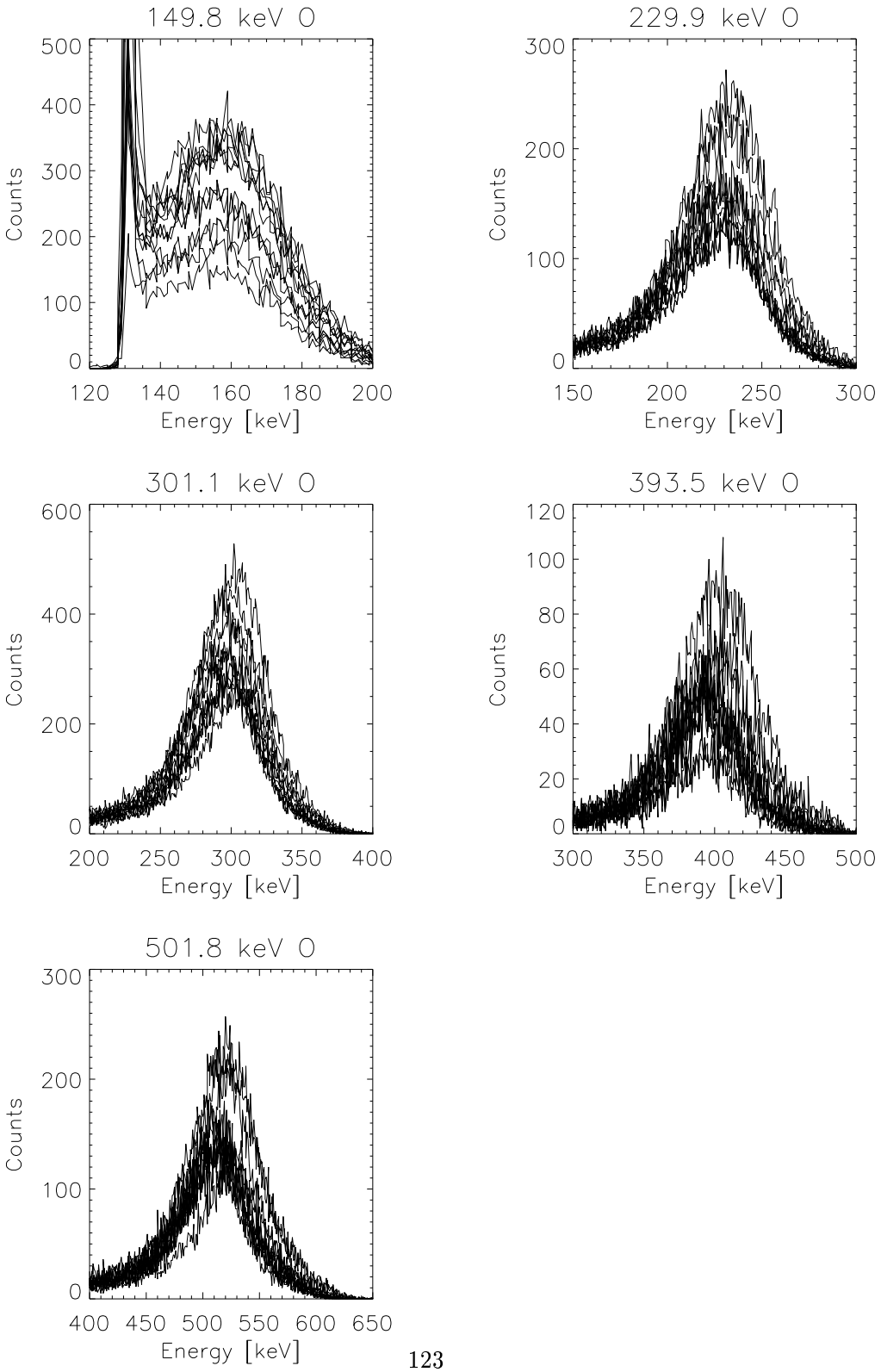




Figure 4.26: Response of all detectors to Oxygen of different energies.

Table 4.8: Centroid (C) and FWHM (F) in MCA channels at calibration energies for Oxygen.

| Energy [keV]: | 149.8 | | 229.9 | | 301.1 | | 393.5 | | 512.4 | |
|---|---|---|---|---|---|---|---|---|---|---|
| Detector: | C | F | C | F | C | F | C | F | C | F |
| 1 | 51.6 | 31.9 | 151 | 54.6 | 247 | 63.2 | 384 | 64.7 | 545 | 67.6 |
| 2 | – | – | – | – | – | – | – | – | – | – |
| 3 | 50.3 | 30.3 | 148 | 50.6 | 244 | 65.4 | 378 | 53.1 | 539 | 72.5 |
| 4 | 50.5 | 28.8 | 143 | 53.1 | 239 | 66.5 | 367 | 62.1 | 529 | 71.4 |
| 5 | 49.7 | 31.9 | 146 | 54.2 | 238 | 68.5 | 365 | 51.1 | 528 | 63.9 |
| 6 | 49.7 | 10.1 | 138 | 40.3 | 237 | 65.3 | 359 | 46.8 | 527 | 65.3 |
| 7 | 51.0 | 22.2 | 137 | 57.2 | 233 | 61.7 | 362 | 43.7 | 522 | 51.6 |
| 8 | 57.6 | 34.1 | 141 | 54.7 | 235 | 63.5 | 371 | 42.7 | 523 | 65.2 |
| 9 | 52.4 | 31.3 | 149 | 53.4 | 235 | 64.1 | 370 | 39.7 | 525 | 74.7 |
| 10 | 53.6 | 20.7 | 140 | 46.5 | 233 | 60.4 | 363 | 40.4 | 522 | 61.8 |
| 11 | 52.3 | 7.7 | 133 | 50.7 | 229 | 64.8 | 353 | 46.6 | 524 | 60.6 |
| 12 | – | – | – | – | – | – | – | – | – | – |
| 13 | 64.3 | 16.7 | 149 | 49.4 | 240 | 63.2 | 392 | 48.7 | 550 | 58.7 |
| 14 | 56.9 | 27.7 | 142 | 52.3 | 239 | 62.7 | 373 | 34.4 | 537 | 61.2 |
| 15 | 56.2 | 23.2 | 139 | 50.5 | 235 | 66.0 | 371 | 48.9 | 525 | 72.7 |
| 16 | 56.7 | 25.8 | 140 | 45.5 | 235 | 62.9 | 364 | 35.3 | 528 | 53.6 |
| Mean | 53.8 | 24.5 | 143 | 51.0 | 237 | 64.2 | 369 | 47.0 | 530 | 64.4 |
| Std. dev. | 4.14 | 8.23 | 5.34 | 4.41 | 4.61 | 2.09 | 10.1 | 8.87 | 8.87 | 7.06 |

the HENA instrument [*Mitchell et al.*, 2000] on the IMAGE spacecraft recorded an image from the southern hemisphere during a major magnetospheric storm in November 2004. Currently NUADU data analysis is in its initial phase and we here only show basic results demonstrating the instrument capabilities.

### 4.5.1 Low altitude ENA emissions

Fig. 4.27 shows three NUADU hydrogen ENA images in the 50-81 keV energy channel from a perigee pass over the south pole during the recovery phase of the moderate ($D_{st}$ index was recovering from $\sim$ -50 nT) substorm on 14 September 2004. The Earth's limb, terminator, and L-shells 4 and 8 are plotted assuming the spin axis perpendicular to the ecliptic plane. The exact spin axis of TC-2 during this measurement was uncertain due to the attitude control computer failure. As a result, the ENA emissions may be offset by a few degrees in the plot. The images show ENA emissions from the interaction between the upper atmosphere and trapped ions from the ring current. Trapped ions spiral down the terrestrial magnetic field lines and charge exchange with the upper atmosphere resulting in intense ENA emissions. The heaviest precipitation occurs near midnight which corresponds to the ENA observations, but this is also an effect of the viewing geometry. The typical viewing geometry for a perigee pass is illustrated in Fig. 4.28. The most intense

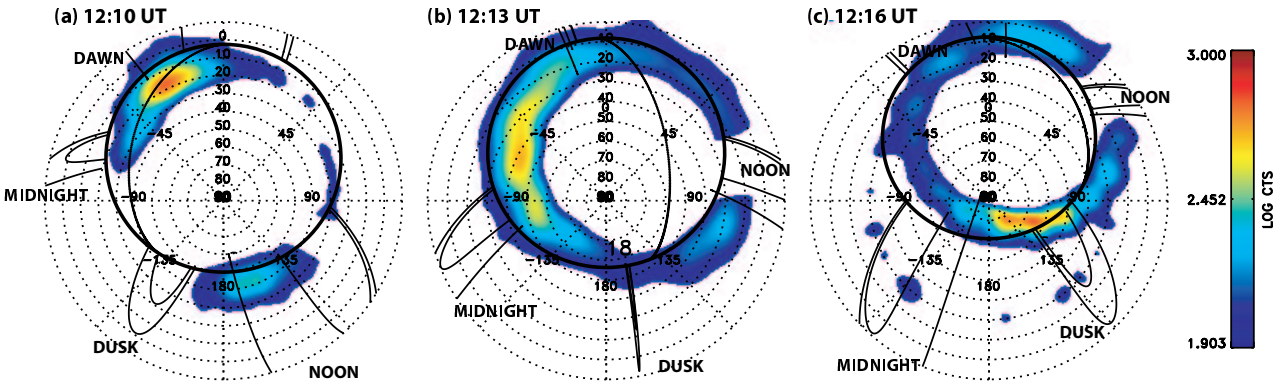


Figure 4.27: Low altitude ENA emissions measured with the NUADU instrument as the TC-2 satellite pass the south pole on a perigee pass 14 September 2004. The image projection is similar to the ones in Fig. 4.4. The Earth's limb, terminator and dipole L-shells 4 and 8 are plotted as solid lines. From [*McKenna-Lawlor et al.*, 2005].

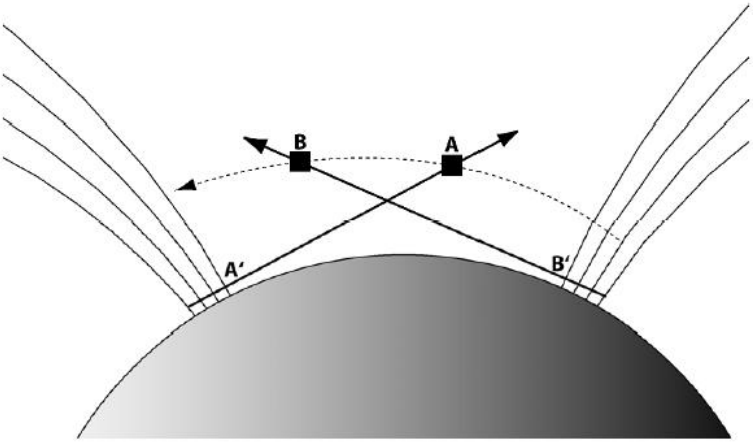


Figure 4.28: Viewing geometry during a typical south polar perigee pass of TC-2. From [*McKenna-Lawlor et al.*, 2005].

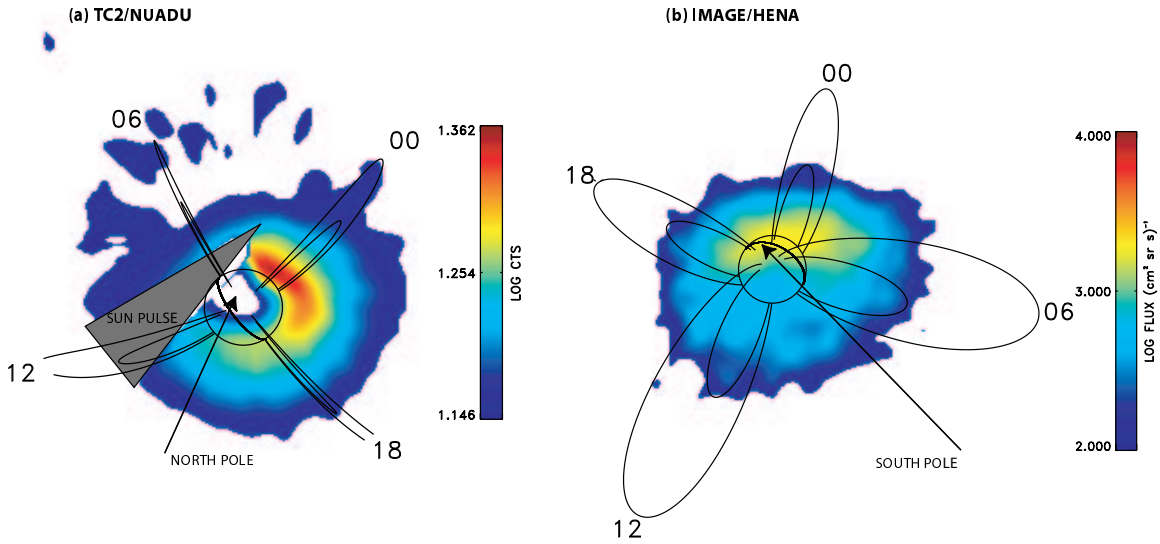


Figure 4.29: (Left) ENA image recorded by NUADU in the 81-58 keV energy channel from 10:10-10:23 UT on 8 November 2003 from a vantage point in the northern hemisphere. (Right) ENA image recorded simultaneously by HENA in the 60-119 keV energy range from a vantage point in the southern hemisphere. From [*McKenna-Lawlor et al.*, 2005].

ENA emissions originates from a region at 350 km altitude. At these altitudes there is an optimal (for ENA production) balance between ion flux attenuation caused by the interaction with the atmosphere and ENA flux attenuation caused by stripping [*Roelof*, 1997]. The ENAs generated in this region forms a layer almost perpendicular to the field at these altitudes because the ions have pitch-angles close to 90°. Because of the relatively low altitude over the polar region the NUADU line of sight crosses this layer in the point distant from the production region as illustrated in Fig. 4.28. The exact geometry and distribution of the low-altitude emissions is far more complicated than the situation depicted in the figure, but this picture is, none the less, qualitatively correct.

The ENA emissions recorded at 12.10 UT (Fig. 4.27, left), came from the sector midnight-to-dawn. This is consistent with the interpretation provided by Fig. 4.28. Six minutes later when the spacecraft has moved in its orbit the emissions in Fig. 4.27 have, correspondingly, moved.

### 4.5.2 NUADU and HENA: Simultaneous storm ring current imaging

Fig. 4.29 (left) shows a high altitude NUADU image from a vantage point in the northern hemisphere recorded during the recovery phase of a major substorm on 8 November 2004 in the 81-158 keV range during a 13 minute integration period starting at 10:10 UT. At that time, the $D_{st}$ index was in an early stage of recovery from $\sim$ -370 nT. The observation show classical enhanced emissions in the local midnight through dusk sector, indicating that ions are injected on the nightside into

the inner magnetosphere. The intense ENA emissions at the foot of the midnight field lines are produced where trapped ring current ions charge exchanged with the dense upper atmosphere as described in the previous section. Fig. 2.29 (right) shows the ENA image obtained simultaneously by IMAGE/HENA in the 60-119 keV range during a 20-minute integration period. At this time the IMAGE satellite was viewing the Earth a vantage point from the southern hemisphere. The general morphology displayed in the two images is consistent, with low-altitude ENA emissions where the ring current ions reached the upper atmosphere and a wrapping around the Earth on the nightside.

Since HENA is capable of separating hydrogen from oxygen [*Mitchell et al.*, 2000] the simultaneously recorded data can be used to estimate the mixing ratio between the hydrogen and oxygen detected in NUADU. The NUADU energy channels for H and O are described in Table 4.6. The NUADU energy channel E3 detects H in the 81-158 keV range and O in the 185-300 keV range. From HENA, the hydrogen ENA flux at E3 energies during storms are typically about two orders of magnitude higher than the oxygen ENA flux. This means that NUADU detected predominantly hydrogen in its third energy channel. While there may be cases when the oxygen ENA flux is exceptionally strong, in most storms NUADU will image hydrogen exclusively as expected.

# Chapter 5

# Summary and future plans

*"I don't see much sense in that," said Rabbit.*
*"No," said Pooh humbly, "there isn't. But there was going to be*
*when I began it. It's just that something happened to it along the way."*
–Winnie the Pooh, by A. A. Milne

This thesis deals with the development of ENA instruments for planetary (Mars and Venus) and magnetospheric missions. The general design and modern concepts of ENA instruments have been reviewed in Chapter 1. Chapters 2, 3, and 4 describe design, development, testing, calibrations, and initial results from the ENA sensors NPI and NUADU for the Mars Express, Venus Express, and Double Star missions. The NPI sensors (almost identical for Mars and Venus Express) are based on surface reflection techniques to decrease the low energy detection limit down to 100 eV. NUADU uses conventional SSD to cover the typical ring current energy range ($\sim$ 20-300 eV) and is designed to have a very large geometrical factor per pixel ($1.23 \times 10^{-2}$ cm$^2$ sr) and high angular resolution (2.8°-11.5°) independent of energy.

The Mars Express/NPI calibrations were conducted at the IRF ion beam facility in Kiruna, Sweden and the following instrument characteristics have been defined:

- optimal MCP bias,
- efficiency dependence on the incoming particle energy,
- geometrical factor,
- angular response function,
- relative efficiency for all sensor directions, and
- dark current.

A so-called priority effect caused by capacitive coupling between NPI detector anodes and finite size of the electron cloud emerging from MCP was investigated and measures to minimize it were developed and implemented. The calibrated instrument characteristics are the key for the following ENA image deconvolution to reconstruct the original ion distributions. Mars Express has spent approximately 2 years in orbit and at the time of writing of this thesis the following results coming from the Mars Express NPI data analysis can be reported:

1. Detection of ENAs from the shocked solar wind in the magnetosheath region and an attempt to deduce the parameters of the original plasma and neutral gas distributions;

2. Observations of ENAs from the upstream solar wind in the Martian eclipse and analysis of the use of these observations to obtain solar wind characteristics (temperature) and to study ENA-upper atmosphere interactions;

3. Possible observations of neutral beams external to the Martian system.

Similar calibrations have been conducted on the Venus Express NPI. The priority effect was eliminated following the extra development work. Additionally, the UV rejection efficiency (against Lyman-$\alpha$) was calibrated at the Lunar and Planetary Laboratory, University of Arizona, Tucson. The results of the photon calibrations showed that the NPI photon efficiency is $\sim 5{\times}10^{-6}$ for Lyman-$\alpha$ wavelengths ($\lambda = 126.1$ nm). Using the calibrated parameters, simulations of the expected ENA images were conducted . Despite higher solar wind flux and denser exosphere, the expected ENA signal from Venus is weaker than from Mars.

Because of the simple geometry of the NUADU instrument, the calibration strategy involved simulations to find the cut-off energy, geometrical factor, and angular response. The NUADU sensor head was then calibrated to find the response to particles of different mass and energy using neutrals generated in the 30 meter diameter CRYRING accelerator at Manne Siegbahn Laboratory, Stockholm University. In the frame of the NUADU experiment, a high voltage supply providing the NUADU deflector voltage was also developed and tested. It is still fully operational after 1.5 years in orbit. The first results from NUADU in Earth orbit show the storm ring current image recorded on November 8, 2004, as well as bright low altitude ENA emissions. Together with the HENA instrument on the IMAGE spacecraft, NUADU has produced the first simultaneous ENA image of the ring current from two different vantage points.

The analysis of data from the instruments developed is still in its initial phase. With Mars Express ENA sensors (NPD and NPI) operational at Mars for almost two years, a large data set has been collected, and is just starting to be explored. NPI data are not very simple to analyze (as is the case for any ENA data) because of UV contamination and a, basically, unknown ENA environment. In the near future the analysis will be concentrated on NPI-NPD data inter-comparison, observations in the eclipse, and identifying suitable geometries for the observations in the magnetospheath. Note that, at the moment of writing, the ASPERA-3 scanner has not yet been initialized and all data analysis has been made within the 2D world defined by the NPI sensor plane! Venus Express will arrive at Venus on April 11, 2006. With the Mars Express experience to build on, hopes are high that the data analysis will quickly reach the stage it currently is at Mars. The NUADU data analysis will follow the general methods developed for the HENA instrument, while fully exploring the opportunity of multi-point imaging.

This thesis marks an important milestone in the field of ENA imaging (or ENA diagnostics) of space plasmas. The initial survey of the Earth magnetosphere in ENAs is complete and ENA instrumentation has been sent to study other, planetary, environments. In 2007, the instrument SARA (Sub-keV Atom Reflecting Analyzer) will be launched to the Moon onboard the Indian mission Chandrayaan-1. With this sensor, the first-ever ENA imaging mass spectrometer, based on

the conversion and surface reflection technique, will attempt imaging of ENAs sputtered from the surface by the solar wind. A copy of SARA, the ENA (Energetic Neutrals Analyzer) instrument, was selected to fly to Mercury onboard the Japanese Mercury Magnetospheric Orbiter. The second spacecraft of the Bepi Colombo mission, ESA's Mercury Planetary Orbiter will carry a low energy neutral detector as a part of the SERENA (Search for Exospheric Refilling and Neutral Abundances) package.

Development at IRF is now proceeding in the direction of increasing mass resolution of ENA detectors, while keeping G-factor and angular resolution as high as possible. This is a big challenge requiring non-standard approaches. One of the possible innovations are systems based on micro electronic and mechanical systems (MEMS) technology. Ultra-fast mechanical shutters can be used as velocity filters as outlined in Chapter 1. A MEMS based ion mass spectrometer is being developed to fly on-board the Swedish technological satellite PRISMA in 2008 to verify and space qualify MEMS components for future ENA applications.

# Bibliography


Ajello, J. M., A. I. Stewart, G. E. Thomas, and A. Graps, Solar cycle study of interplanetary Lyman-alpha variations: Pioneer Venus orbiter sky background results, *Astrophysical Journal*, *317*, 964–986, 1987.

Andersen, H. H., and J. F. Ziegler, Hydrogen, Stopping powers and ranges in all elements, in *The stopping and ranges of ions in matter, 3*.

Baker, D. N., Telescopic and microscopic views of the magnetosphere: Multispacecraft observations, *Space Sci. Rev.*, *109*(1-4), 133–153, 2003.

Barabash, S., Satellite observations of the plasma - neutral coupling near Mars and the Earth, Ph.D. thesis, Swedish Institute of Space Physics, Kiruna, Sweden, iSBN 91-7191-124-3, 1995.

Barabash, S., R. Lundin, T. Zarnowiecki, and S. Grzedzielski, Diagnostics of energetic neutral particles at Mars by the ASPERA-C instrument for the Mars 96 mission, *Adv. Space Res.*, *16*(4), 81–86, 1995.

Barabash, S., P. C:son Brandt, O. Norberg, R. Lundin, E. C. Roelof, C. J. Chase, B. H. Mauk, and H. Koskinen, Energetic neutral atom imaging by the Astrid micro satellite, *20, (4/5)*(4/5), 1997.

Barabash, S., O. Norberg, R. Lundin, S. Olsen, K. Lundin, P. C:son Brandt, E. C. Roelof, C. Chase, and B. Mauk, Energetic neutral atom imager on the Swedish micro satellite Astrid, in *Measurement Techniques in Space Plasmas*, edited by R. F. Pfaff et al., no. 103 in AGU Monograph, pp. 257–262, AGU, Washington, DC, 1998.

Barabash, S., M. Holmström, A. Lukyanov, and E. Kallio, Energetic neutral atoms at Mars IV: Imaging of planetary oxygen, *J. Geophys. Res.*, *107*(A10), 1280, doi:10.1029/2001JA000326, 2002.

Bernstein, W., R. L. Wax, N. L. Sanders, and G. T. Inouyé, An energy spectrometer for energetic (1–25 keV) neutral hydrogen atoms, in *Small Rocket Instrumentation Techniques*, North-Holland Publ. Comp., Amsterdam, 1969.

Bertaux, J. L., J. Blamont, M. Marcelin, V. G. Kurt, N. N. Romanova, and A. S. Smirnov, Lyman–alpha observations of Venera-9 and 10 I. The non–thermal hydrogen population in the exosphere of Venus, *Planetary and Space Science*, *26*, 817–831, 1978.

Bertaux, J. L., et al., SWAN: A study of solar wind anisotropies on SOHO with Lyman alpha sky mapping, *Solar Physics*, *162*, 403–439, 1995.

Biernat, H. K., N. V. Erkaev, and C. J. Farrugia, Aspects of MHD flow about Venus, *J. Geophys. Res.*, *104*, 12,617–12,626, 1999.

Biernat, H. K., N. V. Erkaev, and C. J. Farrugia, MHD effects in the Venus magnetosheath, *Adv. Space Res.*, *26*, 1587–1591, 2000.

Brandt, P. C., S. Barabash, E. C. Roelof, and C. J. Chase, ENA imaging at low altitudes from the Swedish microsatellite Astrid: Extraction of the equatorial ion distribution, *J. Geophys. Res.*, *106*(A11), 25,731–25,744, 2001a.

Brandt, P. C., S. Barabash, E. C. Roelof, and C. J. Chase, Energetic neutral atom (ENA) imaging at low altitudes from the Swedish microsatellite Astrid: Observations at low ($\leq$10 keV) energies, *J. Geophys. Res.*, *106*(A11), 24,663–24,674, 2001b.

Brandt, P. C., R. Demajistre, E. C. Roelof, S. Ohtani, D. G. Mitchell, and S. Mende, IMAGE/HENA: Global energetic neutral atom imaging of the plasma sheet and ring current during substorms, *J. Geophys. Res.*, *107*(A12), 1454, 2002a.

Brandt, P. C., S. Ohtani, D. G. Mitchell, M. C. Fok, E. C. Roelof, and R. Demajistre, Global ENA observations of the storm mainphase ring current: Implications for skewed electric fields in the inner magnetosphere, *Geophys. Res. Lett.*, *29*(20), 1954, 2002b.

Brinkfeldt, K., H. Gunell, P. Brandt, et al., First ENA observations at Mars: Solar-wind ENAs on the night side, *Icarus*, submitted, 2005.

Brinton, H. C., H. C. Taylor, Jr., H. B. Niemann, H. G. Mayr, A. F. Nagy, T. E. Cravens, and D. F. Strobel, Venus nighttime hydrogen bulge, *Geophys. Res. Lett.*, *7*, 865–868, 1980.

Brock, A., N. Rodriguez, and R. N. Zare, Characterization of a Hadamard transform time-of-flight mass spectrometer, *Rev. Sci. Instruments*, *71*(3), 1306–1318, 2000.

Burch, J. L. (Ed.), *The IMAGE mission*, Kluwer Academic, reprinted from *Space Sci. Rev.*, vol. 91, Nos. 1-2, 2000.

Burch, J. L., et al., Views of Earth's magnetospere with the IMAGE satellite, *Science*, *291*(5504), 619–624, 2001.

Bush, B. C., and S. Chakrabarti, A radiative transfer model using spherical geometry and partial frequency redistribution, *J. Geophys. Res.*, *100*(A10), 19,627–19,642, 1995.

Collier, M. R., T. E. Moore, M. C. Fok, B. Pilkerton, S. Boardsen, and H. Kahn, Low–energy neutral atom signatures of magnetopause motion in response to southward $b_z$, *J. Geophys. Res.*, *110*, A02,102, doi:10.1029/2004JA010626, 2005.

Collier, M. R., et al., Observations of neutral atoms from the solar wind, *J. Geophys. Res.*, *106*, 24,893–24,906, 2001.

D. E. Anderson, J., and C. W. Hord, Mariner 6 and 7 ultraviolet spectrometer experiment: Analysis of hydrogen Lyman–alpha data, *J. Geophys. Res.*, *76*, 6666–6673, 1971.

Delcourt, D. C., Particle acceleration by inductive electric fields in the inner magnetosphere, *Journal of Atmospheric and Solar–Terrestrial Physics*, *64*, 551–559, 2002.

Demajistre, R., P. C. Brandt, E. C. Roelof, and D. G. Mitchell, Retrieval of global magnetospheric ion distributions from high–energy neutral atom measurements made by the IMAGE/HENA instrument, *J. Geophys. Res.*, *107*(A04214), doi:10.1029/2003JA010322, 2004.

Dessler, A. J., W. B. Hanson, and E. N. Parker, Formation of the geomagnetic storm main-phase ring current, *J. Geophys. Res.*, *66*(11), 3631–3637, 1961.

Edgar, M. L., R. Kessel, J. S. Lapington, and D. M. Walton, Spatial charge cloud distribution of microchannel plates, *Rev. Sci. Instruments*, *60*(12), 3673–3680, 1989.

Escoubet, C. P., C. T. Russell, and R. Schmidt, *The Cluster and Phoenix missions*, Kluwer Academic Publications, Dordrecht, 1997.

Fok, M.-C., T. E. Moore, M. R. Collier, and T. Tanaka, Neutral atom imaging of solar wind interaction with the Earth and Venus, *J. Geophys. Res.*, *109*(A1), A01206, doi:10.1029/2003JA010094, 2004.

Fraser, G. W., The soft X-ray quantum detection efficiency of microchannel plates, *Nuclear Instruments and Methods in Physics Research*, *195*, 523–538, 1982.

Funsten, H. O., D. J. McComas, and M. A. Gruntman, Neutral atom imaging: UV rejection techniques, in *Measurement Techniques in Space Plasmas: Fields*, edited by D. T. Y. R. F. Pfaff, J. E. Borovsky, no. 103 in AGU Monograph, pp. 251–256, AGU, Washington, DC, 1998.

Futaana, Y., A. Grigoriev, S. Barabash, et al., First observation of ENA emissions from Martian upper atmosphere, *Icarus*, submitted, 2005a.

Futaana, Y., A. Grigoriev, S. Barabash, et al., Subsolar ENA jet at Mars, *Icarus*, submitted, 2005b.

Gruntman, M., Energetic neutral atom imaging of space plasmas, *Rev. Sci. Instruments*, *68*(10), 3617–3656, 1997.

Gunell, H., K. Brinkfeldt, M. Holmström, P. Brandt, et al., First ENA observations at Mars: Charge exchange ENAs produced in the magnetosheath, *Icarus*, accepted, 2005a.

Gunell, H., M. Holmström, S. Barabash, E. Kallio, P. Janhunen, A. F. Nagy, and Y. Ma, Planetary ENA imaging: Effects of different interaction models for Mars, *Planetary and Space Science*, in press, 2005b.

Gunell, H., M. Holmström, H. K. Biernat, and N. V. Erkaev, Planetary ena imaging: Venus and a comparison with mars, *Planetary and Space Science*, *53*(4), 433–441, doi: 10.1016/j.pss.2004.07.021, 2005c.

Hartle, R. E., H. G. Mayr, and S. J. Bauer, Global circulation and distribution of hydrogen in the thermosphere of Venus, *Geophys. Res. Lett.*, *5*, 719, 1978.

Hedin, A. E., Extension of the MSIS thermosphere model into the middle and lower atmosphere, *J. Geophys. Res.*, *96*, 1159–1172, 1991.

Holmström, M., S. Barabash, and E. Kallio, Energetic neutral atoms at Mars I: Imaging of solar wind protons, *J. Geophys. Res.*, *107*(A10), 1277, doi:10.1029/2001JA000325, 2002.

Holmström, M., K. Brinkfeldt, S. Barabash, and R. Lundin, Observations in the shadow of Mars by the Neutral Particle Imager, in *Advances in Geosciences*, World Scientific Publication Company, submitted, 2005.

Johansen, G. A., Development and analysis of silicon based detectors for low energy nuclear radiation, Ph.D. thesis, University of Bergen, Bergen, Norway, 1990.

Kallio, E., An empirical model of the solar wind flow around Mars, *J. Geophys. Res.*, *101*, 11,133–11,147, 1996.

Kallio, E., and S. Barabash, On the elastic and inelastic collisions between precipitating energetic hydrogen atoms and Martian atmospheric neutrals, *J. Geophys. Res.*, *105*, 24,973–24,996, 2000.

Kallio, E., and S. Barabash, Atmospheric effects of precipitating energetic hydrogen atoms on the Martian atmosphere, *J. Geophys. Res.*, *106*, 165–177, 2001.

Kallio, E., J. G. Luhmann, and S. Barabash, Charge exchange near Mars: The solar wind absorption and energetic neutral atom production, *J. Geophys. Res.*, *102*, 22,183–22,197, 1997.

Kallio, E., et al., Scattering of ENAs in the martian atmosphere: Implications and ENA sounding, *Icarus*, submitted, 2005.

Keating, G. M., et al., Models of Venus neutral upper atmosphere: structure and composition, *Adv. Space Res.*, *5*(11), 117–171, 1985.

Kivelson, M. G., and C. T. Russell, *Introduction to space physics*, Cambridge University Press, Cambridge, UK, 1995.

Krasnopolsky, V. A., and G. R. Gladstone, Helium on Mars: EUVE and PHOBOS data and implications for Mars' evolution, *J. Geophys. Res.*, *101*(A7), 15,765–15,772, 1996.

Lichtenegger, H., H. Lammer, and W. Stumptner, Energetic neutral atoms at Mars: 3. flux and energy distributions of planetary energetic H atoms, *Geophys. Res. Lett.*, *107*(A10), doi: 10.1029/2001JA000322, 2002.

Mayr, H. G., I. Harris, H. B. Niemann, H. C. Brinton, N. W. Spencer, H. A. Taylor, R. E. Hartle, W. R. Hoegy, and D. M. Hunten, Dynamic properties of the thermosphere inferred from Pioneer Venus mass spectrometer measurements, *J. Geophys. Res.*, *85*, 7841–7847, 1980.

McKenna-Lawlor, S., et al., The energetic NeUtral Atom Detector Unit (NUADU) for China's Double Star mission and its calibration, *Nuclear Instruments and Methods in Physics Research A*, *530*, 311–322, 2004.

McKenna-Lawlor, S., et al., The NUADU experiment on tc–2 and the first energetic neutral atom (ENA) images recorded by this instrument, *Ann. Geophys.*, accepted, 2005.

McPherron, R. L., The role of substorms in the generation of magnetic storms, in *Magnetic Storms*, edited by B. T. Tsurutani, W. D. Gonzalez, Y. Kamide, and J. K. Arballo, no. 98 in AGU Monograph, pp. 131–148, AGU, Washington, DC, 1997.

Mende, S. B., et al., Far ultraviolet imaging from the IMAGE spacecraft. 1. System design, *Space Sci. Rev.*, *91*, 243–270, 2000.

Mengel, J. G., D. R. Stevens-Rayburn, H. G. Mayr, and I. Harris, Non-linear three dimensional spectral model of the Venusian thermosphere with super-rotation–II. temperature composition and winds, *Planetary and Space Science*, *37*, 707–722, 1989.

Mitchell, D. G., P. C. Brandt, E. C. Roelof, D. C. Hamilton, K. C. Retterer, and S. Mende, Global imaging of $O^+$ from IMAGE/HENA, *Space Sci. Rev.*, *109*(1-4), 63–75, 2003.

Mitchell, D. G., P. C. Brandt, E. C. Roelof, J. Dandouras, S. M. Krimigis, and B. H. Mauk, Energetic neutral atom emissions from Titan interaction with Saturn's magnetosphere, *Science*, *308*, 989–992, 2005.

Mitchell, D. G., et al., The imaging neutral camera for the Cassini mission to Saturn and Titan, in *Measurement Techniques in Space Plasmas: Fields*, edited by D. T. Y. R. F. Pfaff, J. E. Borovsky, no. 103 in AGU Monograph, pp. 281–287, AGU, Washington, DC, 1998.

Mitchell, D. G., et al., High energy neutral atom (HENA) imager for the IMAGE mission, *Space Sci. Rev.*, *91*, 67–112, 2000.

Moore, T., et al., The low energy neutral atom imager for IMAGE, *Space Sci. Rev.*, *91*, 155–195, 2000.

Moore, T. E., M. R. Collier, M. C. Fok, S. A. Fuselier, H. Kahn, W. Lennartsson, D. G. Simpson, G. R. Wilson, and M. O. Chandler, Heliosphere–geosphere interactions using low energy neutral atom imaging, *Space Sci. Rev.*, *109*, 351–371, 2003.

Mura, A., A. Milillo, S. Orsini, E. Kallio, and S. Barabash, Energetic neutral atoms at Mars: 2. imaging of the solar wind–phobos interaction, *J. Geophys. Res.*, *107*(A10), 1278, doi: 10.1029/2002JA000328, 2002.

Nagy, A. F., T. E. Cravens, J.-H. Yee, and A. I. F. Stewart, Hot oxygen atoms in the upper atmosphere of Venus, *Geophys. Res. Lett.*, *8*, 629–632, 1981.

Norberg, O., et al., The micro satellite Astrid, in *12th ESA Symposium on Rocket and Balloon Programmes and Related Research*, pp. 273–277, ESA–PAC, Lillehammer, Norway, 1995.

Paresce, F., Quantum efficiency of a channel electron multiplier in the far ultraviolet, *Applied Optics*, *14*(12), 2823–2824, 1975.

Parks, G. K., *Physics of space plasmas*, Addison–Wesley Publishing Company, Redwood City, California, 1991.

Phillips, J. L., and D. J. McComas, The magnetosheath and magnetotail of Venus, *Space Sci. Rev.*, *55*, 1–80, 1991.

Pollock, C. J., et al., Medium energy neutral atom (MENA) imager for the IMAGE mission, *Space Sci. Rev.*, *91*(1), 113–154, 2000.

Pollock, C. J., et al., The role and contributions of energetic neutral atom (ENA) imaging in magnetospheric substorm research, *Space Sci. Rev.*, *109*(1-4), 155–182, 2003.

Rodriguez, J. M., M. J. Prather, and M. B. McElroy, Hydrogen on Venus: exospheric distribution and escape, *Planetary and Space Science*, *32*, 1235–1255, 1984.

Roelof, E. C., Energetic neutral atom image of a storm-time ring current, *Geophys. Res. Lett.*, *14*(6), 652–655, 1987.

Roelof, E. C., Remote sensing of the ring current using energetic neutral atoms, *Adv. Space Res.*, *9*(12), 195–203, 1989.

Roelof, E. C., ENA emission from nearly-mirroring magnetospheric ions interacting with the exosphere, *Adv. Space Res.*, *20*(3), 361–366, 1997.

Roelof, E. C., and A. J. Skinner, Extraction of ion distributions from magnetospheric ENA and EUV images, *Space Sci. Rev.*, *91*, 437–459, 2000.

Roelof, E. C., D. G. Mitchell, and D. J. Williams, Energetic neutral atoms (E$\approx$ 50 keV) from the ring current: IMP 7/8 and ISEE 1, *J. Geophys. Res.*, *90*(A11), 10,991–11,008, 1985.

Sauer, K., K. Dubinin, K. Baumgartel, and A. Bogdanov, Deimos: An obstacle to the solar wind, *Science*, *269*, 1075, 1995.

Sullivan, J. D., Geometrical factor and directional response of single and multi-element particle telescopes, *Nuclear Instruments and Methods*, *95*, 5–11, 1971.

Taguchi, S., M. R. Collier, T. E. Moore, M.-C. Fok, and H. J. Singer, Response of neutral atom emissions in the low-latitude and high-latitude magnetosheath direction to the magnetopause motion under extreme solar wind conditions, *J. Geophys. Res.*, *109*, A04,208, 2004.

Tanaka, T., and K. Murawski, Three–dimensional MHD simulation of the solar wind interaction with the ionosphere of Venus: Results of two–component reacting plasma simulation, *J. Geophys. Res.*, *102*, 19,805–19,821, 1997.

Tobiska, W. K., T. Woods, F. Eparvier, R. Viereck, L. Floyd, D. Bouwer, G. Rottman, and O. R. White, The SOLAR2000 empirical solar irradiance model and forecast tool, *Journal of Atmospheric and Terrestrial Physics*, *62*, 1233–1250, 2000.

Tsurutani, B. T., W. D. Gonzalez, Y. Kamide, and J. K. Arballo, *Magnetic Storms*, no. 98 in AGU Monograph, AGU, Washington, DC, 1997.

Wilken, B., et al., RAPID–the imaging energetic particle spectrometer on Cluster, *Space Sci. Rev.*, *79*(1-2), 399–473, 1997.

Zhang, M. H. G., J. G. Luhmann, S. W. Bougher, and A. F. Nagy, The ancient oxygen exosphere of Mars: Implications for atmosphere evolution charge exchange, *J. Geophys. Res.*, *98*, 10,915–10,923, 1993.

# Acknowledgments

It has been more than four years since I first stepped into the IRF calibration facility. It is hard to believe that four years can go this fast and yet, when measured in experiences gained, seem like decades. During this time I have learned what experimental science really is. Many have helped and contributed to this work over the years in so many different ways. Thank you all! The following people especially deserve my gratitude.

I would like to extend a very special thanks to my supervisor, Stas Barabash for the possibilities and responsibilities that have been offered during these years. Stas has, somehow, always found the time (from where I have no clue, it is one of the great mysteries of the Universe!) to answer questions or discuss problems. He has always listened and taken the opinions and suggestions, how ever silly they may have been, under serious consideration. I have not stopped to be amazed at the ability he has to find solutions and come up with ideas during the discussions. Whenever I came to him with problems or strange looking data, he'd look at it, sit quiet for a short while, then burst out "Aha! But wait! We can do like this..." and a brilliant solution would be presented. Whenever I came to him with an idea, he would again say "Aha! But wait! We can do like this..." and suddenly the idea had evolved into much more. It has been a great inspiration to work under such circumstances Stas!

I am greatly in debt to Herbert Gunell for all his help with this work. The help with everything from proof-reading, providing simulations, finding quotes for the different chapters, to sorting out the data analysis has been much appreciated. One misconception I think I had in the beginning was that I thought most things was already more or less known. Herbert has taught me that the starting point of all good science is to understand that nothing is really certain. Most concepts are only as solid as the model describing them.

Pontus C:son Brandt have also been a great friend and helped with various things during this time, especially for taking care of me at the . If the work gets frustrating, Pontus has a wonderful way of making science interesting and fun again. He is a true master of making sense out of the seemingly impossible using large arrows ("Scientists have a tendency to get confused so always use large arrows in your powerpoints, Klas!") and a natural curiosity that is awfully contagious.

I would also like to thank Kazushi Asamura for a very tough, but interesting start of my PhD studies. Those first two months in the calibration lab I learned two things: How to calibrate space particle instruments and that I would never survive working i Japan.

Special thanks also to the Swedish National Graduate School of Space Technology, which provided financial support for this work.

Many more should be mentioned here. Mats Holmström for help with the NPI data analysis. Torbjörn Lövgren for allowing me to work on the thesis instead of worrying about how to print it. Rick McGregor for proof-reading on very short notice. Jan Balaz and Yoichi Kazama for teaching me the secrets of noise reduction in detector systems. Bill Sandel and Charles Curtis for excellent work with the UV calibrations. Stina Andersson for helping with the formalities of becoming a PhD candidate. Johan Arvelius, Jonas Ekeberg and Andreas Ekenbäck for help with Latex. Grigory Nikulin for IDL tips and tricks and all the rest of the colleagues at the IRF for making my time here very enjoyable! My parents, Gunnel och Bernt, have always supported me in whatever I have done. So also in this. Thank you!

Finally, Märta, I don't know if I could have done this, or anything for that matter, without you.